ministerie van verkeer en waterstaat

koninklijk nederlands meteorologisch instituut

the spreading and mixing of dense gas clouds in still air

A.P. van Ulden

scientific reports WR 87-12

wetenschappelijke rapporten WR 87-12

de bilt, 1987

KNMI

CONTENTS

* Chapter II is based on a previous publication:
Van Ulden, A.P., 1984: A new bulk model for dense gas dispersion: two-dimensional spread in still air. In: Atm. Dispersion of Heavy Gases and Small Particles (G. Ooms and H. Tennekes eds., Springer Verlag) 419-440.

** Chapter III is a synthesis and extension of the following papers:
Van Ulden, A.P., 1987 A: The spreading and mixing of a dense cloud in still air. Proceedings of I.M.A. conference on Stably Stratified Flow and Dense Gas Dispersion, Chester, April, 1986. Oxford University Press, J. Puttock, editor, in press.
Van Ulden, A.P., 1987 B: The heavy gas mixing process in still air at Thorney Island and in the laboratory. J. of Hazardous Materials, Vol. 16, pp 411-426.
Van Ulden, A.P., 1986: The relative importance of turbulence generated by a spreading dense cloud and atmospheric turbulence. Paper presented at the Second Symposium on Heavy Gas Dispersion Trials at Thorney Island, Sheffield, September, 1986.
Van Ulden, A.P., 1987 C: Some aspects of the dispersion of dense puffs. Paper presented at the Third international Symposium on Stratified Flows, Pasadena, February, 1987.

VOORWOORD

In dit proefschrift wordt onderzoek beschreven dat verband houdt met de preventie van rampen door gevaarlijke stoffen. Het onderzoek vindt zijn oorsprong in de interesse van het Directoraat Generaal van de Arbeid voor het zo veilig mogelijk hanteren van gevaarlijke stoffen. In het begin van de jaren zeventig werd onderzoek gestart naar de problematiek van chloor. Chloor is een giftig gas; het werd in de eerste wereldoorlog gebruikt als strijdgas. Het wordt thans in grote hoeveelheden geproduceerd als basisstof voor de chemische procesindustrie. Chloor is veel zwaarder dan lucht. Daarom bestond de vrees, dat bij een ongeval met chloor, dit zware gas als een deken het aardoppervlak zou bedekken en zich weinig met lucht zou mengen. Dit zou aanzienlijke risico's voor de bevolking met zich mee kunnen brengen.

Over deze problematiek werd het KNMI in 1971 benaderd door de Arbeidsinspectie. Als jong onderzoeker werd ik aan dit probleem gezet. Het bleek een bijzonder probleem te zijn, zowel vanwege de grote maatschappelijke relevantie, als vanwege het vrijwel ontbreken van kwantitatieve beschrijvingen in de toenmalige literatuur. In de beginfase van mijn onderzoek heb ik veel steun ontvangen van Ger Abraham (Waterloopkundig Laboratorium), die mij wegwijs heeft gemaakt in de problematiek van dichtheidsstromingen. Ook heb ik enkele verkennende experimenten kunnen doen bij het Waterloopkundig Laboratorium. Op basis van deze experimenten, en op basis van in de literatuur aanwezige informatie over de spreiding van olie op water, heb ik een eenvoudig model ontwikkeld voor de spreiding van een zware gaswolk op een horizontaal oppervlak. Ondermeer met behulp van dit model werden grootschalige experimenten ontworpen en uitgevoerd door een twintigtal bedrijven en overheidsinstellingen in Nederland. Deze experimenten werden uitgevoerd op de Maasvlakte bij Rozenburg in 1973 en 1974 onder de bezielende leiding van de heer E.H. Siccama (Arbeidsinspectie). Ik heb voor het KNMI aan deze experimenten deelgenomen, daarbij voortreffelijk ondersteund door Wim Schipper en door de Instrumentele Afdeling van het KNMI. Voorts leverde de weerkamer in De Bilt speciale weersverwachtingen, die essentieel waren voor het succes en de veiligheid van de experimenten.

De Nederlandse experimenten leverden zowel direct bruikbare informatie op, als ook inspiratie voor verder onderzoek. Eind jaren zeventig kwam dit onderzoek internationaal sterk op gang. Dit leidde tot een aantal nieuwe experimenten in het buitenland en tot een toename van de internationale samenwerking op het gebied van modelontwikkeling. Deze internationale ontwikkelingen

vormen de voedingsbodem voor het recente onderzoek dat beschreven is in dit proefschrift.

Zo'n 15 jaar zijn voorbijgegaan sinds de start van het onderzoek naar de verspreiding van zware gassen. Nú vordert het internationale onderzoek met rasse schreden. Bevredigende en praktisch bruikbare modellen liggen thans in het verschiet. De boodschap is duidelijk: het bereiken van tastbare resultaten met behulp van resultaat gericht onderzoek kan een aanzienlijke tijd vergen. Onderzoeken is vooruitzien.

Ik ben het KNMI erkentelijk, dat het mij de ruimte gaf: 15 jaar geleden voor het opzetten van dit onderzoek en de laatste jaren voor het realiseren van dit werkstuk. Voorts gaat mijn dank uit naar de vele personen in binnen- en buitenland die een rol hebben gespeeld bij het tot stand komen van dit proefschrift. In het bijzonder ben ik dank verschuldigd aan Bronno de Haan, Theo van Stijn en Roland Stull voor het slechten van numeriek-wiskundige barrières en aan Günther Können voor zijn spirituele inbreng. Tenslotte spreek ik mijn waardering uit over de grote inzet van Marleen Kaltofen en van de tekenkamer en drukkerij van het KNMI bij het feitelijk realiseren van dit proefschrift..

SAMENVATTING

In onze industriële samenleving worden vele gassen gebruikt en geproduceerd, die brandbaar, explosief, radioactief of giftig zijn. Dit maakt ongevallen mogelijk waarbij grote hoeveelheden van een gevaarlijk gas in de atmosfeer kunnen vrijkomen. Zulke ongevallen hebben plaats gevonden en zullen met grote waarschijnlijkheid ook in de toekomst plaats vinden. Een speciale klasse van ongevallen is die waarbij in korte tijd een wolk zwaar gas vrijkomt. Zo'n zware gaswolk stroomt uit over het aardoppervlak onder invloed van de zwaartekracht. Dit kan resulteren in hoge gasconcentraties nabij de grond over grote oppervlakken, met alle risico's van dien. In het geval van een zeer grote en dichte gaswolk en lage windsnelheden zal deze uitstroming weinig worden beïnvloed door de atmosferische omstandigheden: de gaswolk bepaalt zijn eigen ontwikkeling en vormt hierbij een zogenaamd quasi-ontkoppeld systeem.

Dit proefschrift is gericht op de beschrijving van quasi-ontkoppelde gaswolken. De opbouw van het proefschrift is als volgt.

In een korte inleiding worden de belangrijkste vormingsmechanismen van zware gaswolken gegeven en het verloop van de verspreiding geschetst. Dit wordt geïllustreerd met een aantal foto's.

Hoofdstuk I beschrijft enkele elementaire modelleringsprincipes. Er wordt een aantal eenvoudige "schalingswetten" afgeleid, die ruwe schattingen mogelijk maken van de afmetingen van en de concentraties in zware gaswolken.

In hoofdstuk II wordt de problematiek van twee-dimensionale dichtheidsstromingen geanalyseerd. Aandacht wordt besteed aan de structuur van de voorste begrenzing van de zware vloeistof (of het zware gas). Zo'n voorste begrenzing wordt gekenmerkt door een abrupte sprong in de dichtheid en wordt veelal front genoemd. Twee-dimensionale fronten zijn goed bestudeerd in het laboratorium. Experimentele informatie uit de literatuur wordt in dit hoofdstuk gebruikt voor het afleiden van schalingswetten voor de frontstructuur. Voorts wordt in dit hoofdstuk een model afgeleid voor de dynamica van de zware vloeistof achter het front. Hierbij wordt gebruik gemaakt van ruimtelijk geïntegreerde bewegingsvergelijkingen. Een dergelijk model wordt dynamisch integraal-model genoemd.

Hoofdstuk III vormt de kern van dit proefschrift. Hier wordt een driedimensionaal dynamisch integraal-model voor een zware gaswolk afgeleid. Het inzakken, uitspreiden en opmengen van de wolk wordt beschreven door ruimtelijk geïntegreerde bewegingsvergelijkingen. Hierbij wordt rekening gehouden met

horizontale en verticale versnellingen in en rond de wolk. Voor de cirkelvormige rand van de wolk wordt de frontstructuur van hoofdstuk II gebruikt. Het opmengen van de wolk wordt beschreven middels een ruimtelijk geïntegreerde vergelijking voor de turbulente energie. Met deze vergelijkingen worden de straal van de wolk en de gasconcentraties berekend als functie van de tijd. Deze worden vergeleken met experimentele gegevens uit de literatuur. Het blijkt dat de straal van de wolk en de concentratieprofielen goed worden beschreven. Tevens blijkt uit de evaluatie van de meetgegevens dat concentraties nabij de grond vele malen hoger zijn dan tot dusverre werd aangenomen (III.5.3).

Het hoofdstuk wordt afgesloten met een uitvoerige evaluatie en gevoeligheidsanalyse van het model en met een beschouwing over de toepasbaarheid van simpele schalingswetten.

Ter afronding van het proefschrift wordt in hoofdstuk IV gesproken over het opzetten van een model, dat naast de quasi-ontkoppelde toestand ook andere fasen in het verspreidingsproces kan beschrijven. In zo'n model begint de wolk in de quasi-ontkoppelde fase, spreidt zich uit en evolueert uiteindelijk naar de zogenaamde passieve eindfase. In het hoofdstuk wordt in het kort beschreven welke stadia de wolk hierbij doorloopt en wat de dominerende processen zijn, welke beschrijvingen hiervoor reeds voorhanden zijn en welke problemen nog moeten worden opgelost. De conclusie is dat het dynamisch integraal-model uit hoofdstuk III een geschikt uitgangspunt is voor het construeren van een dergelijk algemeen model.

SUMMARY

The present work was originally started in the early seventies. In the Netherlands the authorities and companies questioned the safety of production, transport and processing of large quantities of chlorine. Chlorine is a toxic and dense gas. A release of a large amount of chlorine is a considerable hazard to the environment. However, the details of the spreading mechanism of high density gases in the atmosphere were greatly unknown. In 1973 experiments were carried out in the Netherlands to investigate these problems. Pictures, of these experiments, shown in the introductory section of this thesis visualize the spreading of a dense gas cloud. These pictures show that a dense cloud spreads over the ground and takes the form of a large shallow pancake. The dominating mechanism is the action of gravity. Indeed, in the life cycle of a dense cloud there is a period in which gravity-induced spreading and mixing almost fully determines the dispersion of the cloud. So the cloud behaves as if it is uncoupled from the atmospheric flow around it. Therefore we call this phase the quasi-uncoupled phase. This work focusses on the modeling of quasi-uncoupled dense clouds. The modeling is described in three steps, subsequently given in the chapters I, II and III.

In chapter I the basic modeling principles are described and some scaling laws are derived. These allow a simple first-order estimate of the size and mean concentration of the cloud as a function of time.

In chapter II a detour is made to investigate two-dimensional density currents. The frontal structure of the leading edge of such currents has been studied relatively well in the laboratory. Laboratory data are used to derive a parameterisation of this frontal structure. The bulk dynamics of two-dimensional density currents is studied by means of a special integral-form of the momentum equation that includes the effects of entrainment and allows the existence of large density differences between the dense flow and the ambient fluid.

In chapter III a dynamical integral-model for axisymmetric clouds is presented. From the fundamental equations of motions, integral-equations are derived for the spreading, slumping and mixing of the cloud. These equations account for radial and vertical accelerations in and around the cloud and for the effect of large density differences between the cloud and the environment. Turbulent mixing is described with an entrainment equation, which uses the turbulent kinetic energy of the cloud. This turbulent energy is described with

a newly developed time-dependent turbulent-energy equation.

The model is compared with observations on axisymmetric dense clouds taken from the literature. First radial gravity spreading is considered (III.5.2). Here the agreement between model simulations and experimental data is quite satisfactory. The present results on radial spreading are consistent with the results of previous studies. However in this study no ad-hoc fitting of model coefficients was needed to achieve this.

Next experimental concentration data are analysed. The present analysis shows that near-surface concentrations are likely to be much higher than indicated by previous studies of the same experimental data. The reason for this is that usually a Gaussian or uniform profile is assumed for the vertical distribution of area-averaged cloud concentrations. The present analysis shows that such profiles are poor approximations to the observed profiles, especially close to the ground where strong vertical gradients are observed. In this study a new ad-hoc similarity profile is proposed. With this profile our model gives a satisfactory simulation of observed concentrations (III.5.3).

The remainder of chapter III is devoted to a sensitivity analysis and to a description of model characteristics.

In chapter IV we put the present work in a wider context. We give our views on the possibilities to construct a satisfactory comprehensive dense gas model that includes the transport and dispersion by wind and atmospheric turbulence. Our conclusions are that such possibilities exist and that our dynamic model for still air is a good starting point.

INTRODUCTION AND PROBLEM DEFINITION

In modern society many gases are used and produced which are flammable, explosive, radioactive or toxic. Releases of such gases have occurred in the past and are likely to occur in the future. A brief review of recent accidents has been given by Graziani et al. (1987). It appears that accidental releases of hazardous gases are a grave problem. This is especially the case when the release leads to the quasi-instantaneous formation of a large cloud. In a significant fraction of (potential) accidents, such a cloud will have a density that is larger than the atmospheric air density. Such a high density may result from the high molecular weight of the gas that is released, or from the low temperature at which the gas is released. The latter will occur when the gas has a low boiling point and is stored in liquefied form. Three major release mechanisms may result in the quasi-instantaneous formation of a dense cloud.

Type 1

The gas is stored in liquefied form under pressure at ambient temperature. After a failure of the storage tank the pressure drops suddenly and a significant fraction of the liquefied gas evaporates spontaneously. In this case the heat source for the evaporation is the heat stored in the liquefied gas. Spontaneous evaporation leads to a rapidly expanding hemispheric cloud of a dense gas. The rapid expansion causes vigorous initial mixing with the ambient air.

Type 2

The gas is stored in liquefied form in a container that is cooled down to the boiling temperature of the gas at ambient pressure. In this case no heat is available in the liquid for spontaneous evaporation. After the failure of the tank the liquid will spread over the ground or over a water surface. Especially in the latter case the heat transfer from the surface to the liquefied gas will lead to rapid formation of a dense gas cloud.

Type 3

A dense gas is stored in gaseous form and is released as such (without an intermediate boiling process). In the special case in which the gas is stored at ambient pressure, expansion and enhanced mixing will not occur during the release.

These three types of release mechanisms have been simulated in field and laboratory experiments. Examples are:

type 1: Freon experiment at the "Maasvlakte" (Van Ulden, 1974).

type 2: Low wind cases of LNG, LPG experiments at "Maplin Sands" (e.g. Colenbrander and Puttock, 1984).

type 3: Freon experiments at Porton (Picknett, 1981) and "Thorney Island" (e.g. McQuaid, 1984).

Laboratory experiments with Freon (Havens and Spicer, 1984, 1985).

These and other experiments have supported and stimulated significant modelling efforts during the last 15 years.

The modelling of the behaviour of large dense clouds is by no means a simple task. Apart from the usual problems which arise, when one wants to model the dispersion of passive trace contaminants, dense clouds create a few problems of their own. The main reason for this is that the force of gravity works on dense clouds. This leads to gravity-driven flow phenomena with their own specific characteristics. For a review of this subject we refer to Simpson (1982).

A suitable introduction to the problems related to dense cloud modelling is a time series of pictures of a dense cloud during and after its release. For this purpose we have selected a number of pictures taken during the first large scale field experiments on dense cloud dispersion, that have been carried out in the Netherlands in 1973. A brief survey of these experiments is given in the report "Experiments with Chlorine" (Directorate-General of Labour, 1975). The dense gas problems are discussed in Van Ulden (1974). The aim of these experiments was to acquire a better insight into the behaviour and control of large accidental chlorine spills. To avoid the hazards of a large chlorine release, a potential accident was simulated using freon-12 (CCl_2F_2). This is an invisible, non-toxic and rather inert gas, with a molecular weight of 121 and a boiling point of 243 K.

A quasi-instantaneous source was obtained as follows. A vessel with 1000 kg of liquid freon at ambient temperature was placed over an open tank filled with hot water. At the bottom of the vessel was an outlet which was closed by a rupture disc. The disc was forced to break by an increase of the pressure on the vessel to about 7 bar. This led to a rapid downward outflow of

the liquid freon into the hot water. The water provided sufficient heat for a complete evaporation of the freon in about 5 seconds. Moreover it supplied the cloud with water vapour, the condensation of which made the cloud visible. After its expansion the cloud had a temperature nearly equal to the air temperature. Its density was about 20% higher than that of air.

The formation of the cloud and its subsequent behaviour is illustrated with 6 characteristic pictures on the next pages. The first picture gives the cloud after 1 s, the second picture after 5 s when the cloud formation is completed. We see that the expansion is more or less hemispheric. The cloud edge is very diffuse. This is due to the vigorous turbulent mixing owing to the rapid expansion. After its formation the cloud starts to slump. The pictures 3-5 show the cloud after 8 s, 15 s and 35 s respectively. We see that the cloud acquires a very shallow and wide form. In other pictures, not shown here, it is observed that this form is more or less cylindrical. After 35 s the diameter of this cylinder is about 100 m. Its depth is then about 0.5 m. It is clear that a dense cloud behaves differently from a puff of passive contaminant. In passive puff dispersion the vertical and horizontal scales are of the same order.

The very pronounced slumping, which is observed for a dense cloud, is caused by the combination of the high cloud density and gravity. This makes the cloud negatively buoyant. Therefore dense gases are often called heavy gases. The negative buoyancy results in an increased static pressure in the cloud, which leads to a radially outward pressure force. This causes the outward slumping motion. The process resembles the spreading of a liquid over a solid surface.

The slumping process does not continue indefinitely. In the absence of wind and atmospheric turbulence, the slumping will stop when the cloud height reduces to the hieght of the roughness elements and irregularities of the surface. When there is wind, and turbulence, sooner or later atmospheric transport and diffusion will carry the cloud away and dilute it to smaller and smaller concentrations until it behaves as a passive contaminant. The start of the latter processes is shown in picture 6, which was taken after 70 s. Here we see that only remnants of the visible cloud still linger at the surface. The bulk of the cloud has become invisible due to mixing with dry air and evaporation of the liquid water.

Picture 1

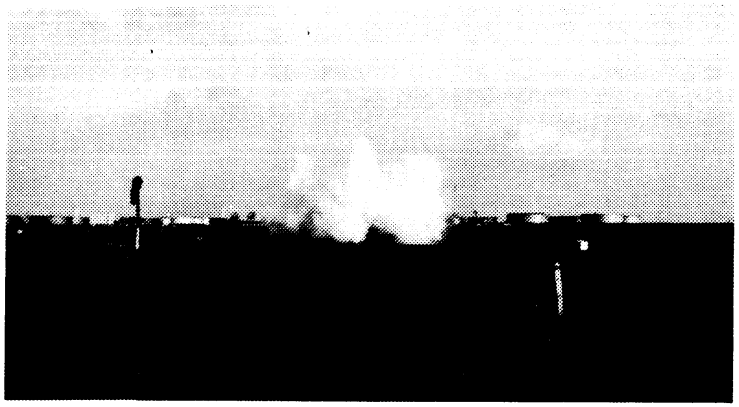

t=1S

Picture 2

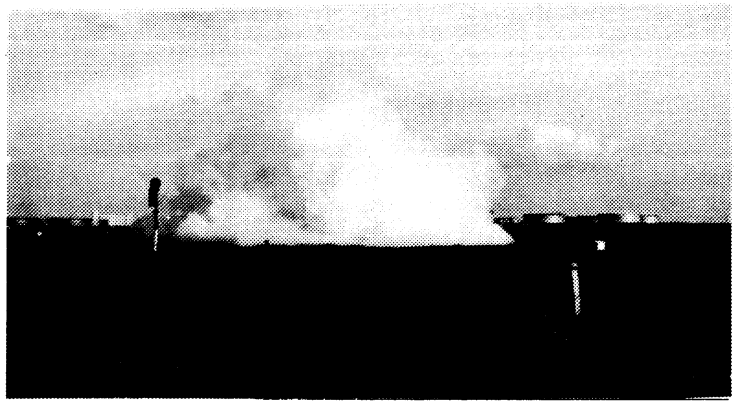

t=5S

◀Cloud diameter 25m▶

Picture 3

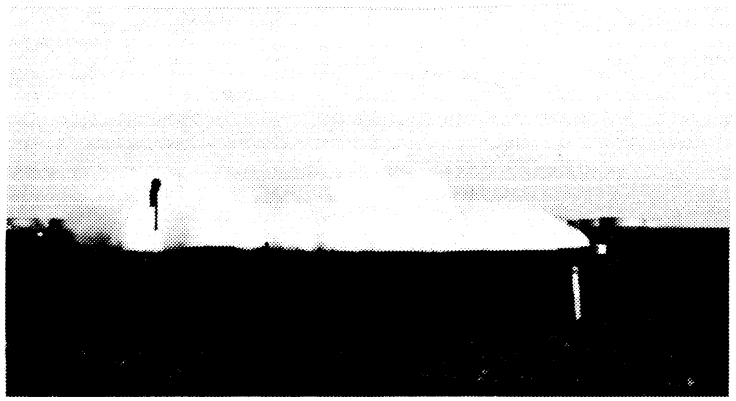

t=8S

Picture 4

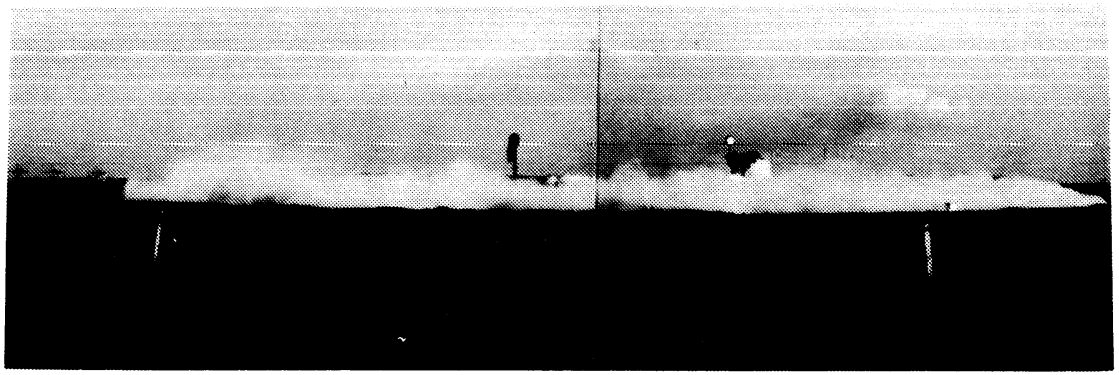

t=15 S

Picture 5

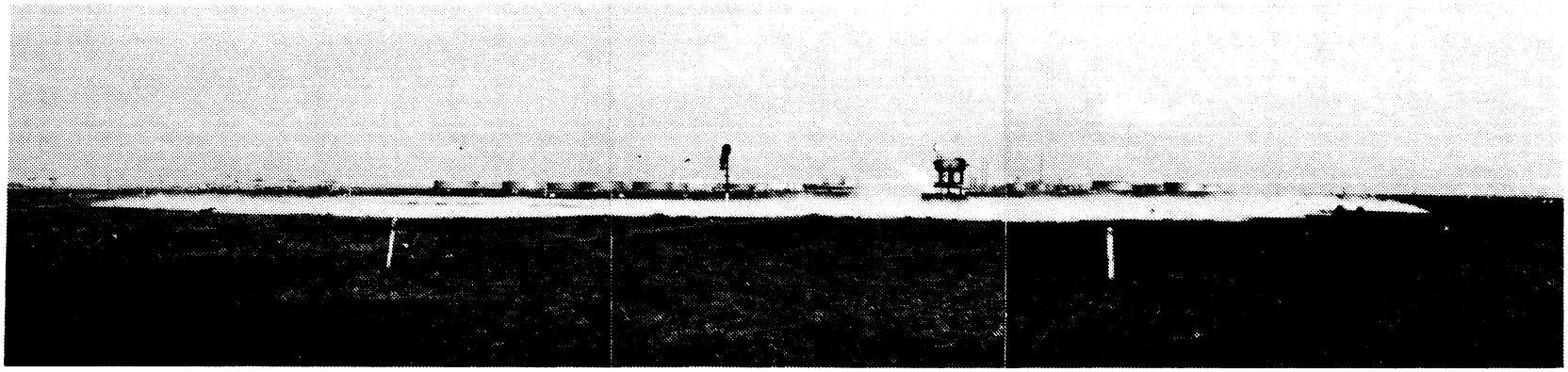

t=35 S

Cloud diameter ca 100 m

Picture 6

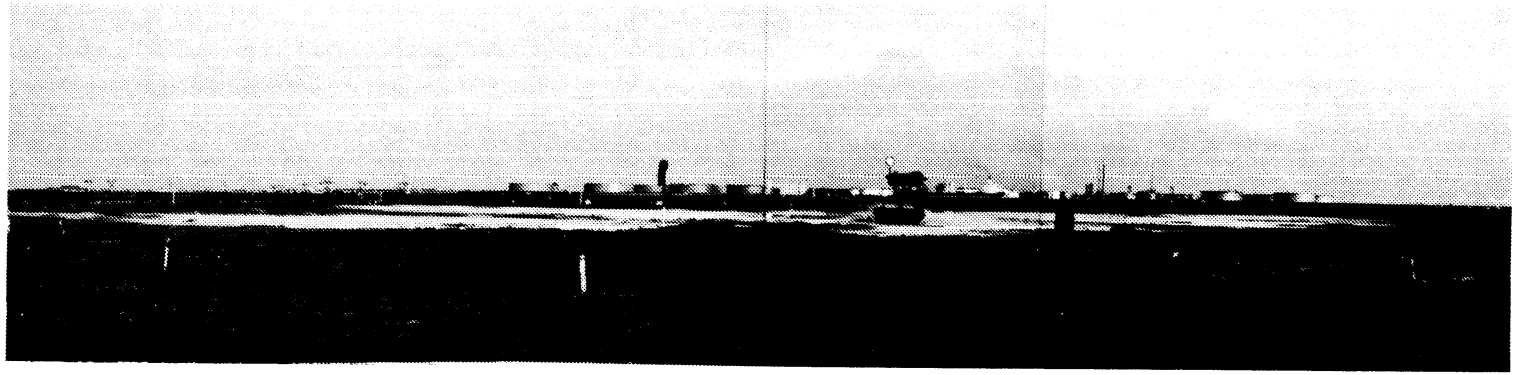

t=70 S

These and other observations suggest that the life cycle of the spreading and mixing of a dense cloud can be split up in five phases.

I The formation phase

This phase comprises the release of the (liquefied) gas and, if appropriate, its following evaporation and expansion. The three major types of formation mechanisms have been given above (picture 1).

II The quasi-uncoupled slumping phase

This phase occurs when the effects of turbulence and momentum of the ambient flow can be neglected, as well as the influence of surface friction. In this phase the dynamics and mixing of the cloud are exclusively driven by the negative buoyancy of the cloud. A slumping and radially spreading cloud is observed with a more or less pronounced raised edge, sharp radial boundaries and a diffuse top. Significant mixing occurs, resulting from the turbulence which is generated by gravity spreading (pictures 2-5).

III The coupled spreading phase

In this phase gravity spreading still dominates over horizontal atmospheric diffusion. However, the cloud no longer slumps because atmospheric turbulence leads to vertical mixing at a similar or greater rate than the gravity induced slumping motion. In addition, advection by the mean wind occurs and surface friction may affect the gravity spreading (picture 6).

IV The mixed phase

In this phase gravity spreading and horizontal diffusion are of comparable importance. The sharp-edged cloud transforms into a diffuse cloud. Vertical diffusion is still reduced by cloud density.

V The passive phase

In this phase cloud density effects can be neglected. Dispersion by atmospheric turbulence and advection by the mean wind are similar to those for a passive puff.

The present work focusses on the second (quasi-uncoupled) phase and in particular with the special case of an isothermal dense cloud, i.e. a cloud with a uniform temperature equal to the air temperature.

Chapter I
INTRODUCTION TO THE MODELLING OF QUASI-UNCOUPLED DENSE CLOUDS

I.1 Basic principles

It appears from observations that a dense cloud in the quasi-uncoupled phase has a cylindrical shape. The radial cloud edge is quite distinct (figure I.1). This calls for a description of the cloud area involving the distance R of the radial cloud edge from the cloud center. The cloud area is given by

$$A = \pi R^2 \ . \tag{I.1}$$

On the other hand the cloud top is quite diffuse and irregular (figure I.1). Clearly the vertical distribution of dense material in the cylindrical cloud is non-uniform. This calls for an integral definition of cloud height. The mean height $\langle z \rangle$ of dense material in the cloud is by definition

$$\langle z \rangle \equiv {}_0\int^R {}_0\int^\infty z\, \Delta\rho(r,z)\, 2\pi r\, dr\, dz \ / \ {}_0\int^R {}_0\int^\infty \Delta\rho(r,z)\, 2\pi r\, dr\, dz \tag{I.2}$$

Here z is the height above the ground, r the radial distance from the cloud center and $\Delta\rho(z,r)$ the difference between the local cloud density $\rho(z,r)$ and the ambient air density ρ_a. The mean height $\langle z \rangle$ can be used to define a mean cloud depth H. Let us consider the special case in which initially the cloud is a cylinder with radius R_o, height H_o and a uniform density difference $\Delta\rho_o$. For this special case it can be simply shown that the relation between the cloud top H_o and the mean height $\langle z \rangle_o$ is

$$H_o = 2\langle z \rangle_o \ . \tag{I.3}$$

This suggests that a suitable general definition for the cloud depth is

$$H \equiv 2\langle z \rangle \ . \tag{I.4}$$

Adopting this definition we may also define a cloud volume by

$$V \equiv \pi R^2 H \ , \tag{I.5}$$

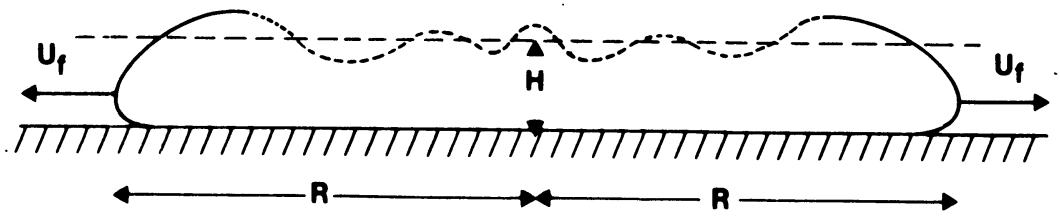

figure I.1: Vertical Cross-section through the cloud center showing the sharp cloud edge and the diffuse cloud top.

a mean cloud density difference by

$$\overline{\Delta\rho} \equiv \int_0^R \int_0^\infty \Delta\rho(r,z)\, 2\pi r\, dr\, dz \;/\; V \qquad (I.6)$$

and a mean cloud density by

$$\bar{\rho} \equiv \rho_a + \overline{\Delta\rho} \; . \qquad (I.7)$$

These definitions have the important and convenient property that they allow a simple and exact representation of the potential energy of the cloud. This potential energy P_E equals

$$P_E = \int_0^R \int_0^\infty g\, \Delta\rho(r,z)\, z\, 2\pi r\, dr\, dz \; , \qquad (I.8)$$

where g is the acceleration by gravity. The integral in (I.8) can be simply evaluated by using (I.2), (I.4), (I.5) and (I.6). The result is

$$P_E = \tfrac{1}{2}\, g\, \overline{\Delta\rho}\, V\, H \; . \qquad (I.9)$$

In this equation $g\, \overline{\Delta\rho}\, V$ is the total negative buoyancy of the cloud. Thus the potential energy equals the negative buoyancy multiplied by the height $\frac{1}{2}H$ of the center of mass of the cloud. This result can be simplified further for the special case of an isothermal cloud. We use the fact that the total mass of material should be conserved. This mass equals $\overline{\rho_o}\, V_o$. Moreover the total mass of the cloud increases due to turbulent entrainment of air. For an isothermal cloud the mass increase at a given instant equals $\rho_a\, (V-V_o)$. Thus the total cloud mass at a given instant equals

$$\bar{\rho}\, V = \overline{\rho_o}\, V_o + \rho_a\, (V-V_o) \; . \qquad (I.10)$$

From this equation it follows directly that

$$\overline{\Delta\rho}\ V = \overline{\Delta\rho_o}\ V_o \ . \qquad \text{(I.11)}$$

Thus for an isothermal cloud the difference between the cloud mass and the mass of an amount of air with the same volume is a conserved quantity. Therefore the negative buoyancy $g\ \overline{\Delta\rho}\ V$ is also a conserved property for an isothermal dense cloud. Using this we may write for the potential energy

$$P_E = \tfrac{1}{2}\, g\ \overline{\Delta\rho_o}\ V_o\ H \ . \qquad \text{(I.12)}$$

So isothermal clouds have the convenient property that their potential energy is fully specified by the initial conditions and by the actual cloud height H.

We will use this property now to illustrate the cloud dynamics in terms of its energy budget. This may help to understand the basic principles of the spreading and mixing processes.

As initial condition we take a still cloud with a potential energy

$$P_{Eo} = \tfrac{1}{2}\, g\ \overline{\Delta\rho_o}\ V_o\ H_o . \qquad \text{(I.13)}$$

The negative buoyancy, which is the basis of this potential energy, also creates an increased static pressure in the cloud. This increased static pressure pushes the cloud radially outward: it starts a radial acceleration, that is accompanied by a downward acceleration for continuity reasons. In terms of energy this corresponds with a transformation of potential energy into kinetic energy (K_E). Indeed slumping implies a loss of height and a loss of potential energy.

In the slumping process the outward moving cloud edge feels the resistance of the ambient air. Continually, new air is accelerated by the cloud edge. Here strong shears in the flow are present that lead to the production of turbulent energy (T_E) at the cost of kinetic energy.

The turbulence thus created leads to two new processes. The first process is turbulent mixing at the top of the cloud. Ambient air is entrained into the cloud volume, which corresponds with a relative thickening of the cloud. This is equivalent with a transformation of turbulent energy back into potential energy. This process we call buoyant destruction. The second process is viscous dissipation. In a turbulent energy cascade energy is transferred to smaller and smaller scales. At the smallest scale viscous friction destroys turbulent energy, while internal heat (I_E) is produced. The flows of energy are summarized in the following diagram:

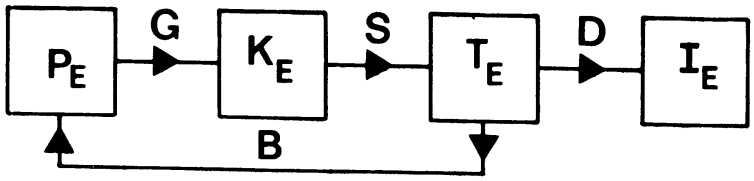

G production of K_E B buoyant destruction of T_E
S production of T_E D viscous dissipation of T_E

In the life cycle of the quasi-uncoupled phase the potential energy decreases monotonously, while the internal heat increases. The kinetic energy starts at a zero value, increases when the cloud accelerates from rest, and decreases later on. The turbulent energy lags behind the kinetic energy, but similarly goes through a maximum during the quasi-uncoupled phase.

It will be clear that the gravity spreading of a dense cloud is a very unsteady process. A proper description of this process requires the solution of time-dependent equations for momentum and energy. This is done in chapter II for 2-dimensional gravity currents and in chapter III for axisymmetric clouds. Before we start with the detailed modeling problems, we first give a description of some simple scaling "laws". This may help the reader to develop some quantitative understanding of the spreading and mixing of dense clouds.

I.2 Simple scaling "laws"

The source for all dense gas motions is the static pressure surplus in the cloud due to its negative buoyancy. Thus we start our scaling analysis with an evaluation of this pressure surplus. Inside the cloud the static pressure P_c varies with height as

$$\partial P_c/\partial z' = -g\rho \ , \qquad (I.14)$$

where z' is the local height and ρ is the local cloud density. To find P_c at a given position (r,z), we integrate (I.14) with respect to z' from z to infinity

$$P_c(r,\infty) - P_c(r,z) = -\int_z^\infty g\rho(r,z')dz' \ . \qquad (I.15)$$

Outside the cloud the static pressure P_a at the height z is given by

$$P_a(\infty) - P_a(z) = -\int_z^\infty g\rho_a \, dz' \ . \qquad (I.16)$$

At an infinite height the pressure is no longer affected by the presence of the cloud, thus

$$P_c(r,\infty) = P_a(\infty) \ . \tag{I.17}$$

The static pressure surplus at a given position in the cloud is then given by

$$\Pi_s(r,z) \equiv P_c(r,z) - P_a(z) = \int_z^\infty g\ \Delta\rho\ (r,z')\ dz' \ . \tag{I.18}$$

A mean value $\overline{\Pi}_S$ of the static pressure surplus may be defined in the same manner as we have defined $\overline{\Delta\rho}$ in (I.6). It reads:

$$\overline{\Pi}_s \equiv \int_0^R \int_0^\infty \Pi_S(r,z)\ 2\pi r\ dr\ dz\ /\ V \ . \tag{I.19}$$

Substituting (I.18) for Π_S we obtain:

$$\overline{\Pi}_s \equiv \int_0^\infty \int_z^\infty g\ \Delta\rho(r,z')\ 2\pi r\ dr\ dz\ dz\ /\ V \ . \tag{I.20}$$

Using (I.2)-(I.6) it can be shown that (I.20) is identical to

$$\overline{\Pi}_s = \tfrac{1}{2}\ g\ \overline{\Delta\rho}\ H \ . \tag{I.21}$$

This result is quite general in the sense that no assumptions have been made regarding the density distribution in the cloud. However, when we want to arrive at simple scaling laws, we have to make such assumptions.

A scaling law for radial gravity spreading can be derived as follows. The radial edge of the cloud has the appearance of a sharp front (see figure I.1). At this front there is a jump in the static pressure. We approximate this pressure jump by its mean cloud value (I.21).
The front moves outward with a velocity

$$U_f \equiv dR/dt \ . \tag{I.22}$$

The moving front meets continually undisturbed ambient air which is accelerated outward and upward. This creates a dynamic pressure Π_a outside the cloud, which scales as

$$\Pi_a = \tfrac{1}{2}\ c\ \rho_a\ U_f^2 \tag{I.23}$$

where c is an empirical drag coefficient. Assuming a balance between the mean static pressure inside the cloud and the dynamic pressure outside the cloud (i.e. $\overline{\Pi}_s = \Pi_a$) we simply find from (I.21) and (I.23) that

$$U_f = k \, (g \, \overline{\Delta\rho} \, H \, / \, \rho_a)^{\frac{1}{2}} \tag{I.24}$$

where

$$k \equiv 1 \, / \, \sqrt{c} \tag{I.25}$$

is a densimetric Froude number. We assume that cloud shape and flow configuration only depend on H, R and U_f. Then k is a constant. Experimental data show that the simple scaling law (I.24) gives a fair description of the radial spreading of a dense cloud and that k is close to unity, except initially when the cloud is still accelerating from rest (see chapters II and III). From this result we may draw a first and quite important conclusion, that is that the radial spreading velocity does not depend on the density surplus $\overline{\Delta\rho}$ alone, but on the product of $\overline{\Delta\rho}$ and H! Thus significant gravity spreading may occur for small values of $\overline{\Delta\rho}$ provided the cloud depth is great enough. Another point, to be noted is, that it is the ratio $\overline{\Delta\rho}/\rho_a$ that matters and not $\overline{\Delta\rho}/\overline{\rho}$. The latter ratio has been used by several authors (e.g. Van Ulden, 1974). A numerical example illustrates the kind of spreading velocities which we may expect. Taking $\overline{\Delta\rho}/\rho_a = 0.1$ and H = 10 m we find that $U_f \approx 3$ m s^{-1}. For the same cloud depth and $\overline{\Delta\rho}/\rho_a = 1$ we find $U_f \approx 10$ m s^{-1}.

From (I.24) we may derive an expression for the cloud radius as a function of time. Using (I.5), (I.11) and (I.22), we may rewrite (I.24) as

$$dR^2/dt = 2k \, (g \, \Delta\rho_o \, V_o \, / \, \rho_a \, \pi)^{\frac{1}{2}} \, . \tag{I.26}$$

Integration of this expression with respect to time yields

$$R^2 - R_o^2 = 2k \, (g \, \Delta\rho_o \, V_o \, / \, \rho_a \, \pi)^{\frac{1}{2}} \, t \, . \tag{I.27}$$

Thus the cloud area is a linear function of time. (I.27) can be written in dimensionless form as follows

$$(R/R_o)^2 = 2k \, (t/t_o) + 1 \tag{I.28}$$

where

$$t_o \equiv R_o/U_o \tag{I.29}$$

is a time scale and

$$U_o = (g\ \Delta\rho_o\ H_o\ /\ \rho_a)^{1/2} \tag{I.30}$$

a velocity scale.

Thus R_o and U_o are "natural" scaling parameters for radial gravity spreading. These scaling parameters can also be used to write the equation (I.24) for the front velocity in dimensionless form. The result for large times ($t/t_o >> 1$) is:

$$U_f/U_o = (kt_o/2t)^{1/2} . \tag{I.31}$$

We see that the front velocity decreases inversely proportional to the square-root of time, which means that the cloud is decelerating.

The spreading "law" (I.31) cannot be valid for early times. Initially the cloud is at rest, so there must be a period in which the cloud accelerates. We will not deal with this acceleration phase in detail. It is useful however to give an estimate for its duration. This estimate is obtained as follows. Initially the static pressure force is used to accelerate both the cloud mass itself and an amount of "added air mass". We approximate the static pressure force which acts on the cloud edge by:

$$F_S \simeq 2\pi R\ H\ \bar{P}_S \tag{I.32}$$

and the inertial force by

$$F_i \simeq \bar{\rho}\ V\ \frac{dU_f}{dt} . \tag{I.33}$$

Assuming a balance between these two forces and using (I.21), we find that for time t=0

$$\left[\frac{dU_f}{dt}\right]_{t=0} \simeq \frac{2g\ \Delta\rho_o\ H_o}{\rho_o\ R_o} \simeq \frac{2\rho_a}{\rho_o}\ \frac{U_o}{t_o} . \tag{I.34}$$

This suggests that an appropriate time scale t_a for the initial acceleration phase is

$$t_a \simeq \frac{\rho_o}{2\rho_a}\ t_o . \tag{I.35}$$

Since normally $\rho_o/2\rho_a$ is of O(1), t_a/t_o is of O(1). A numerical example illustrates the kind of time scales we may expect for the inital acceleration. Let us take a cloud with initially $\Delta\rho_o/\rho_a = 1$, $H_o = 10$ m, $R_o = 10$ m, then we find $U_o = 10$ m s^{-1}, $t_o = 1$ s and $t_a = 1$ s. Thus the initial acceleration phase is very short in this example. A more detailed discussion on this subject is given in chapter III, section 6.3.

Next we proceed with the scaling of the mixing process. We have seen before that observations show that the cloud edges are very distinct. This indicates that little mixing occurs <u>through</u> the cloud edge. On the other hand the cloud top is quite diffuse, which indicates that significant mixing may occur there. Thus as a first appriximation we describe the mixing process by

$$dV/dt = \pi R^2 W_e \ , \tag{I.36}$$

where W_e is an area-averaged top entrainment velocity to be estimated later. Because $V = \pi R^2 H$ and $dR/dt = U_f$ we may write (I.36) as

$$dH/dt = - 2(H/R) U_f + W_e \ . \tag{I.37}$$

This shows that the cloud height changes by two processes. The first term at the right hand side gives the mean downward fluid motion caused by the spreading and slumping process. The last term shows that the entrainment velocity is equivalent to a mean upward motion of the cloud top relative to the fluid motion. In section 1.1 we have seen that the potential energy of the cloud is proportional to the cloud height (I.12). Thus the entrainment relation (I.37) is directly linked with the energy budget of the cloud. To be more precise, the energy budget of the cloud imposes certain restrictions on the scaling laws of W_e. W_e should not be modeled in such a way that the potential energy increases above its initial value. On the contrary, we expect that the potential energy and the cloud height decrease with time because of continuous dissipation of energy into heat. Thus we expect that

$$W_e < 2(H/R) U_f \ . \tag{I.38}$$

Let us now look at the entrainment process itself. Entrainment occurs because turbulence is produced by the shear that is related to the radial gravity spreading. The strongest shears are present near the advancing leading edge.

Here turbulent eddies are created with an energy density of order $\frac{1}{2} \rho_a U_f^2$. This occurs at a volume rate of order $2\pi R\ H\ U_f$. thus the eddy-production rate should scale as $\pi \rho_a\ R\ H\ U_f^3$. This production rate is used partly for the viscous dissipation of turbulent energy, partly for increasing the potential energy. From (I.12) and (I.37) it follows that the latter energy transformation occurs at a rate $\frac{1}{2} g\ \Delta\rho_o\ V_o\ W_e$. We now assume similarity in the sense that a fixed fraction ε of the turbulent energy production is used for increasing the potential energy. This leads to

$$\tfrac{1}{2} g\ \overline{\Delta\rho_o}\ V_o\ W_e \simeq \varepsilon\ \pi\ \rho_a\ R\ H\ U_f^3 \ . \tag{I.39}$$

Using (I.11), (I.22) and (I.24) we easily obtain that

$$W_e \simeq 2\ \alpha_e \frac{H}{R} \frac{dR}{dt} \ , \tag{I.40}$$

where

$$\alpha_e \equiv \varepsilon\ k^2 \tag{I.41}$$

is an entrainment coefficient. Comparing (I.40) and (I.37) we see that the energy constraint is met for $\alpha_e < 1$. Further it is interesting to see that in a mathematical sense the scaling law (I.40) for top entrainment is identical to the edge entrainment proposed e.g. by Van Ulden (1974). A major problem with (I.40) is that the value of α_e is not well established. Values for α_e ranging from 0.4 to 1.0 have been given in the literature. Minor variations in α_e have a significant effect on cloud concentrations for large times. This can be seen, when we substitute (I.40) for W_e in (I.36) and solve for V by using (I.24). The result is

$$V/V_o = [2k(t/t_o) + 1]^{\alpha_e} \ . \tag{I.42}$$

From this result we see that for great times V/V_o becomes very sensitive for the value of α_e. Thus a significant amount of uncertainty exists here. More discussion on this subject is given in chapter III. Despite the uncertainties in the scaling "laws" (I.28) and (I.42), these laws are useful for providing a first educated guess for the spreading and mixing of an isothermal dense cloud. We will illustrate this with an example.

Let us take instantaneous release of a cylindrical cloud with $R_o = 10$ m, $H_o = 10$ m and $\Delta\rho_o/\rho_a = 1$. Then $U_o \simeq 10\ m\ s^{-1}$ and $t_o \simeq 1$ s. Let us assume that

$k = 1$ and $\alpha_e = 0.5$. With these values we find from (I.28) that after 50 s the cloud area has been increased by a factor 100, i.e. R is about 100 m. From (I.42) we see that the cloud volume has been increased by a factor 10. Thus average cloud concentration $\bar{c}$ and its relative density difference with air $\overline{\Delta\rho}/\rho_a$ are decreased to about 10% of their initial values. The cloud height is also decreased to about 10% of its initial value, i.e. to H = 1 m. By then, according to (I.24), the spreading velocity $U_f \simeq 1$ m s^{-1}. In atmospheric flow conditions with low windspeeds this is a very significant velocity.

The evaluation after 20 minutes gives R = 500 m, H = 0.2 m, $\overline{\Delta\rho}/\rho_a = 0.02$ and $\bar{c} \simeq 0.02$. Then the spreading velocity has decreased to $U_f \simeq 0.2$ m s^{-1}, which still is a significant spreading velocity.

From this numerical example we learn that a large dense cloud may spread over a very large area and becomes very shallow. At the same time significant self-mixing occurs. Also we see that the time scale of all this is quite small. From this it is apparent that gravity spreading and self-induced mixing are features that should be included in models for the dispersion of large dense clouds.

Chapter II
A DYNAMICAL INTEGRAL MODEL FOR TWO-DIMENSIONAL GRAVITY CURRENTS

II.1 Introduction

The gravity spreading phenomena due to negative buoyancy of dense clouds are not unique. Similar phenomena have been observed in other "man-made" flows and in a number of geophysical flows. Examples are:

- exchange flows in locks, which separate salt water and fresh water (e.g. Barr, 1967; Simpson and Britter, 1979);
- the spreading of oil on water (e.g. Abbott, 1961; Fay, 1969; Fanneløp and Waldman, 1972);
- atmospheric cold fronts (e.g. Schmidt, 1911).

For a recent review on gravity currents we refer to Simpson (1982).

Since gravity currents and especially two-dimensional gravity currents have been studied widely, it is useful to study the 2-D problem first before we enter into the details of the axisymmetric spreading problem. In this chapter we focus on horizontal bottom currents, which result from an instantaneous release of dense fluid. For reasons of simplicity we focus on shallow currents in which vertical accelerations can be neglected. We further assume that the ambient fluid is at rest and infinitely deep. Viscous forces are neglected.

The structure of this chapter is as follows. We start in section 2 with a review of studies made on "inertia-buoyancy currents" and discuss some general features of these currents. In section 3 we describe a new bulk model. This models consists of bulk equations for matter and momentum, which are derived from the basic equations of motion. In the sections 4 and 5 we present model results and an evaluation of these. In section 6 we give our conclusions.

II.2 History and problem definition

II.2.1 The leading edge of gravity currents

Major information on the conditions of the leading edge can be found in Schmidt (1911), Benjamin (1968), Simpson (1972) and Simpson and Britter (1979). In figure II.1 an arrested leading edge is shown.

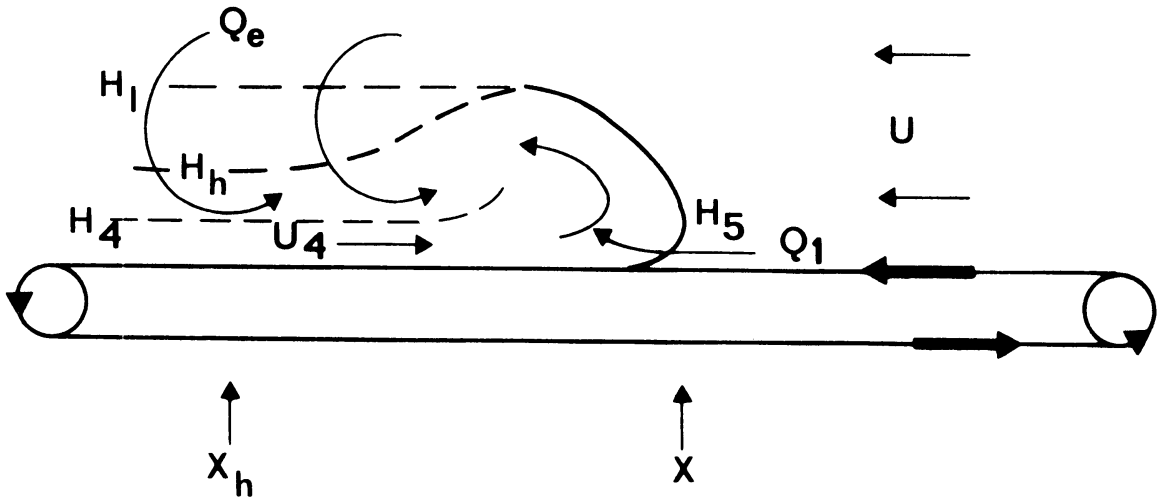

figure II.1: The head of a steady gravity current (after Simpson and Britter, 1979).

Some characteristic features are:

1. At the leading edge a head is present with a depth H_1 which is about twice the depth H_h of the current behind the head.
2. An elevated forward stagnation point is present. Below this point an insignificant flux Q_1 of ambient fluid is entrained.
3. Behind the head a wake region is present in which significant mixing occurs.
4. In the head a significant internal flow is present. Near the surface denser fluid moves towards the head with a velocity U_4. In the wake region a mixing layer moves away from the head.
   S & B found that

$$U_4 \approx 0.2\ U, \qquad \text{(II.2.1)}$$

   where U is the velocity of the current relative to the ambient fluid.
5. The dimensionless velocity C_h of the leading edge can be written as

$$C_h = U / \sqrt{g\Delta\rho_h H_h/\rho_a}\ , \qquad \text{(II.2.2)}$$

   where $\Delta\rho_h$ is the mean density difference behind the head, ρ_a the density of the ambient fluid and H_h the densimetric mean depth behind the head. A formal definition of the product of $\Delta\rho_h$ and H_h is (Fay, 1980):

$$\Delta\rho_h H_h = \int_0^{H_1} \Delta\rho(z)\, dz\ . \qquad \text{(II.2.3)}$$

With this definition the value of C_h may be computed from experimental data. From Schmidt (1911), Benjamin's (1968) review, S & B (1979), Fanneløp et al. (1980), Huppert and Simpson (1981) it follows that

$$C_h = 1.15 \pm 0.05, \qquad \text{(II.2.4)}$$

both for steady and unsteady gravity currents, provided the Reynolds number $UH_h/\nu > O(10^3)$ and provided the current is deeply submerged.

II.2.2 Bulk properties of fixed volume releases

A major contribution to the understanding of the bulk properties of fixed volume releases has been given by Fanneløp and Waldman (1971, 1972) and later by Hoult (1972). Their aim was to describe the spreading of oil on water. They assumed (II.2.2) as a leading edge boundary condition and used the shallow-water equations to describe the interior of the current. They showed that similarity solutions to this set of equations exist for the layer averaged velocity $\bar{u}$, for the local depth h and for the dimensionless velocity

$$C_H \equiv U_f/\sqrt{g\overline{\Delta\rho}H/\rho_a}\ , \qquad \text{(II.2.5)}$$

where U_f is the front velocity, $\overline{\Delta\rho}$ the mean density difference and $H = V/X$ the mean depth of the current. (V is the volume per unit width of current and X the length of the current.) Their results cannot be applied as such to the present problem, because entrainment and the internal flow were not included in their description. Also their solutions are only valid for large times, when the current has passed through its initial acceleration phase into the final deceleration phase. The problems of entrainment and initial acceleration have been dealt with - be it in a crude manner - by Van Ulden (1979). Van Ulden assumed a rectangular shape with a linear velocity distribution and derived a bulk equation for dU_f/dt. He included a static pressure force, a drag force and an effective stress due to entrainment in this equation. However, objections may be raised against the way in which this equation was derived.

It is the purpose of this paper to improve on this. We will derive bulk continuity and momentum equations starting from the basic equations of motion. The now existing better understanding of the leading edge conditions will be employed in the model. Also some features of the approach by Fanneløp and

Waldman (1971, 1972) will be included in the model. Furthermore a parameterization for top entrainment will be presented.

II.3 A new bulk model for fixed volume releases

II.3.1 Introduction

In the remainder of this paper we deal with gravity currents which result from an instantaneous release of a volume V_o (per unit width) of a fluid with density ρ_o that is greater than the density ρ_a of the ambient fluid by an amount $\Delta\rho_o$. The two fluids are assumed incompressible and of equal temperature. The release is at the horizontal bottom at the beginning of an infinitely deep channel in which the ambient fluid is at rest. The initial volume has a length X_o and a mean depth $H_o \equiv V_o/X_o$. After the release a gravity current develops of the type that is shown in figure 2. Such currents develop when surface friction and side wall effects are negligible and the current is shallow. These conditions are presupposed in this chapter. In the figure it is shown that a typical gravity current has a distinct head, followed by a long tail with a diffuse upper boundary. The local depth of the gravity current is defined by:

$$h(x,t) \equiv 2 \int_o^\infty z\, \Delta\rho(x,z,t)\, dz \;/\; \int_o^\infty \Delta\rho(x,z,t)\, dz \;. \qquad (II.3.1)$$

Thus the local depth is twice the local densimetric mean depth $\bar{z}(x,t)$. For our model we will use an idealised representation of a real gravity current. Our idealised gravity current has a uniform density ρ_c and all dense material is below the local depth h(x,t). The volume per unit width of the current is given by

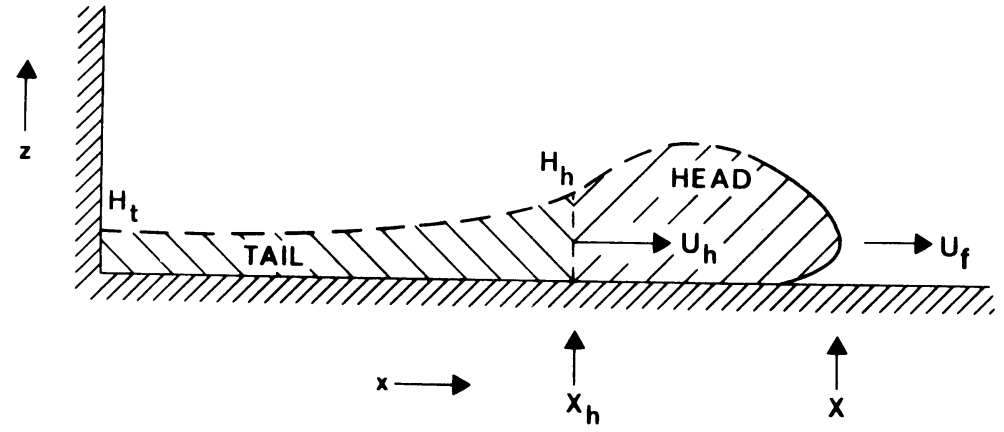

figure II.2: The unsteady gravity current.

$$V = \int_0^X h(x,t)\, dx \qquad \text{(II.3.2)}$$

and the horizontal momentum-integral per unit width is approximated by

$$M = \int_0^X \rho_c\, \bar{u}(x,t)\, h(x,t)\, dx\ , \qquad \text{(II.3.3)}$$

where $\bar{u}(x,t)$ is the layer averaged horizontal velocity. Equations for dV/dt and dM/dt form the basis of our dynamical integral model. Such equations will be derived in the sections II.3.2 and II.3.3. To obtain a full model closure also the integrals in (II.3.2) and (II.3.3) have to be evaluated. This is done in section II.3.4 for the tail region and in section II.3.5 for the head of the current. In these sections the volume and momentum of the tail and the head are expressed in terms of the length X of the current, the depth H_t in the origin, the depth H_h at the transition from tail to head and the velocity $U_f \equiv dX/dt$ of the leading edge.

II.3.2 Equations for the volume of the current

As we have seen in II.2.1 little mixing occurs through the leading edge of the gravity current. On the other hand significant mixing occurs at the top of the current behind the head. Therefore we parameterize the mixing process as:

$$dV/dt = W_e\, X\ , \qquad \text{(II.3.4)}$$

where W_e an effective entrainment velocity an X the area per unit width of the current. Thus W_eX can be interpreted as the volume flux of ambient fluid into the gravity current.

Next we will derive a parameterisation for the entrainment velocity by considering the energy budget of the current. The potential energy of the current is given by

$$PE = \int_0^X \int_0^{h(x,t)} g\, \Delta\rho_c\, z\, dz\, dx \qquad \text{(II.3.5)}$$

where

$$\Delta\rho_c = \rho_c - \rho_a \qquad \text{(II.3.6)}$$

is the average density difference between the current and the ambient fluid.

When h(x,t) does not vary too wildly with x the potential energy can be approximated by

$$PE = \tfrac{1}{2} g \Delta\rho_c V H , \qquad (II.3.7)$$

where

$$H = V/X \qquad (II.3.8)$$

is the average cloud depth.

As we have seen in Chapter I (eqn. (I.11)) the conservation of dense material implies that

$$\Delta\rho_c V = \Delta\rho_o V_o . \qquad (II.3.9)$$

Therefore

$$PE = \tfrac{1}{2} g \Delta\rho_o V_o H \qquad (II.3.10)$$

and

$$dPE/dt = \tfrac{1}{2} g \Delta\rho_o V_o (dH/dt) . \qquad (II.3.11)$$

Using (II.3.4) and (II.3.8) and using that

$$dX/dt = U_f \qquad (II.3.12)$$

it is easily shown that

$$dH/dt = - HU_f/X + W_e . \qquad (II.3.13)$$

Therefore

$$dPE/dt = - \tfrac{1}{2} g \Delta\rho_o V_o H U_f/X + \tfrac{1}{2} g \Delta\rho_o V_o W_e . \qquad (II.3.14)$$

The physical interpretation of this result is that the potential energy decreases due to slumping and increases due to entrainment. The latter process corresponds with a transformation of turbulent energy into potential energy. This transformation process is often called "the buoyant destruction of turbulence". From (II.3.14) we see that the entrainment velocity is known when the buoyant destruction is known. To find the buoyant destruction rate we make the

closure assumption that buoyant destruction is proportional to the production of turbulent kinetic energy. This assumption has led to successful modeling of entrainment in the atmosphere and ocean (e.g. Tennekes and Driedonks, 1981). The production of turbulent energy in the present case can be derived from the analysis by Simpson and Britter (1979). They showed that shear production occurs mainly in the head region of the current, while destruction of eddies mainly occurs behind the head. Near the head, eddies are created with an energy density of order $\frac{1}{2} \rho_a U_f^2$. This occurs at a volume rate of order $H_h U$. Thus the production rate should scale as $\frac{1}{2} \rho_a H_h U_f^3$. Using this we obtain for the buoyant destruction rate:

$$\frac{1}{2} g \Delta\rho_o V_o W_e = \frac{1}{2} \varepsilon \rho_a H_h U_f^3 , \qquad \text{(II.3.15)}$$

where ε is a numerical coefficient. From this result we find with (II.3.4) and (II.3.9) for the entrainment rate:

$$dV/dt = \varepsilon H_h U_f / Ri \qquad \text{(II.3.16)}$$

where

$$Ri = g\Delta\rho_c H/\rho_a U_f^2 \qquad \text{(II.3.17)}$$

is a bulk Richardson number and where ε is an empirical coefficient. this result resembles the traditional scaling of side entrainment (Van Ulden, 1974; Fay, 1980) which reads or the two-dimensional case

$$dV/dt = \alpha_e H U_f , \qquad \text{(II.3.18)}$$

where α_e is a constant. The physical meaning of our result is, however, completely different. In our model only the production of turbulent kinetic energy occurs at the leading edge, but the subsequent entrainment occurs at the top of the current. Thus turbulent eddies are mainly created near the leading edge. While travelling away from the leading edge they lose their kinetic energy and increase the potential energy of the current.

The estimation of our entrainment coefficient ε is not easy. No data seem to be available for the 2-dimensional case. As a preliminary value we will use $\varepsilon = 0.6$. This value lies within the range of entrainment coefficients found for the axisymmetric case (see chapter III for a full discussion on this subject).

II.3.3 The momentum-integral equation

In this section we will derive an equation for the horizontal momentum-integral of the gravity current by considering the momentum budget in a time varying control volume, which just encloses the gravity current. This budget reads:

$$dM/dt = - \int_0^{X+} \int_0^{h+} (\partial P/\partial x)\, dx\, dz \ . \qquad (II.3.19)$$

In this equation P is the pressure, while X+ and h+ denote, that the integrations are extended to include the outer boundary of the current. In this momentum budget it is presupposed that shear-stresses and momentum fluxes vanish at the boundaries of the control volume. In this section we will evaluate the right hand side of this momentum budget, which represents the pressure forces that act on the current.

It is convenient for this evaluation to introduce the pressure disturbance Π, which is defined as:

$$\Pi(x,z,t) \equiv P(x,z,t) - P_\infty(z) \ , \qquad (II.3.20)$$

where $P_\infty(z)$ is the pressure of the undisturbed ambient fluid at the height z. Since $\partial P_\infty/\partial x = 0$, it follows that

$$-\int_0^{X+} \int_0^{h+} (\partial P/\partial x)\, dx\, dz = -\int_0^{X+} \int_0^{h+} (\partial \Pi/\partial x)\, dx\, dz \ . \qquad (II.3.21)$$

Since $\partial h+/\partial x$ and Π at the upper boundary are small in the bulk of the current we may write:

$$-\int_0^{X+h+} (\partial \Pi/\partial x)dxdz = -\int_0^{X+} \frac{\partial}{\partial x}\left(\int_0^{h+} \Pi dz\right)dx = \int_0^{h+(0,t)} \Pi(0,z,t) - \int_0^{h+(X+,t)} \Pi(X+,z,t)dz \qquad (II.3.22)$$

Thus the pressure force on the current is determined by the pressure disturbances in the origin and at the leading edge.

Three different processes produce these pressure disturbances:

- the negative buoyancy of the dense fluid gives rise to an increase Π_s in the static pressure in the current and a corresponding static pressure force F_s;
- the advancing head of the current intrudes into stagnant ambient fluid. This produces a dynamical pressure Π_d in front of the head and a corresponding

dynamical drag force F_d;

- the acceleration of the current applies momentum changes in the ambient fluid. This leads to an acceleration reaction pressure Π_a in front of the head and a corresponding reaction force F_a.

In the following we will describe these three pressure forces.

The static pressure disturbance vanishes in X+, because no dense fluid is present at this distance from the origin. Thus the static pressure force is given by:

$$F_S = \int_o^{h+(o,t)} \Pi_s(o,z,t)\, dz \ . \qquad \text{(II.3.23)}$$

Since Π_s obeys the hydrostatic relation

$$\partial \Pi_s / \partial z = - g\Delta\rho_c \qquad \text{(II.3.24)}$$

it can be shown that the static pressure force equals:

$$F_s = \tfrac{1}{2}\, g\Delta\rho_c\, H_t^{\,2} \ , \qquad \text{(II.3.25)}$$

where $H_t = h(o,t)$ is the current depth in the origin (see fig. II.2).

The dynamic pressure vanishes in the origin. Thus the dynamic drag force is determined by the flow conditions near the leading edge. The dynamic pressure difference over the leading edge scales as $\tfrac{1}{2}\, \rho_a\, U_f^{\,2}$, while the scale depth for the leading edge is H_h (see fig. II.2). Therefore we parameterize the dynamic drag force as:

$$F_d = - \tfrac{1}{2}\, c_f\, \rho_a\, U_f^{\,2}\, H_h \ , \qquad \text{(II.3.26)}$$

where c_f is a drag coefficient of O(1) which will be estimated in section II.3.5.

The acceleration reaction force is written as:

$$F_a = - dM_v/dt \ , \qquad \text{(II.3.27)}$$

where M_v is the virtual momentum of the ambient fluid (Batchelor, 1967, 6.4). To parameterize this virtual momentum we use the resemblance between our gravity current and an elliptical cylinder with aspect ratio H/X. For such a

cylinder the virtual momentum equals $\rho_a H^2 U_f$ (Batchelor, 1967, 6.6). Therefore we parameterize M_v as:

$$M_v = \alpha \rho_a H^2 U_f , \qquad \text{(II.3.28)}$$

where α is an empirical coefficient of O(1). The exact value of this coefficient is not important for a shallow gravity current, because M_v is small in comparison with the total momentum M of the current. In this study we use $\alpha = 2$.

We are now ready for our momentum-integral equation. Using that $dM/dt = F_s + F_d + F_a$ we easily find from (II.3.25), (II.3.26) and (II.3.27) that:

$$d(M+M_v)/dt = \tfrac{1}{2} g\Delta\rho_c H_t^2 - \tfrac{1}{2} c_f \rho_a H_h U_f^2 . \qquad \text{(II.3.29)}$$

This equation and the continuity equation (II.3.16) are the bulk rate equations for the total gravity current. In these equations the volume integral (II.3.2) and the momentum integral (II.3.3) still have to be specified. We will do so in the following sections.

II.3.4 The horizontal distributions of layer depth and layer averaged velocity in the tail of the current

It is the purpose of this section to evaluate for the tail of the current the volume-integral

$$V_t(t) \equiv \int_0^{X_h} h(x,t)\, dx \qquad \text{(II.3.30)}$$

and the momentum-integral

$$M_t(t) \equiv \int_0^{X_h} \rho_c \bar{u}(x,t)\, h(x,t)\, dx \qquad \text{(II.3.31)}$$

In particular we want to express these integrals in terms of the model variables H_t, H_h, X_h and U_h. In order to do so we need approximations to the functions $h(x,t)$ and $\bar{u}(x,t)$. During the early development of the current these are difficult to obtain, but quite soon the current becomes shallow enough that the shallow layer equations are applicable to the flow in the tail of the current. In the present problem the following equations apply:

$$\frac{1}{h}\frac{Dh}{Dt} = -\frac{\partial \bar{u}}{\partial x} + \frac{w_e}{h} \qquad \text{(II.3.32)}$$

and

$$\frac{D\bar{u}}{Dt} = -g\frac{\Delta\rho_c}{\rho_c}\frac{\partial h}{\partial x} - \frac{\rho_a w_e \bar{u}}{\rho_c h} - \tfrac{1}{2}\delta\frac{\partial \bar{u}^2}{\partial x} . \qquad \text{(II.3.33)}$$

In these equations $D/Dt = \partial/\partial t + \bar{u}\,\partial/\partial x$, w_e is the local entrainment velocity and $\tfrac{1}{2}\delta\,\partial\bar{u}^2/\partial x$ a momentum flux gradient term that accounts for the fact that the horizontal velocity varies with height. δ is an empirical constant to be estimated later. It should be noted that (II.3.33) is fully consistent with our bulk equation (II.3.29), provided the current is shallow. Also in (II.3.29) an effective stress gradient term similar to that in (II.3.33) is hidden in the dM/dt term. This can be checked by evaluating the time derivative of (II.3.20). The physical meaning of the decelerating stress gradient term is simply this. Entrainment does not affect the total momentum - since no momentum is entrained -, but it increase the total mass of the current. This necessarily causes a decrease in the mean velocity. Thus entrainment leads to a deceleration term in the equation for the mean velocity. We will now derive approximate solutions to (II.3.32) and (II.3.33) by making two similarity assumptions. The first is that the shape of the current is quasi-conserved in time i.e. that

$$\frac{1}{h}\frac{Dh}{Dt} \simeq \frac{1}{H}\frac{dH}{dt} , \qquad \text{(II.3.34)}$$

virtually independent from x. The second assumption is that the layer averaged density difference remains horizontally uniform and equal to $\Delta\rho_c$. This requires that

$$w_e/h \simeq W_e/H , \qquad \text{(II.3.35)}$$

virtually independent from x (see also section II.3.1). It then follows that

$$\partial\bar{u}/\partial x \simeq U_h/X_h \qquad \text{(II.3.36)}$$

and that

$$\bar{u} \simeq x\,U_h/X_h \qquad \text{(II.3.37)}$$

It also follows from (II.3.33)-(II.3.37) that $\partial h/\partial x$ is a linear function of x that vanishes in $x = 0$. Using the boundary conditions $h = H_t$ for $x = 0$ and $h = H_h$ for $x = X_h$, we now easily find that

$$h = H_t + (H_h - H_t)\,(x/X_h)^2 \qquad \text{(II.3.38)}$$

The solutions for $\bar{u}$ and h happen to be of the same form as those obtained by Fanneløp and Waldman (1971, 1972). However there are two differences. In our model H_t and H_h are independent variables that are determined by the dynamics of the gravity current. Further we use (II.3.37) and (II.3.38) only to estimate the volume and momentum integrals of the tail. From (II.3.30), (II.3.31) and (II.3.37), (II.3.38) we easily obtain

$$V_t = \frac{1}{3}\,(2\,H_t + H_h)\,X_h \qquad \text{(II.3.39)}$$

and

$$M_t = \frac{1}{4}\,\rho_c\,(H_t + H_h)\,X_h\,U_h \qquad \text{(II.3.40)}$$

This completes our description of the tail.

II.3.5 The head of the current

The shallow layer equations are not applicable to the head of the current. Instead we use the momentum-integral approach that we applied to the total current (II.3.19). The force balance for the head looks as follows. The static pressure force follows from the integration of the static pressure gradient over the head region and equals:

$$F_s = \tfrac{1}{2}\,g\Delta\rho_c\,H_h^2 \qquad \text{(II.3.41)}$$

The dynamic pressure force is

$$F_d = -\tfrac{1}{2}\,c_f\,\rho_a\,H_h\,U_f^2\ . \qquad \text{(II.3.42)}$$

Furthermore there is a momentum flux into the head due to the internal current in the head (figure II.1). Near the surface the inward flow U_4 carries positive momentum into the head. The return flow U_3 carries negative momentum out the head. So the net effect of the internal flow is a positive momentum flux into the head. Assuming $U_3 = U_4$ and $h_4 = \tfrac{1}{2}\,H_h$ we find that this flux is crudely

$$Q_h = \rho_a\,H_h U_4^2 \qquad \text{(II.3.43)}$$

Using $U_4 = 0.2\ U_f$ (II.2.1) we may write this as

$$Q_h = \tfrac{1}{2}\ \delta\ \rho_a\ H_h\ U_f^2 \qquad \text{(II.3.44)}$$

where

$$\delta = 0.08\ . \qquad \text{(II.3.45)}$$

Thus δ is an empirical coefficient which characterizes the non-uniformity of the vertical velocity profile. It has the same meaning as in (II.3.37).

We neglect the inertial terms in the momentum-integral equation for the head. It can be shown that these terms are normally small in comparison with the other terms. Thus we assume that the head is in a quasi-steady state. This assumption is supported by experiment. We have seen in section II.2.1 that the dimensionless leading edge velocity $C_h = 1.15 \pm 0.05$ both for steady and for unsteady currents (II.2.4). Our momentum-integral equation now reads:

$$0 = \tfrac{1}{2}\ g\Delta\rho_c H_h^2 - \tfrac{1}{2}\ c_f \rho_a H_h U_f^2 - \tfrac{1}{2}\ \delta \rho_a H_h U_f^2 \qquad \text{(II.3.46)}$$

It follows from this equation that the dimensionless velocity C_h defined by (II.2.2) is given by

$$C_h = 1\ /\ \sqrt{c_f - \delta}\ . \qquad \text{(II.3.47)}$$

Since C_h and δ are known, the value of c_f can be estimated from this equation. The result is

$$c_f = 0.84 \pm 0.07 \qquad \text{(II.3.48)}$$

With (II.3.44)-(II.3.48) we have specified the important dynamical leading-edge boundary conditions.

We conclude this section with the specification of the volume and momentum of the head. We allow the volume of the head to vary in time, but assume that its shape remains unchanged. In section II.2 we have seen that the depth H_1 of the head is about twice the depth H_h behind it. We also assume that its length scales with H_h. Thus we write

$$X - X_h = a\ H_h\ . \qquad \text{(II.3.49)}$$

Experimental data suggest that a ≈ 2. The volume of the head now is written as

$$V_h = b\, H_h^2 \ , \qquad \text{(II.3.50)}$$

where b ≈ 4. To estimate the momentum of the head we assume that (as in the tail) the layer averaged velocity increases linearly with x. It then follows that

$$U_h = U_f X_h / X \ . \qquad \text{(II.3.51)}$$

Using (II.3.49)-(II.3.51) we find for the momentum of the head.

$$M_h = b\rho_c\, U_f H_h^2\, (X - \tfrac{1}{2}\, a\, H_h)/X \ . \qquad \text{(II.3.52)}$$

This completes our description of the head. Together, the bulk equations derived in II.3.2 and II.3.3 and the equations for the tail and the head derived in II.3.4 and II.3.5 form a closed set. We will summarize the final set of equations in the next section.

II.3.6 Final model equations

In the final model equations we use the dimensionless density difference $\Delta^* = \Delta\rho_c/\rho_a$ and the velocity integral $M^* = (M_t+M_h+M_v)/\rho_a$. The model has 7 variables, i.e. X, V, M^*, U_f, H_h, H_t and Δ^* and 7 equations, namely 3 rate equations and 4 diagnostic equations. These follow now. The first rate equation results from the definition of U_f and reads:

$$dX/dt = U_f \ . \qquad \text{(II.3.53)}$$

The second rate equation follows from (II.3.4) and (II.3.15):

$$dV/dt = \varepsilon\, H_h X U_f^3 / g\Delta^*_o V_o \ , \qquad \text{(II.3.54)}$$

where ε ≈ 0.6 is an entrainment coefficient, and Δ^*_o and V_o are the initial values of Δ^* and V. The third rate equation follows from (II.3.29):

$$dM^*/dt = \tfrac{1}{2}\, g\Delta^*\, H_t^2 - \tfrac{1}{2}\, c_f\, H_h U_f^2 \ , \qquad \text{(II.3.55)}$$

where $c_f \approx 0.84 \pm 0.07$. These equations determine the development of X, V and M^*. The other variables follow from the diagnostic equations. From (II.3.8), (II.3.28), (II.3.40), (II.3.49), (II.3.51) and (II.3.52) we find that the leading edge velocity is:

$$U_f = \frac{M^* X}{(1+\Delta^*)\left[\frac{1}{4}(H_t+H_h)(X-aH_h)^2 + bH_h^2(X-\frac{1}{2}aH_h)\right] + \alpha V^2/X} \qquad \text{(II.3.56)}$$

where $a \approx 2$, $b \approx 4$ and $\alpha \approx 2$. The depth of the leading edge follows from (II.3.47):

$$H_h = (c_f-\delta)U_f^2/g\Delta^* \ , \qquad \text{(II.3.57)}$$

where $\delta \approx 0.08$. The depth at the origin follows from (II.3.39), (II.3.49) and (II.3.50):

$$H_t = \frac{3}{2}(V - bH_h^2)/(X-aH_h) - \tfrac{1}{2}H_h \ . \qquad \text{(II.3.58)}$$

From (II.3.9) we get the relative density difference

$$\Delta^* = \Delta^*_o V_o/V \qquad \text{(II.3.59)}$$

This completes our model. The time development of the 8 variables of the model is obtained by numerical integration of the three rate equations (II.3.53)-(II.3.55) with respect to time. This yields X, V and M^* as a function of time. The other variables are obtained from the diagnostic equations (II.3.56)-(II.3.59).

II.4 Some general model results

In this section we describe some model results. We will present our computations in dimensionless form. From the momentum equation it follows that the appropriate dimensionless time τ is

$$\tau = t/t_o \ , \qquad \text{(II.4.1)}$$

where

$$t_o \equiv X_o / \sqrt{g\Delta^*_o H_o} \qquad \text{(II.4.2)}$$

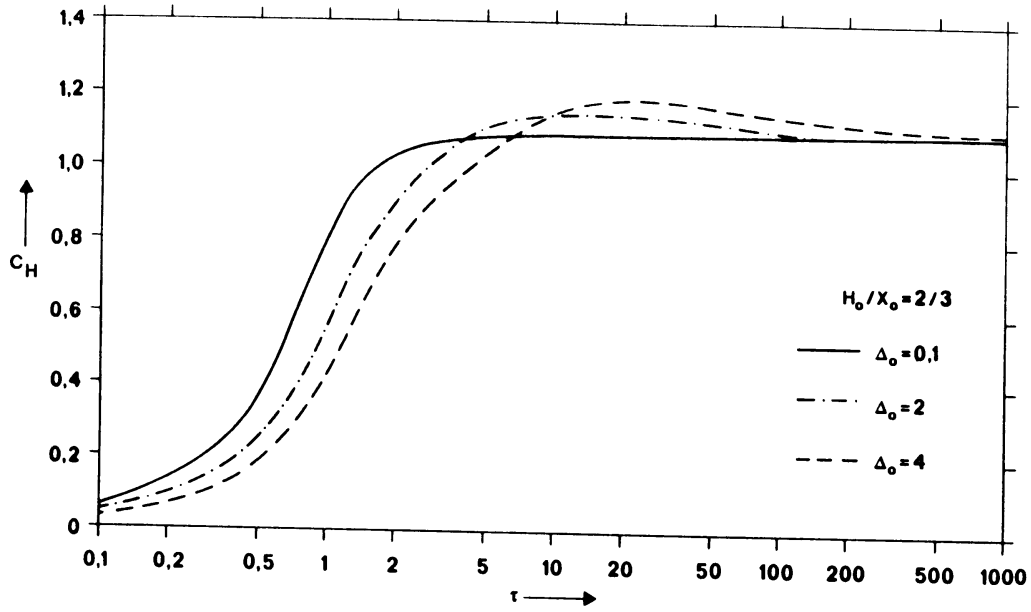

figure II.3: The dimensionless velocity as a function of dimensionless time.

is a time scale. The subscripts o denote initial values. In the time scale t_o two length scales are involved, i.e. X_o and H_o. Thus our scaling differs from that by Fanneløp and Waldman (1972) and by Hoult (1972), who used only one length scale $L_o = \sqrt{V_o}$ and neglected variations in the initial aspect ratio H_o/X_o.

We will present some computations made with the values of the empirical constants given in the last section, for a release with $H_o/X_o = 2/3$. In our model this corresponds with initial values for H_t/X and H_h/X of 1 and 0 respectively. In figure II.3 we show the dimensionless velocity

$$C_H = U_f/(g\Delta^* H)^{\frac{1}{2}} \qquad \text{(II.4.3)}$$

as a function of the dimensionless time τ for $\Delta^*_o = 0.1$, 2 and 4. It appears that for $\Delta^*_o = 0.1$ the velocity approaches rapidly an asymptotic value $C_\infty = 1.1$. In terms of C_H the initial acceleration of the current is almost completed when $\tau = 2$. Thus t_o is a characteristic time scale which crudely separates the acceleration phase from the deceleration phase (because U decreases when C_H is constant). For high initial values of Δ^*, the acceleration phase lasts longer, but after it the dimensionless velocity reaches temporarily higher values. For very large times C_H again approaches the asymptotic value C_∞. The latter feature can be attributed to entrainment, that leads to a vanishing Δ^* at large times.

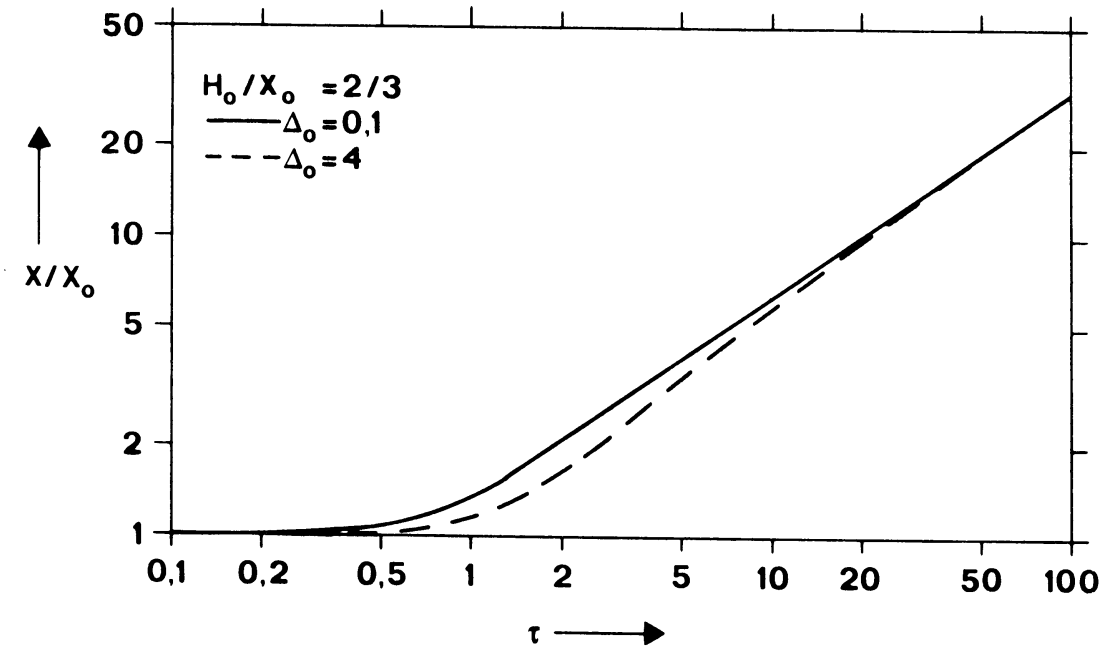

figure II.4: The dimensionless current length as a function of dimensionless time.

In figure II.4 we give the dimensionless current length X/X_o. The effect of Δ^*_o on X/X_o is moderate. In figure II.5 we present the dimensionless volume concentration V_o/V as a function of X/X_o. Here, too, the effect of Δ^*_o is moderate. More interesting is that entrainment does not start immediately with the spreading of the dense fluid. This is due to the initial delay in the creation of turbulence.

We have also tested the sensitivity of the model to variations in the head size coefficients a and b and in the coefficient c for the virtual inertia. It appears that the model results are almost invariant for changes in a and b even as large as a factor 2. Changes in α have some effect. E.g. using $\alpha = 1$ instead of $\alpha = 2$ leads to higher velocities for $\tau < 1$ and lower velocities for $1 < \tau < 10$. There is no net effect on X/X_o for $\tau > 10$. On the other hand there is a notable effect on the concentration even for large times. For $\tau > 10$ the concentration is about 10% higher with $\alpha = 1$ than with $\alpha = 2$. This is due to a lower entrainment rate in the period $1 < \tau < 10$.

The model sensitivity to c_f, δ and ε will be discussed in the next section.

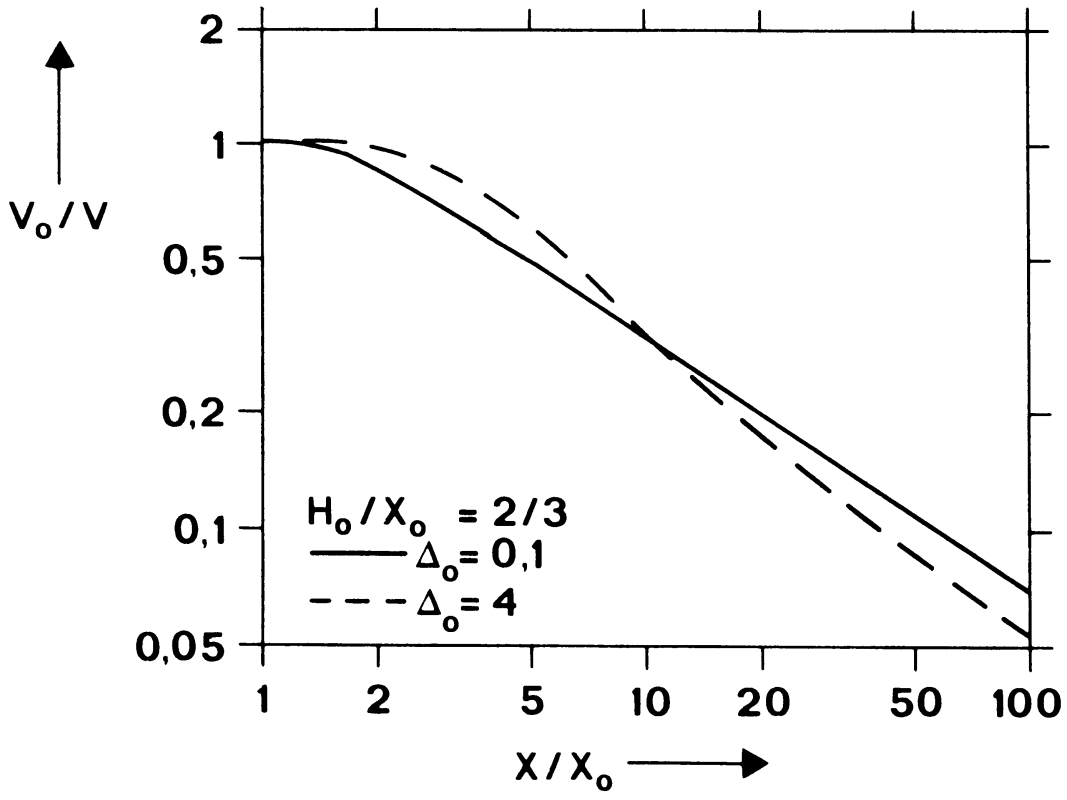

figure II.5: The dimensionless volume concentration as a function of dimensionless current length.

II.5 The momentum budget for great times

Sooner or later - this depends on the value of Δ^*_o - the dimensionless velocity C_H will approach its asymptotic value C_∞. This occurs when $\Delta^* \ll 1$ and $H/X \ll 1$. When this is the case the velocity integral M^* reduces to

$$M^* = \tfrac{1}{4}\left(\frac{H_t}{H} + \frac{H_h}{H}\right) VU_f \ . \qquad \text{(II.5.4)}$$

Furthermore when C_H is constant also H_t/H and H_h/H are constant. It then follows that

$$\frac{dM^*}{dt} = \tfrac{1}{4}\left(\frac{H_t}{H} + \frac{H_h}{H}\right) V \frac{dU_f}{dt} + \tfrac{1}{4}\left(\frac{H_t}{H} + \frac{H_h}{H}\right) U_f \frac{dV}{dt} \ . \qquad \text{(II.5.5)}$$

The first term at the right side is the inertial force due to the deceleration of the current and the second term the vertical stress gradient due to entrainment. With this result the momentum equation (II.3.55) can be transformed into

an equation with a single unknown i.e. C_∞. Dividing (II.3.55) by $\frac{1}{2} g\Delta^* H^2$, using (II.3.57) and (II.3.58) to eliminate H_h/H and H_t/H and using (II.4.3) we arrived at the following equation:

$$-\frac{1}{8}[3 + (c_f-\delta)C_\infty{}^2]C_\infty{}^2 + \frac{1}{4}\varepsilon(c_f-\delta)[3 + (c_f-\delta)C_\infty{}^2]C_\infty{}^6$$

$$= \frac{9}{4} - \frac{3}{2}(c_f-\delta)C_\infty{}^2 + \frac{1}{4}(c_f-\delta)^2 C_\infty{}^4 - c_f(c_f-\delta)C_\infty{}^4 . \qquad \text{(II.5.6)}$$

The first term at the left represents the dimensionless inertial force F^*_i, the second term the stress F^*_s, the first three terms at the right the static pressure force F^*_p and the last term the dynamic force F^*_d. For given values of c_f, δ and ε (II.5.6) can be solved for $C_\infty{}^2$. For $c_f = 0.84$, $\delta = 0.08$ and $\varepsilon = 0.6$ the solution is $C_\infty{}^2 = 1.2$ or $C_\infty = 1.094$. The magnitude of the various terms of (II.5.6) is $F^*_i = -0.58$; $F^*_s = 0.76$; $F^*_p = 1.09$; $F^*_d = -0.91$. In addition it follows that $H_t \approx H_h \approx H$. This implies that the static pressure varies little over the current and that the static pressure force mainly acts at the leading edge, where it is approximately balanced by the dynamical force on the head. In the bulk of the current the inertial force is approximately balanced by the shear stress due to entrainment. Thus the shear stress has a significant effect on the dynamics of the gravity current.

We may also use the asymptotic equation (II.5.6) to evaluate the sensitivity of the model to variations in the empirical constants c_f, δ and ~. It appears that C_∞ is most sensitive to variations in the value of $c_f-\delta$. A 10% increase in $c_f-\delta$ corresponds with a 4% decrease in C_∞. Further we found that a 10% increase in ε corresponds with a 1% decrease in C_∞. The model is quite insensitive to variations in δ. A 100% increase in δ (with $c_f-\delta$ kept at the same value) leads to a 1% decrease in C_∞.

II.6 Summary and conclusions

We have developed a model for the spreading of a dense fluid in an infinitely deep channel. The model consists of rate equations for the length, the momentum-integral and the volume of the resulting gravity current. Diagnostic equations describe the shape of the current and the velocity distribution in it. The model is non-hydrostatic. The Boussinesq approximation has not been made. This makes the model suited to desribe currents with a density that is considerable higher than that of the ambient fluid. A new parameterization of

entrainment is proposed, which does not violate the conservation law for potential and kinetic energy. The model contains six empirical coefficients that have been estimated as well as possible from literature data. A new dimensionless representation has been proposed. In this representation the dimensionless velocity, length and volume are within moderate limits universal functions of the dimensionless time. The model is mathematically rather simple and physically rather complete. A definite test of the model against well-documented experimental data still has to be made. From a physical point of view the model is a significant advance over the similarity approach by Fanneløp and Waldman (1972) and over the crude dynamical approach by Van Ulden (1979).

One of the interesting results of the present model is that it throws light on the effect of entrainment on the spreading dynamics. We have found that the vertical stress gradient due to entrainment approximately balances the inertial force due to decelerations. This suggests that the current depth is relatively uniform (apart from the head near the leading edge). This finding also suggests that it is justified to describe the unsteady gravity current by means of a box model, provided the proper bulk dynamics are included in the model.

Chapter III

THE SPREADING AND MIXING OF A DENSE AXISYMMETRIC CLOUD IN STILL AIR

III.1 Introduction

III.1.1 Scope

This chapter deals with isothermal dense gas clouds spreading axisymmetrically over a smooth horizontal surface in still air. The initial state is a quiescent cylindrical cloud with volume V_o, radius R_o and height H_o. Its density ρ_o is uniform and greater than the air density ρ_a by an amount $\Delta\rho_o = \rho_o - \rho_a$. The cloud temperature is equal to the ambient temperature, so this density difference is purely due to the higher mean molecular weight of the gas.

III.1.2 Historical background

In the first generation integral models (e.g. Van Ulden, 1974 and Chapter I) the cloud is represented by a cylinder with radius R, height H and a uniform relative density difference Δ between the cloud and the ambient air. The radial spreading is approximated by a simple similarity relation for the front velocity:

$$U_f \equiv dR/dt = k\sqrt{gH\Delta} \ , \qquad \text{(III.1.1)}$$

where t is the time, k an empirical constant of order 1 and g the acceleration due to gravity. The mixing process is usually described with an equation of the form:

$$dV/dt = \pi R^2 W_e + 2\pi RHU_e \ , \qquad \text{(III.1.2)}$$

where V is the volume of the cloud and W_e, U_e entrainment velocities for mixing at the top and at the front edge of the cloud. Usually W_e and U_e are taken to be proportional to the front velocity U_f.

This simple approach has been fairly successful, especially in describing the later stages of radial spreading. The acceleration from rest, however, is not described by (III.1.1) and its range of applicability is not clear. Even more problems have arisen with the description of the mixing process with

(III.1.2). It appears that mixing through the cloud edge is small and cannot account for the observed mixing, while a top entrainment with $W_e \propto U_f$ leads to a violation of the energy budget (Fay, 1980). A more general problem is that the physical basis is incomplete for the first generation integral models.

Therefore attempts have been made to improve on this. E.g. Fanneløp and Waldman (1971), Van Ulden (1979), Byggstøyl and Saetran (1983) have proposed models that describe the spreading process by momentum equations with suitable boundary conditions for the leading edge. In these models, however, vertical accelerations in the cloud and the reaction of ambient fluid to accelerations of the front edge and of the top of the cloud have been neglected. Therefore these models are not capable of describing the early spreading stage, when the cloud is not shallow. Moreover, in these models the entrainment is either neglected or treated in an ad hoc manner.

An improvement on this is the model by Van Ulden (1984) for a two-dimensional gravity current (see chapter II) and a similar model by Havens and Spicer (1985) for an axisymmetric cloud. In these models acceleration reactions are included in the momentum budget. Entrainment is modelled by assuming that edge production of turbulent energy and buoyant destruction of this energy are proportional. This corresponds with $W_e \propto \bar{u}_t^3 / gH\Delta \propto U_f^3/gR\Delta$, where $\bar{u}_t$ is a turbulent velocity scale. With (III.1.1) this led Van Ulden to the conclusion that top entrainment scales like edge entrainment, which solves the energy problem discussed by Fay (1980) (see section II.3.2).

In these models vertical accelerations in the cloud are still neglected. Additionally the turbulent energy budget is still incomplete and not satisfactory, because the destruction of turbulence should lag behind its production.

Therefore we go two steps further in the present chapter. In the first place we will account for vertical accelerations in the cloud. In the second place we will include in the model a fully time dependent turbulent kinetic energy budget and a separate entrainment model taken from Driedonks and Tennekes (1984). The latter model describes the relation between entrainment and turbulent kinetic energy. In this manner we will avoid an undesirable number of ad hoc empirical coefficients in the description of entrainment. The structure of this chapter is the following. In section 2 we describe the general model structure. In section 3 we analyse the momentum budget and derive an equation for the radial momentum-integral. In section 4 we analyse the energy budget and derive an equation for the turbulence generated by the cloud. In section 5 we compare the model with experimental data. In section 6 we discuss the model properties. Section 7 gives our conclusions.

III.2 The general model structure

In the present model the cloud dimensions are defined by means of its radius R and its volume V. The cloud radius is obtained by numerical integration with respect to time of the rate equation:

$$dR/dt = U_f \qquad \text{(III.2.1)}$$

The spreading velocity U_f is derived by numerical integration of an equation for dU_f/dt that we will derive from the radial momentum budget of the cloud in section III.3.

The time rate of change of the cloud volume is modelled as

$$dV/dt = \pi R^2 W_e \ , \qquad \text{(III.2.2)}$$

where W_e is an entrainment velocity. We neglect edge entrainment and describe W_e by means of the entrainment model of Driedonks and Tennekes (1984). This model reads:

$$W_e = c_e \bar{u}_t \ / \ (c_t + Ri_t) \qquad \text{(III.2.3)}$$

where $c_e = 0.2$ and $c_t = 1.5$ are empirical coefficients given by the authors,

$$Ri_t = g \ \overline{\Delta\rho} \ H \ / \ \bar{\rho} \ \bar{u}_t^{\,2} \qquad \text{(III.2.4)}$$

is a bulk turbulent Richardson number and $\bar{u}_t$ is a bulk turbulent velocity scale defined by the total turbulent kinetic energy T_E in the entraining turbulent layer. In the present flow configuration this corresponds with the following definition

$$\bar{u}_t = (2T_E \ / \ \bar{\rho} \ V)^{\frac{1}{2}} \qquad \text{(III.2.5)}$$

or

$$T_E = \tfrac{1}{2} \ V \ \bar{\rho} \ \bar{u}_t^{\,2} \ . \qquad \text{(III.2.6)}$$

In the present model T_E is obtained by numerical integration of an equation for dT_E/dt which we will derive from the energy budget of the cloud in section III.4.

Given the cloud dimensions, R and V, some other important variables can be obtained from simple diagnostic equations. The cloud height is defined as:

$$H = V / \pi R^2 \ . \qquad \text{(III.2.7)}$$

The average density difference between cloud and air is obtained from

$$\overline{\Delta\rho} = \Delta\rho_o \, V_o / V \ , \qquad \text{(III.2.8)}$$

where $\Delta\rho_o$ and V_o are the initial values of $\overline{\Delta\rho}$ and V and where we have used that the total mass surplus $\overline{\Delta\rho}\ V$ is a conserved quantity for an isothermal cloud (chapter II). The average cloud density is given by

$$\bar{\rho} = \rho_a + \overline{\Delta\rho} \ , \qquad \text{(III.2.9)}$$

where ρ_a is the air density.

To facilitate the analysis of the cloud dynamics we will use an idealized cloud representation. We assume that the cloud is cylindrical and that its density is uniform and equal to $\bar{\rho}$. For a real cloud the density distribution will not be uniform, so a proper definition of our model variables in terms of observable quantities is needed. For the cloud radius this is no problem, because for a real cloud the cloud edge is quite sharp and directly observable. Its distance from the cloud centre of mass can be compared directly with the cloud radius of our model. The cloud height is more of a problem because mixing leads to a very diffuse cloud top. This calls for an integral definition of cloud height. We will derive such a definition from the mean height $\langle z \rangle$ of dense material in the cloud, which is:

$$\langle z \rangle \equiv {}_o\int^{\infty} {}_o\int^{\infty} z \, \Delta\rho(z,r) \, 2\pi r \, dr \, dz \ / \ \Delta\rho_o \, V_o \ . \qquad \text{(III.2.10)}$$

This "densimetric mean height" can be "observed" by measuring vertical profiles of density. It is directly related to the potential energy of the cloud, which is:

$$P_E \equiv {}_o\int^{\infty} {}_o\int^{\infty} g \, z \, \Delta\rho(z,r) \, 2\pi r \, dr \, dz = g \, \Delta\rho_o \, V_o \, \langle z \rangle \ . \qquad \text{(III.2.11)}$$

Next we define the "cloud height" in our model as:

$$H = 2 \langle z \rangle \ . \qquad \text{(III.2.12)}$$

This definition can be seen as a "sophisticated" definition of a box-model height. It has the following properties:

- It corresponds exactly with the height of a cylinder with uniform density.
- It is consistent with the height definition, used by Driedonks and Tennekes (1984) and therefore with III.2.2, III.2.3 and III.2.7.
- It is an observable quantity for a cloud with a diffuse top.
- Like $\langle z \rangle$, it is uniquely and simply related to the potential energy of the cloud; namely by:

$$P_E = \tfrac{1}{2} g \Delta\rho_o V_o H \ . \qquad \text{(III.2.13)}$$

Next we consider concentrations. The cloud-averaged concentration by volume is

$$\overline{C} = V_o/V \ . \qquad \text{(III.2.14)}$$

This is the concentration variable predicted directly by our integral model. When this volume- averaged concentration is to be compared with locally observed concentrations, spatial concentration variations should be accounted for. In the present model we do not resolve radial variations in the vertical structure, but we do allow for non-uniform vertical concentration profiles. In general the area-averaged concentration C(z) can be described by profiles of the type

$$C(z)/\overline{C} = f(z/H) \ , \qquad \text{(III.2.15)}$$

where z is the height above the surface and f(z/H) a function of the scaled height z/H. This function has to satisfy several constraints.

In the first place the total volume of dense gas should be conserved. This implies:

$$\int_0^\infty f(\tfrac{z}{H})\, d(\tfrac{z}{H}) = 1 \ . \qquad \text{(III.2.16)}$$

Furthermore this function has to be consistent with the definition of H, which gives the constraint:

$$\int_0^{\infty} \left(\frac{z}{H}\right) f\left(\frac{z}{H}\right) d\left(\frac{z}{H}\right) = \tfrac{1}{2} \qquad \text{(III.2.17)}$$

Candidates for the scaled concentration profiles (III.2.16) are profiles of the family

$$f(z/H) = A \exp\left[-(Bz/H)^s\right] , \qquad \text{(III.2.18)}$$

where s is a profile shape factor and where

$$A = 2s\, \Gamma(2/s) \,/\, [\Gamma(1/s)]^2 \qquad \text{(III.2.19A)}$$

and

$$B = 2\, \Gamma(2/s) \,/\, \Gamma(1/s) . \qquad \text{(III.2.19B)}$$

Γ is the gamma function. This profile family satisfies the constraints (III.2.16) and (III.2.17). Furthermore profiles from this family have been observed (Nieuwstadt and Van Ulden, 1978) and can be obtained as solutions of the diffusion equation (Chatwin, 1968; Van Ulden, 1978; Hunt and Weber, 1979; Van Ulden and Nieuwstadt, 1980). The family includes the uniform profile ($s = \infty$, $A = 1$, $B = 2$) the gaussian profile ($s = 2$, $A = 4/\pi$, $B = 2/\sqrt{\pi}$) and the exponential profile ($s = 1$, $A = 2$, $B = 2$).

It should be noted that the present model, being an integral model, cannot solve explicitly for the concentration profile. Our model only computes bulk quantities like H and $\overline{C}$. The translation of these quantities into concentration profiles has to be made with an empirical choice for f(z/H). This will be a matter of discussion in section 5. Here we continue with a description of the momentum budget and the energy budget of the cloud that have to provide us with equations for dU_f/dt and dT_E/dt.

III.3 The momentum-integral equation

The equation of motion in its most general integral-form reads

$$\frac{d}{dt} \int_{V_c} \rho u_i \, dv = \phi_i + \int_{V_c} \rho\, g_i \, dv + \int_{V_c} \frac{\partial \sigma_{ij}}{\partial x_j} \, dv . \qquad \text{(III.3.1)}$$

In this equation V_c is an arbitrary control volume, that is allowed to vary continuously in time, ρu_i are the components of the instantaneous momentum density, ϕ_i the flux of momentum into the volume, g_i the volume force (in casu

the acceleration by gravity) and σ_{ij} the stress tensor. The equation can be derived from equations given by Batchelor (1967, 3.2). We have selected this form of the momentum equation, because it is appropriate for the present problem of a cloud, that changes both in shape and in volume.

In this section we use this momentum-integral equation to derive an equation for the radial acceleration dU_f/dt of the cloud edge. To this end we apply the momentum-integral equation to the radial velocity component u_r in a control volume with boundaries just outside our idealized cylindrical cloud. Since gravity works only vertically, the volume force vanishes in the radial momentum equation. Moreover in our idealized flow configuration the flux ϕ_r of radial momentum and the shear stresses are presupposed to be negligible at the boundaries of the control volume. So ϕ_r and the off-diagonal components of the stress tensor vanish also. Therefore the radial component of the momentum-integral equation reduces to:

$$\frac{d}{dt} \int_0^{R+} \int_0^{H+} \bar{\rho}\, \bar{u}_r \, 2\pi r \, dr \, dz = - \int_0^{R+} \int_0^{H+} \frac{\partial P}{\partial r} \, 2\pi r \, dr \, dz \; . \qquad \text{(III.3.2)}$$

In this equation R+ and H+ denote that the boundaries of the integration domain lie just outide the cloud, $\bar{u}_r$ is the annulus-averaged radial velocity and $P \equiv -\sigma_{rr}$ is the pressure. The left hand side of this equation gives the time rate of change of the radial momentum-integral M_r. For the evaluation of this integral we need the functional relationship $\bar{u}_r(r)$. This is easily obtained from the continuity equation as

$$\bar{u}_r(r) = rU_f/R \; . \qquad \text{(III.3.3)}$$

Using this it follows that

$$M_r \equiv \int_0^{R+} \int_0^{H+} \bar{\rho}\, \bar{u}_r(r) \, 2\pi r \, dr \, dz = \frac{2}{3} \bar{\rho} \, V \, U_f \; . \qquad \text{(III.3.4)}$$

Taking the time derivative of this equation and using (III.2.2), (III.2.7), (III.2.8) and (III.2.9) we easily find that

$$\frac{2}{3} \bar{\rho} \, V \frac{dU_f}{dt} = \frac{dM_r}{dt} - \frac{2}{3} \rho_a \, V \frac{W_e U_f}{H} \; . \qquad \text{(III.3.5)}$$

From the last term in this equation we see that the spreading rate of the cloud is reduced by entrainment. This is due to the fact that for a given value of

M_r, this momentum-integral is distributed over an increasing mass, which corresponds with a decreasing radial velocity. The actual deceleration occurs by way of a vertical gradient in the radial shear stress in the cloud. From (III.3.5) we see that the average value of this gradient equals $-\frac{2}{3}\rho_a W_e U_f/H$.

Next we proceed with the evaluation of the right hand side of the momentum-integral equation (III.3.2), which represents the pressure force that determines dM_r/dt. For the evaluation of the pressure force it is convenient to introduce the pressure disturbance

$$\Pi(r,z,t) \equiv P(r,z,t) - P_\infty(z) \ , \qquad \text{(III.3.6)}$$

where $P_\infty(z)$ is the pressure of the undisturbed ambient fluid at the height z. $P_\infty(z)$ is presupposed to be independent of r. Therefore we may write the momentum-integral equation as:

$$\frac{dM_r}{dt} = -\int_0^{R+}\int_0^{H+} \frac{\partial \Pi}{\partial r}\, 2\pi r \, dr \, dz \ . \qquad \text{(III.3.7)}$$

Integrating the right hand side of this equation with respect to r, we find that

$$\frac{dM_r}{dt} = 2\pi R \int_0^{H+} [\bar{\Pi}(z,t) - \Pi(R_+,z,t)] \, dz \qquad \text{(III.3.8)}$$

where

$$\bar{\Pi}(z,t) \equiv \frac{1}{R+}\int_0^{R+} \Pi(r,z,t) \, dz \qquad \text{(III.3.9)}$$

is the radially averaged pressure disturbance in the cloud. In the following we will approximate this radially averaged pressure disturbance by its area-averaged value.

The area-averaged pressure disturbance $\bar{\Pi}(z,t)$ is determined by two processes:

- The negative buoyancy of the dense fluid gives rise to an average increase $\bar{\pi}_s$ in the static pressure in the cloud and a corresponding <u>static pressure force</u> F_s.
- Vertical accelerations in and above the cloud produce an average non-hydrostatic pressure $\bar{\Pi}_v$ in the cloud and a corresponding <u>non-hydrostatic pressure force</u> F_v.

The pressure disturbance $\Pi(R+,z,t)$ at the cloud edge is also due to two processes:

- The spreading cloud edge intrudes into stagnant ambient fluid. This leads to a dynamical pressure Π_d at the cloud edge and a corresponding dynamical force F_d.
- Radial accelerations of the cloud give rise to additional accelerations in the ambient fluid and a corresponding acceleration reaction force F_a.

In terms of these pressure forces the momentum-integral equation reads:

$$dM_r/dt = F_s + F_v + F_d + F_a \ . \qquad \text{(III.3.10)}$$

In the following we will evaluate the four pressure forces.

The static pressure force F_S is easily determined by using the hydrostatic relation for the static pressure disturbance. This relation reads:

$$\partial \bar{\Pi}_s/\partial z = - g \overline{\Delta\rho} \ . \qquad \text{(III.3.11)}$$

Integrating this equation with respect to z and using that $\bar{\Pi}_s$ vanishes for $z \geq H$ we find that

$$\bar{\Pi}_s = g \overline{\Delta\rho} \ (H-z) \qquad \text{for } 0 \leq z \leq H \ . \qquad \text{(III.3.12)}$$

Therefore the static pressure force is simply given by

$$F_s \equiv 2\pi R \int_0^H \bar{\Pi}_s \, dz = \pi R \, g \, \overline{\Delta\rho} \, H^2 \ . \qquad \text{(III.3.13)}$$

The evaluation of the non-hydrostatic pressure force F_v is considerably more complicated. The area-averaged non-hydrostatic pressure $\bar{\Pi}_v$ can be computed by applying the vertical component of the momentum-integral equation (III.3.1) to a cylindrical control volume between the heights H(t) and z(t). Here z(t) is a time varying height such that z(t)/H(t) is fixed in time. For this control volume the equation for the vertical momentum-integral reads:

$$\frac{dM_z}{dt} = \phi(H) - \phi(z) - \int_z^H g\bar{\rho} dz' - \pi R^2 \, [\bar{P}(H) - \bar{P}(z)] \qquad \text{(III.3.14)}$$

where

$$M_z \equiv \int_{z(t)}^{H(t)} \pi R^2 \, \bar{\rho} \, \bar{w} \, dz'(t) \qquad \text{(III.3.15)}$$

is the vertical momentum-integral, $\bar{w}$ the area-averaged vertical fluid-velocity, $\phi(H)$ and $\phi(z)$ the downward fluxes of momentum through the upper and lower

boundary of the control volume and $\bar{P}(H)$ and $\bar{P}(z)$ the averaged pressure at these two boundaries. Because the non-hydrostatic pressure $\bar{\Pi}_v$ is related to the total pressure $\bar{P}$ by

$$\partial\bar{P}/\partial z = \partial\bar{\Pi}_v/\partial z - g\bar{\rho} \ , \qquad \text{(III.3.16)}$$

the momentum equation (III.3.14) can be written as:

$$\frac{dM_z}{dt} = \phi(H) - \phi(z) - \pi R^2 \, [\bar{\Pi}_v(H) - \bar{\Pi}_v(z)] \ . \qquad \text{(III.3.17)}$$

For the evaluation of the momentum-integral M_z we need the z dependence of $\bar{w}(z)$. This is easily obtained from the continuity equation for the control volume as:

$$\bar{w}(z) = z \, \bar{w}(H)/H \qquad \text{(III.3.18)}$$

where

$$\bar{w}(H) = - 2 \, H \, U_f/R \qquad \text{(III.3.19)}$$

is the area-averaged vertical fluid velocity at the cloud top. Using this we find that the momentum-integral (III.3.15) equals:

$$M_z = - (\bar{\rho} \, V \, U_f \, H/R) \, [1 - (\frac{z(t)}{H(t)})^2] \ . \qquad \text{(III.3.20)}$$

The momentum fluxes $\phi(H)$ and $\phi(z)$ are related to the entrainment of ambient fluid. Since the vertical momentum density of the ambient fluid just above the cloud top equals $\rho_a \, \bar{w}(H)$, the momentum flux $\phi(H)$ equals:

$$\phi(H) = + \pi R^2 \, W_e \, \rho_a \, \bar{w}(H) \qquad \text{(III.3.21)}$$

or with (III.3.21):

$$\phi(H) = - 2\pi R \, H \, \rho_a \, W_e \, U_f \ . \qquad \text{(III.3.22)}$$

Similarly, because the effective entrainment velocity $w_e(z)$ at the height z(t) equals

$$w_e(z) = zW_e/H \qquad \text{(III.3.23)}$$

it follows that

$$\phi(z) = - 2\pi R\ H\ \rho_a\ W_e\ U_f\ (z/H)^2 \ . \qquad \text{(III.3.24)}$$

The next step is to estimate $\bar{\Pi}_v(H)$. This dynamic pressure is obtained from the momentum-integral equation in a control volume outside the cloud. It reads:

$$\frac{d\ M_v}{dt} = - \phi(H) + \pi R^2\ \bar{\Pi}_v(H) \ . \qquad \text{(III.3.25)}$$

Here M_v is the vertical component of the ambient fluid-impulse or virtual momentum. We have used that at a great distance from the cloud the momentum flux $\phi(\infty)$ and the dynamic pressure $\pi(\infty)$ should vanish. M_v is approximated (Batchelor, 1967, 6.6 and 6.8) by:

$$M_v = c_v\ \rho_a\ V\ \bar{w}(H) \qquad \text{(III.3.26)}$$

where

$$c_v = \frac{R}{2H} \ . \qquad \text{(III.3.27)}$$

Using (III.3.19) we find that

$$M_v = \rho_a\ V\ U_f \ . \qquad \text{(III.3.28)}$$

Now we are ready to solve for $\bar{\Pi}_v(z)$. Adding (III.3.25) and (III.3.17) yields

$$\pi R^2\ \bar{\Pi}_v(z) = \frac{d\ M_z}{dt} + \frac{d\ M_v}{dt} + \phi(z) \ . \qquad \text{(III.3.29)}$$

Integrating this equation with respect to z and using (III.3.20), (III.3.24) and (III.3.28), we obtain after fairly long but straightforward calculations that

$$F_v \equiv 2\pi R \int_0^H \bar{\Pi}_v(z) = \qquad \text{(III.3.30)}$$

$$- \left[2\rho_a\ V\ \frac{H}{R} + \frac{4}{3}\ \bar{\rho}\ V\ \left(\frac{H}{R}\right)^2\right] \frac{dU_f}{dt} + 4\ \bar{\rho}\ V\ \left(\frac{H}{R}\right)^2 \frac{U_f^2}{R}$$

$$- \left[2\rho_a\ V\ \frac{H}{R} + \frac{4}{3}\ (\ \bar{\rho} + 2\rho_a)\ V\ \left(\frac{H}{R}\right)^2\right] \frac{W_e U_f}{H} \ .$$

Next we evaluate the pressure forces that act on the cloud edge. The

dynamical force F_d is parameterized as in chapter II. There we found that the vertically integrated dynamic pressure scales as

$$\int_0^{H+} \Pi_d \, dz = \tfrac{1}{2} c_f \rho_a U_f^2 H_f , \qquad \text{(III.3.31)}$$

where c_f is a drag coefficient and H_f a scale depth at the cloud edge representing the fact that the depth of the cloud edge may differ somewhat from the average cloud depth H. Multiplying (III.3.31) with the circumference of the cloud, we obtain the dynamical drag force as:

$$F_d = - c_f \pi R \rho_a U_f^2 H_f . \qquad \text{(III.3.32)}$$

The scale depth H_f can be described in terms of H by using the analysis of chapter II. First we write the ratio H_f/H as:

$$H_f/H = K^2/K_f^2 , \qquad \text{(III.3.33)}$$

where

$$K \equiv U_f / (g \overline{\Delta\rho} H / \rho_a)^{\frac{1}{2}} \qquad \text{(III.3.34)}$$

is a Froude number based on the average cloud depth and

$$K_f \equiv U_f / (g \overline{\Delta\rho} H_f / \rho_a)^{\frac{1}{2}} \qquad \text{(III.3.35)}$$

is the Froude number based on H_f. Thus (III.3.33) is simply an identity. We use this identity to write the dynamical force (III.3.32) as:

$$F_d = - c_d \pi R \rho_a U_f^2 H , \qquad \text{(III.3.36)}$$

where

$$c_d \equiv c_f K^2 / K_h^2 \qquad \text{(III.3.37)}$$

is a new drag coefficient. We now assume that the frontal structure of the present axisymmetric cloud is the same as the frontal structure of the 2-dimensional gravity current which we have discussed in chapter II. Thus we take $c_f = 0.84$ and $K_f = 1.15$ according to (II.3.48) and (II.2.2) respectively. This yields:

$$c_d = 0.64 K^2 . \qquad \text{(III.3.38)}$$

In this equation the Froude number K is a variable, which according to (III.3.34) depends on U_f, $\overline{\Delta\rho}$ and H. These are variables which are computed by our model.

The last force which we have to parameterize is the acceleration reaction force F_a. We model this force as:

$$F_a = d\, M_a / dt \,, \qquad \text{(III.3.39)}$$

where M_a is the radial virtual momentum of the ambient fluid.
Using the arguments given in chapter II we approximate M_a by:

$$M_a \approx 2\pi R\, H^2\, \rho_a\, U_f \,. \qquad \text{(III.3.40)}$$

From the time derivative of this equation, we find in a straightforward manner that

$$F_a = -\,2\,\rho_a\, V\, \frac{H}{R}\left(\frac{dU_f}{dt} - 3\,\frac{U_f^2}{R} + \frac{W_e U_f}{H}\right) . \qquad \text{(III.3.41)}$$

With this result we have finished our analysis of the pressure forces and we are ready for our final momentum equation.

We will write this in the form of an equation for the acceleration dU_f/dt of the cloud edge. Using (III.3.5), (III.3.10), (III.3.13), (III.3.30), (III.3.36) and (III.3.41), combining terms with dU_f/dt, U_f^2/R and $W_e U_f/H$ respectively and dividing by V yields:

$$\frac{dU_f}{dt} = \frac{g\overline{\Delta\rho}\frac{H}{R} - \left[c_d - 6\frac{H}{R} - 4\frac{\bar{\rho}}{\rho_a}\left(\frac{H}{R}\right)^2\right]\frac{\rho_a U_f^2}{R} - \left[\frac{2}{3} + 6\frac{H}{R} + \frac{4}{3}\left(\frac{\bar{\rho}}{\rho_a}+2\right)\left(\frac{H}{R}\right)^2\right]\frac{\rho_a W_e U_f}{H}}{\frac{2}{3}\bar{\rho} + 4\,\rho_a\,\frac{H}{R} + \frac{4}{3}\,\bar{\rho}\,\left(\frac{H}{R}\right)^2} \,. \qquad \text{(III.3.42)}$$

In the numerator of this equation we may recognize the following terms:

$g\,\overline{\Delta\rho}\,H/R$ representing the static pressure force

$c_d\,\rho_a\,U_f^2/R$ representing the drag force on the cloud edge, and

$\frac{2}{3}\,\rho_a\,e\,U_f/H$ representing the radial stress related to entrainment.

The other terms containing H/R and $(H/R)^2$ represent the effect of cloud deformation on dU_f/dt.

The denominator gives the inertial terms of the radial momentum in the cloud, of the ambient fluid momentum and of the vertical momentum inside the cloud respectively. This last term is the major inertial term when $\overline{\rho}/\rho_a$ is large and H/R = 2, as in most of the experiments by Havens and Spicer (1985). Therefore "shallow-layer" models are not likely to behave well in the early acceleration phase.

We now continue with an analysis of the energy budget of the cloud.

III.4 The energy budget

III.4.1 General energy budget

In the following we will derive an equation for the time rate of change dT_E/dt of the turbulent kinetic energy. Our starting point is the conservation of total energy in a large control volume containing the cloud and the secondary flows around it. In the present problem we distinguish between four types of energy: the potential energy P_E, the kinetic energy of mean radial and vertical motions K_E, the earlier mentioned turbulent kinetic energy T_E and the internal heat I_E. The conservation law reads

$$\frac{d}{dt}\,(P_E + K_E + T_E + I_E) = 0\ . \qquad \text{(III.4.1)}$$

Between the various forms of energy four transformation processes take place, namely:

- the production G of mean kinetic energy, at the cost of potential energy,
- the buoyant destruction B of turbulent energy, which is the conversion of turbulent energy into potential energy by entrainment,
- the shear production S of turbulent energy and
- the dissipation D of turbulent energy into internal heat.

This energy system is summarized in figure III.1.

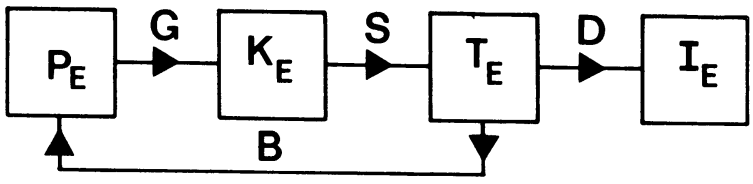

figure III.1: The energy budget:

The equations for this system are:

$$dP_E/dt = -G + B \ , \qquad \text{(III.4.2)}$$

$$dK_E/dt = G - S \ , \qquad \text{(III.4.3)}$$

$$dT_E/dt = S - B - D \ , \qquad \text{(III.4.4)}$$

and

$$dI_E/dt = D \ . \qquad \text{(III.4.5)}$$

Since we want to solve for dT_E/dt, we have to model S, B and D. We do so as follows. In section 4.2 we parameterize P_E and K_E in terms of the model variables V, R, H, U_f, W_e, $\overline{\Delta\rho}$ and $\overline{\rho}$. Using (III.4.2) and (III.4.3) we derive parameterizations for S and B. In section III.4.3 the dissipation D is modelled directly, using the turbulent variables $\overline{u}_t$ and Ri_t. In section III.4.4 we combine these results to obtain an equation for dT_E/dt.

III.4.2 The shear production S and buoyant destruction B

As mentioned above S and B will be modelled by using the equations for dP_E/dt and dK_E/dt. The potential energy has been found before (III.2.13) as:

$$P_E \equiv \tfrac{1}{2} g \Delta\rho_o V_o H \qquad \text{(III.4.6)}$$

Taking the time derivative of this equation we find that

$$dP_E/dt = \tfrac{1}{2} g \Delta\rho_o V_o (dH/dt) \ . \qquad \text{(III.4.7)}$$

Because $H = V/\pi R^2$, it follows that $dH/dt = -2HU_f/R + W_e$ and that

$$dP_E/dt = -G + B = - g \Delta\rho_o V_o U_f H/R + \tfrac{1}{2} g \Delta\rho_o V_o W_e \ . \qquad \text{(III.4.8)}$$

In this equation the first term on the right hand side equals exactly -G, while the second term equals B. Using the entrainment relation (III.2.3) we thus can write

$$B = \tfrac{1}{2} c_e g\Delta\rho_o V_o \overline{u}_t / (c_t + Ri_t) \ . \qquad \text{(III.4.9)}$$

The mean kinetic energy is parameterized as

$$K_E = \tfrac{1}{2} V U_f^2 \left[\frac{2}{3}\bar{\rho} + 4\rho_a \frac{H}{R} + \frac{4}{3}\bar{\rho}\left(\frac{H}{R}\right)^2\right] . \qquad \text{(III.4.10)}$$

This parameterization is consistent with that of the momentum equation (III.3.42). The first term represents the interior radial component, the second the virtual energy outside the cloud and the third the energy of the vertical motion in the cloud. Taking the time derivative of all the terms and eliminating terms containing dU_f/dt by using the momentum equation (III.3.42), we find after long and tedious, but straightforward calculations that

$$dK_E/dt = G - S =$$

$$g\,\Delta\rho_o\, V_o\, U_f\, H/R - c_d\,\rho_a\, V \frac{U_f^3}{R} - \left[\frac{1}{3} + 2\frac{H}{R} + 2\left(\frac{H}{R}\right)^2\right]\rho_a\, V \frac{W_e U_f^2}{H} . \qquad \text{(III.4.11)}$$

Here we recognize in the first term on the right hand side the production G of mean kinetic energy. The other terms give the shear production of T_E. The meaning of the various terms in the shear production is the following:

$c_d\,\rho_a\, V\, U_f^3/R$ is the production at the cloud edge.

$\frac{1}{3}\rho_a\, V\, W_e\, U_f^2/H$ is the production by the interaction of the radial turbulent stress that scales as $W_e U_f$ and the velocity shear that scales as U_f/H.

The other terms represent the shear production related to secondary flows.

III.4.3 The dissipation D

The dissipation is parameterized in a standard manner as (Tennekes and Lumley, 1973, p.20):

$$D \propto \bar{\rho}\, V\, \bar{u}_t^3 / \ell , \qquad \text{(III.4.12)}$$

where ℓ is a characteristic length scale. We follow Brost and Wyngaard (1978) and write for the inverse of this length scale:

$$1/\ell = 1/\ell_g + 1/\ell_b . \qquad \text{(III.4.13)}$$

In this equation ℓ_g represents the limit to the size of large eddies due to the presence of the ground. In the present problem turbulent eddies are predominantly created at a height of O(H), so we may take

$$\ell_g = H \ . \qquad \text{(III.4.14)}$$

The length scale ℓ_b is the so-called buoyancy length scale. This length scale represents the reduction of the eddy size and the enhancement of dissipation in a stably stratified flow. ℓ_b can be estimated by assuming a balance between vertical inertial forces that scale as $\rho\sigma_w^2 / \ell_b$ (σ_w^2 is the vertical velocity variance) and buoyant forces that scale as $- g \ell_b (\partial\rho/\partial z)$. This balance gives

$$\frac{1}{\ell_b} = \frac{- g \ell_b (\partial\rho/\partial z)}{\rho\sigma_w^2} \ . \qquad \text{(III.4.15)}$$

We multiply the numerator and the denominator of the right hand side of this equation by σ_w and obtain:

$$\frac{1}{\ell_b} = \frac{- g \sigma_w \ell_b (\partial\rho/\partial z)}{\rho\sigma_w^3} \ . \qquad \text{(III.4.16)}$$

In this equation $\sigma_w \ell_b$ can be interpreted as a vertical eddy diffusivity and $- g \sigma_w \ell_b (\partial\rho/\partial z)$ as a local buoyancy flux. The average value of this flux clearly is

$$\overline{- g \sigma_w \ell_b (\partial\rho/\partial z)} = B/V \ , \qquad \text{(III.4.17)}$$

where B is the total buoyant destruction given by (III.4.9). Next we take the average value of $\rho\sigma_w^3$ proportional to $\bar{\rho}\,\bar{u}_t^3$ and obtain from (III.4.12)-(III.4.17) our parameterization of the dissipation as:

$$D = c_n \frac{\bar{\rho} V \bar{u}_t^3}{H} + c_b B \ , \qquad \text{(III.4.18)}$$

where c_n and c_b are empirical coefficients. In this equation the first term at the right hand side gives the dissipation that we would have in the absence of stable stratification. The coeffient c_n can be estimated as follows. In a neutral shear flow characterized by a stress $\bar{\rho}\,u_*^2$ the dissipation at a height H above the ground equals $\bar{\rho}\,u_*^3 / \kappa H$, where $\kappa = 0.4$ is the von Kármán constant.

Since approximately in such a flow $u_*^3 \approx 0.04\ \bar{u}_t^3$ (Beljaars et al., 1983), we find as a first guess:

$$c_n \approx 0.1 \ . \qquad \text{(III.4.19)}$$

The last term in the dissipation equation (III.4.18) represents the enhancement of the dissipation by the presence of stable stratification. The coefficient c_b can be estimated by looking at stable free shear layers (e.g. Nieuwstadt, 1984). For a steady stable layer dT_E/dt vanishes and the turbulent energy budget reads:

$$B + D = S \ . \qquad \text{(III.4.20)}$$

The relative magnitude of the three terms in this equation can be expressed by means of a flux Richardson number Ri_f which in the present context is defined as:

$$Ri_f \equiv B/S \ . \qquad \text{(III.4.21)}$$

When the stable layer approaches neutral stability, Ri_f vanishes, while in very stable conditions Ri_f approaches a constant critical value $Ri_c \approx 0.2 - 0.25$. Thus in very stable conditions

$$B/S \approx Ri_c \qquad \text{(III.4.22)}$$

and because of (III.4.20)

$$D \approx \left(\frac{1}{Ri_c} - 1\right) B \ . \qquad \text{(III.4.23)}$$

So in very stable steady flow the dissipation is proportional to the buoyant destruction.

In the present problem the flow is quite unsteady. Then we may run into problems, because B only depends on the actual state of the turbulence, while the shear production S also depends on the state of the mean flow. Since the development of the mean flow and that of the turbulence are not normally in phase, the closure assumption (III.4.22) is not likely to be valid in the present context.

On the other hand, like B, the dissipation D depends only on the actual state of the turbulence. So (III.4.23) does seem to be a suitable closure assumption for very stable unsteady flow. In the present problem the stablity is represented by the turbulent bulk Richardson number Ri_t as defined by (III.2.4). Thus we expect that

$$D \to (\frac{1}{Ri_c} - 1)\, B \quad \text{for } Ri_t \to \infty \,. \tag{III.4.24}$$

Using tis relation, (III.4.9) and (III.4.18) we can solve for c_b. The result is

$$c_b = \frac{1}{Ri_c} - 1 - 2\,\frac{c_n}{c_e} \,. \tag{III.4.25}$$

Taking $Ri_c = 0.25$, $c_n = 0.1$ and $c_e = 0.2$ we find that

$$c_b = 2.0 \,, \tag{III.4.26}$$

which is the value that we will use in our model study. We are now ready to complete our model description.

III.4.4 Final equation for dT_E/dt

Using the results of the previous sections in (III.4.4) we arrive at the following turbulent energy equation:

$$\frac{dT_E}{dt} = c_d\, \rho_a\, V\, \frac{U_f^3}{R} + [\frac{1}{3} + 2\,\frac{H}{R} + 2\,(\frac{H}{R})^2]\, \rho_a\, V\, \frac{W_e U_f^2}{H}$$

$$- c_n\, \bar{\rho}\, V\, \bar{u}_t^3/H - \tfrac{1}{2}\,(c_b+1)\, c_e\, g\, \Delta\rho_o\, V_o\, \bar{u}_t \,/\, (c_t + Ri_t) \,. \tag{III.4.27}$$

In this equation W_e and $\bar{u}_t$ are still functions of T_E itself, as defined by (III.2.3) and (III.2.6). Thus numerical integration with respect to time is needed to solve it. This result completes our model description.

III.5 Analysis and simulation of still-air experiments

III.5.1 Experimental characteristics

In this section we analyse laboratory experiments by Havens and Spicer (1985) and Thorney Island trials with low atmospheric turbulence. The characteristics of the experiments used from Havens and Spicer are given in table III.1. As we see, the initial volumes vary by a factor of 10, while the measuring heights used vary by a factor 14. So possible effects of scale and measuring height can be investigated.

Table III.1

Experiments by Havens and Spicer (1985)

$\Delta\rho_o/\rho_a = 3.19$, $H_o/R_o = 2$

Symbol used in figures	•	Δ	<>	o	+	x
$V_o[m^3]$	0.531	0.135	0.535	0.054	0.054	0.054
z_m/H_o	0.007	0.011	0.015	0.015	0.049	0.098

From Thorney Island we select the trials 12 and 34, because these were trials with a low atmospheric turbulence as expressed by its density

$$t_E \equiv \tfrac{1}{2}\,\rho_a\,(\sigma_u^2 + \sigma_v^2 + \sigma_w^2) \qquad \text{(III.5.1)}$$

where σ_u^2, σ_v^2 and σ_w^2 are the variances of the three wind components. We approximate this turbulent kinetic energy density by

$$t_E = \tfrac{1}{2}\,\rho_a\,(c_*\,u_*)^2 \,, \qquad \text{(III.5.2)}$$

where u_* is the surface friction velocity and

$$c_* \simeq 3 \qquad \text{(III.5.3)}$$

Table III.2 Thorney Island Trials

Trial no.	12	34
Symbol used in figures	C	S
$\Delta\rho_o/\rho_a$	1.37	0.83
H_o/R_o	1.81	1.95
$V_o[m^3]$	1950	2100
z_m/H_o	0.032	0.029
$U\ [m\ s^{-1}]$	2.6	1.4
$u_*\ [m\ s^{-1}]$	0.080	0.028

an empirical coefficient (Beljaars et al., 1983; Puttock, 1987). The friction velocity u_* can be estimated from the windspeed U_{10} at 10 m, the surface roughness length z_o and the cloud cover using a procedure by Van Ulden and Holtslag (1985). For our calculation we used zero cloud cover, z_o = 0.01 m and the observed windspeeds. The resulting u_* is given in table 2. This result will be used later to estimate the period in which atmospheric turbulence presumably has a negligible effect on cloud mixing. The other experimental characteristics of the trials 12 and 34 are also given in table III.2.

III.5.2 Analysis and simulation of radial spreading

Havens and Spicer (1985) provide accurate measurements of the cloud radius as a function of time. For the Thorney island trials 12 and 34, no such data are available. Thus in this section we only analyse the laboratory data. To investigate possible scale effects we non-dimensionalize the data with the initial radius R_o and the velocity scale

$$U_o \equiv \sqrt{g\ \Delta\rho_o\ H_o/\rho_a}\ , \qquad \text{(III.5.4)}$$

where H_o is the initial cloud height.
The time is scaled with

$$t_o = R_o/U_o\ . \qquad \text{(III.5.5)}$$

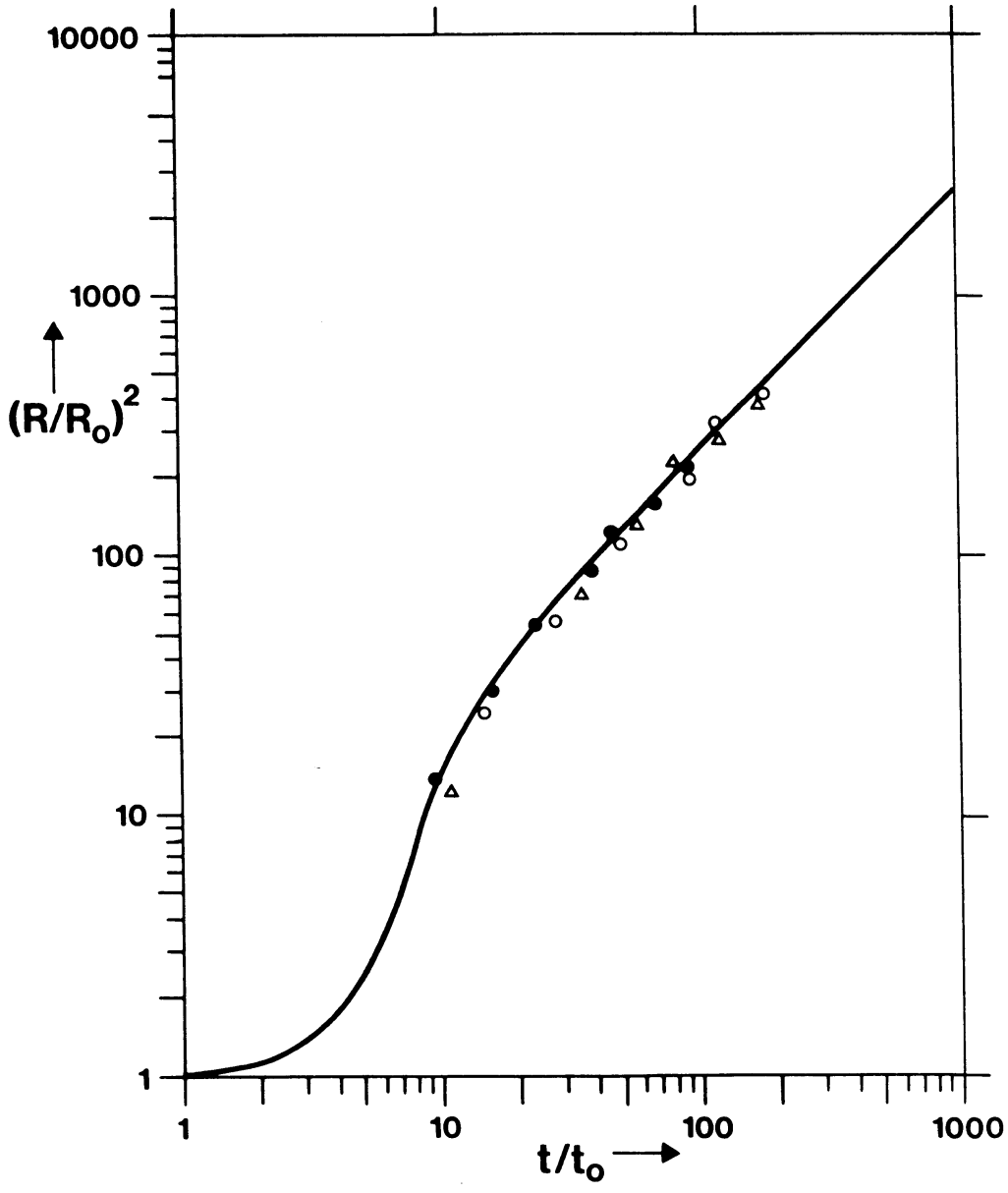

figure III.2: Dimensionless cloud area versus dimensionless time.
Symbols : data from Havens and Spicer (1985) (see table 1)
Solid line: present model
R_o initial cloud radius, $t_o = R_o/U_o$; $U_o = \sqrt{g\ \Delta\rho_o\ H_o/\rho_a}$; $\Delta\rho_o$ initial density difference, H_o initial cloud height, ρ_a air density.

In figure II.2 we give the experimental data on dimensionless cloud area, together with our model simulation. As we see there appears to be no scale effect in the data and viscous effects do not seem to be present for the time interval shown. The performance of the model is quite satisfactory. The time delay connected with the initial acceleration is well modeled. The straight part of the curve corresponds with

$$K = U_f / (g \overline{\Delta\rho} H/\rho_a)^{\frac{1}{2}} = 1.20 \ . \qquad \text{(III.5.6)}$$

This result agrees very well with the average value K = 1.19 that was observed for the low-windspeed trials 8, 9 and 10 at Thorney Island (Brighton et al., 1985). Thus large scale field data seem to be consistent with the laboratory data and with the present model for gravity spreading in still air.

III.5.3 Analysis and simulation of the mixing process

In this section we will analyse and simulate area-averaged concentrations. For the Thorney Island trials pertinent data are available (Brighton, 1985; Brighton and Prince, 1986). For the laboratory experiments we have computed area averages from the graphs given in the report (Havens and Spicer, 1985). The contribution to the average of each sensor was weighted according to the area for which the sensor is representative.

The representative area scales with $2\pi\ R_m\ \Delta R$, where R_m is the distance of the sensor from the origin and ΔR the spacing between the sensors. Thus the present analysis puts more weight on the outer sensors. For greater times this leads to area-averaged concentrations that are only slightly lower than the values given by Van Ulden (1986). We further require that at least three sensors saw gas and that the cloud did not move too far beyond the outermost sensor. This reduces the r.m.s. error of the computed area-averages to about 10-20% and limits the period of reliable data to the dimensionless time interval $30 < t/t_o < 180$. This time interval will be included in the analysis.

The Thorney Island data - which cover a much longer period - can only be used in the present analysis, as long as mixing by atmospheric turbulence can be neglected. We assume that this is the case when the atmospheric turbulent energy density is less than half the turbulent energy density produced by the cloud as computed with our model. This is the case in trial 12 for $t/t_o < 70$ and in trial 34 for $t/t_o < 170$. Thus we include in our analysis only data from the Thorney Island trials for dimensionless times smaller than these limits.

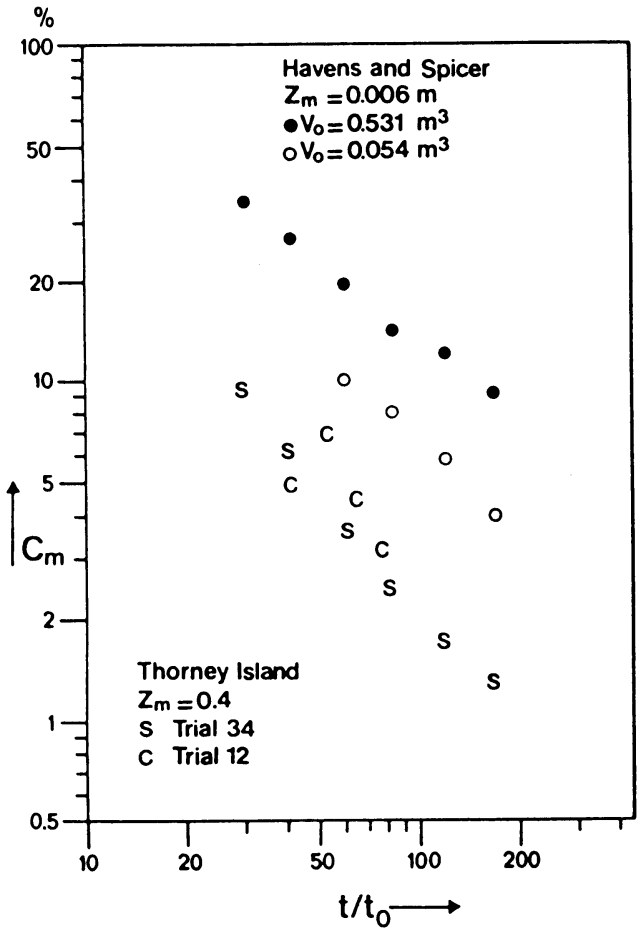

figure III.3: Observed area-averaged concentration C_m versus dimensionless time. Symbols: see table 1 and table 2.

After this careful data selection, we now proceed with a comparison between the various experiments. A representative selection is shown in figure III.3. Included are data from Havens and Spicer (1985) for V_o = 0.531 m^3 and V_o = 0.054 m^3. Further we give the data for the Thorney Island trials 12 and 34. In the figure we see very significant differences between the experiments. The question is: what causes the differences? At first sight one might think that apparently different mixing processes are involved. There is, however, an alternative and quite exciting interpretation. It may be that the measurements depend strongly on the dimensionless measuring height z_m/H_o. Let us investigate this possibility.

In figure III.4 we have plotted measured area-averaged concentrations as a function of this dimensionless measuring height for t/t_o = 60. Apart from 4 data points taken from figure III.3, we have also plotted data from other laboratory experiments including estimates of the area-averaged concentration

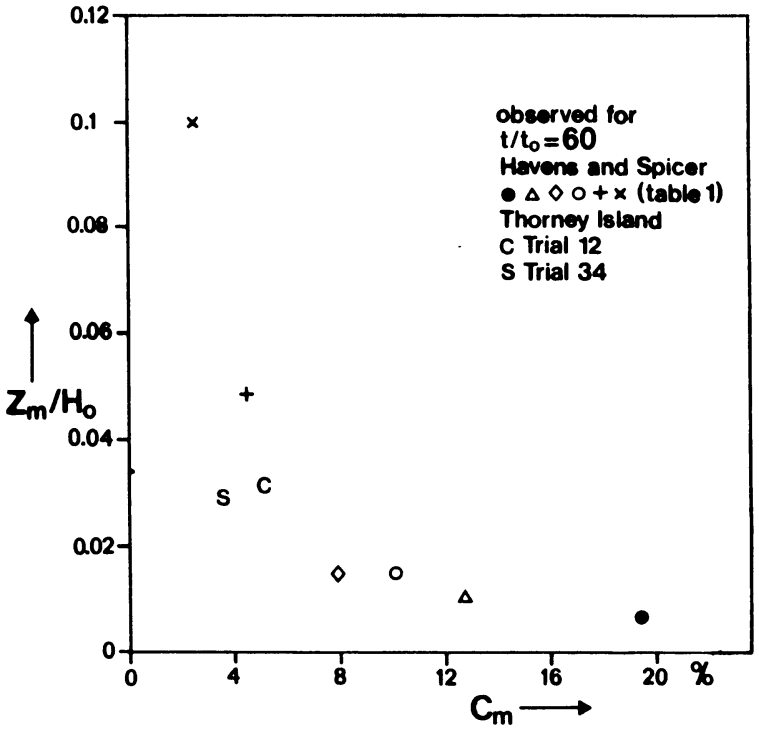

figure III.4: Observed area-averaged concentration C_m for $t/t_o = 60$ versus dimensionless measuring height z_m/H_o.
z_m: observation height; H_o: initial cloud height.

obtained from sensors put at 0.02 m and 0.04 m. This figure strongly suggests that the observed concentrations decrease rapidly with height. The Thorney Island data are fairly consistent with the trend observed for the laboratory data. Similar figures can be made for different times and a similar behaviour is observed. A more complete picture of the concentration profile can be obtained by plotting the data for the different times in a scaled form. This is done in figure III.5. Measured concentrations C_m have been normalized with cloud averaged concentrations $\overline{C}_c$ as calculated with our model. Similarly the measuring height z_m is normalized with the calculated cloud height H_c. The result is that all data appear to show a similar decrease with height. In fact we have plotted the concentration profile in the similarity co-ordinates suggested by eqn. (III.2.15). The data suggest that such a similarity function exists, at least for the analysed time interval.

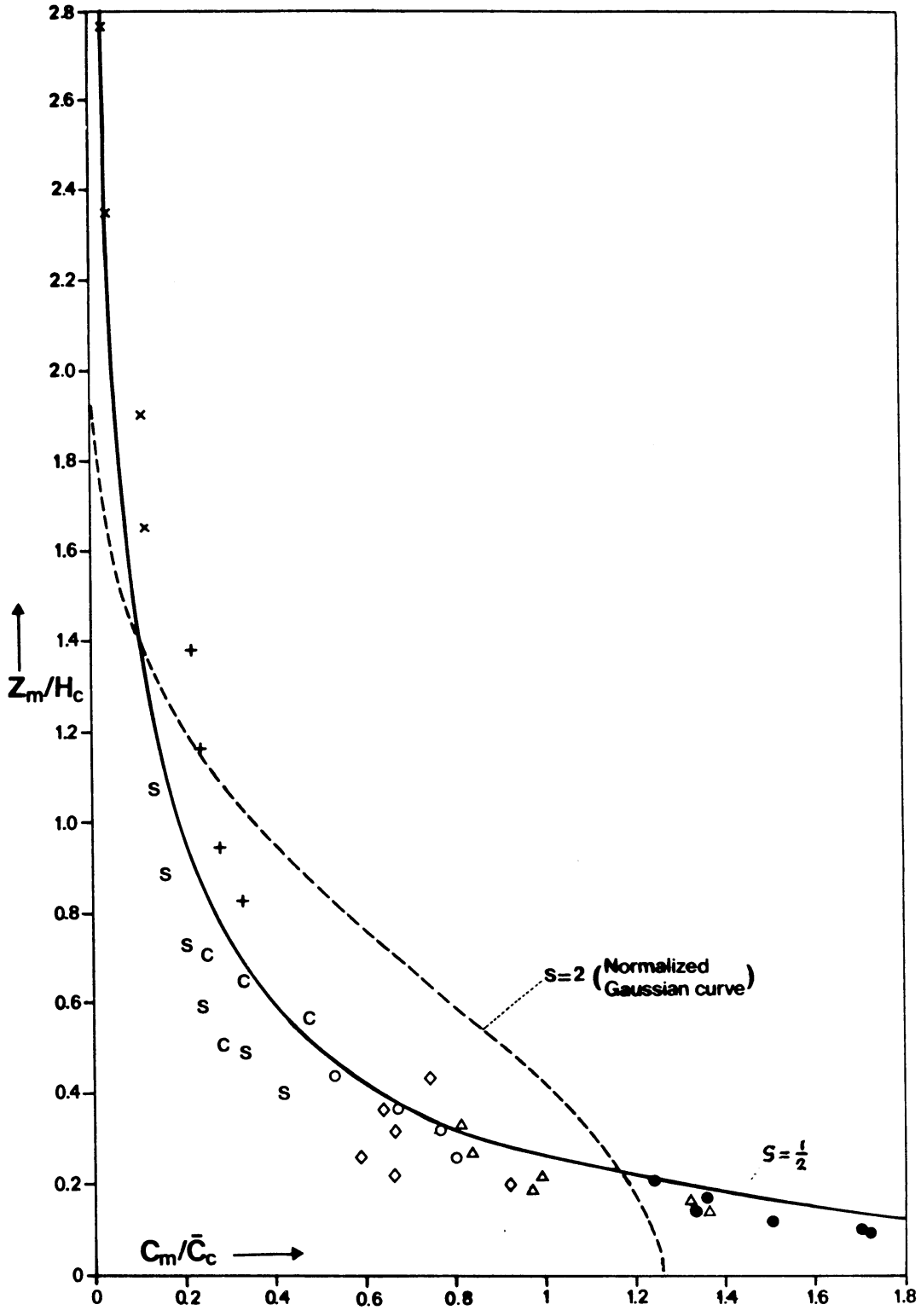

figure III.5: Normalized observed area-averaged concentration $C_m/\bar{C}_c$ versus normalized observation height z_m/H_c. $\bar{C}_c$ is the computed cloud-averaged concentration and H_c the computed cloud-height for the values of t/t_o shown in figure III.3. The symbols are explained in table III.1 and table III.2. The curves in the figure are:
broken line: $\frac{4}{\pi} \exp\left[-\frac{4}{\pi}\left(\frac{z}{H}\right)^2\right]$ (gaussian curve)
solid line : $6 \exp\left[-\left(\frac{12z}{H}\right)^{1/2}\right]$

For reference purposes we show in the figure the Gaussian profile. It is clear that the concentration profile is not Gaussian. Thus the fair agreement which Van Ulden (1987A) found, between concentrations computed with a Gaussian profile and the data for the experiments with $V_o = 0.531$ m^3 is fortuitous. In the figure another curve is shown which more or less goes through the data. This curve is the similarity profile (III.2.18) with a shape factor $s = \frac{1}{2}$. It reads

$$C(z)/\overline{C} = 6 \exp\left[-(12\ z/H)^{\frac{1}{2}}\right] . \qquad \text{(III.5.7)}$$

With showing this curve, we do not imply that it gives a correct description of the concentration profile below $z/H = 0.1$. In this respect the data are not conclusive. The results of the above analysis may be biased by the use of our model for calculating H_c and $\overline{C}_c$. We think,however, that this bias is weak at most. The reason is, that the data in figure III.5 show a hyperbolic behaviour in the sense that $z_m\ C_m/H_c\ \overline{C}_c \approx 0.2$ is approximately constant for the bulk of the data. Since $H_c\ \overline{C}_c = V_o/\pi R_c^2$ and since our model predicts the cloud area quite accurately, errors in the entrainment model lead to compensating errors in H_c and $\overline{C}_c$. Therefore errors in the entrainment model only give rise to a shift of the data along the fitted curve and have a minor effect on the analysis. In this context it should be noted that the curvature of the vertical concentration profile found here is also present in the profile analysis by Brighton (1985). This follows from the fact that the latter author found negative values of h_p for most of the time (see his section 2.4).

Let us take now (III.5.7) as a preliminary estimate of the dimensionless concentration profile and use it in our model to predict the concentrations at the observation heights of the data given in figure III.3. The result is shown in figure III.6. In this figure the model results for trial 12 and 34 approximately coincide and are given by one curve. For the two laboratory experiments both model curves are given. We see that the agreement between the model and the data is satisfactory. Thus making corrections for the observation height removes the discrepancy between the Thorney Island data and the laboratory data and also explains the differences between the two laboratory data sets for different initial volume. The present analysis indicates that no significant viscous effects are present in the laboratory data as suggested earlier by Van Ulden (1987A).

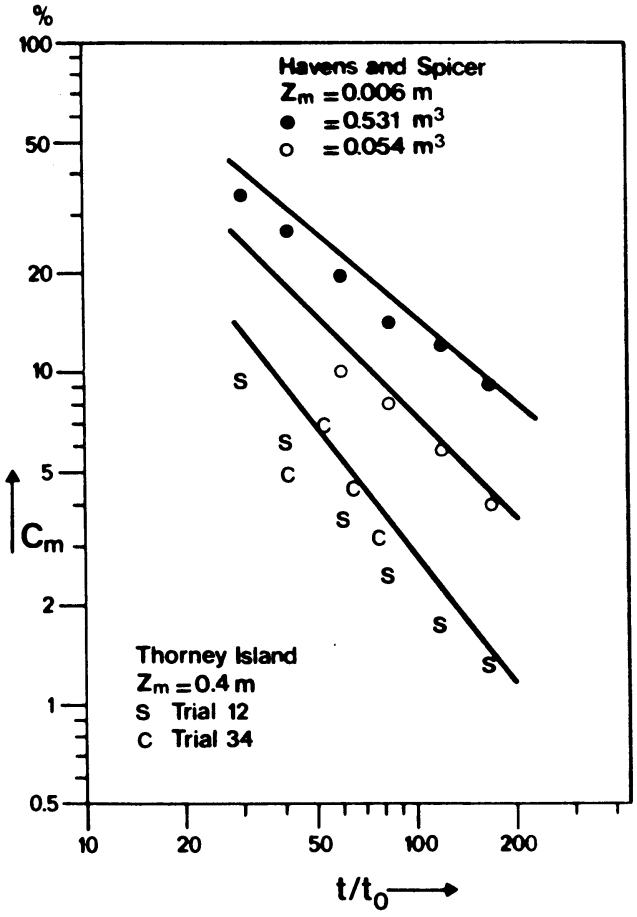

figure III.6: Observed and predicted area-averaged concentration C_m versus dimensionless time t/t_o. Data as in figure 3.
Solid line: present model.

An important preliminary conclusion is that, at least in the low wind speed trials at Thorney Island, the observations at 0.4 m are not representative for the volume averaged concentrations and may be very much less than the non-observed surface concentrations. If our interpretation is correct, the Thorney Island data need a careful reanalysis. For example the cloud heights as derived by Brighton (1985) may be significantly too high. The same is true for empirical coefficients for side entrainment. Further discussion on this subject is given in section III.6.

So far we have considered area-averaged concentrations. It is also interesting to look at concentrations that are measured locally by a specific sensor. In the figures III.7 and III.8 we give two typical examples taken from the data by Havens and Spicer (1985). The data are from the sensors placed at R_m = 2.4 m and R_m = 6.4 m from the cloud centre at a height of H_m = 0.006 m.

Also our model results are given. It is seen that the arrival time is well predicted. The modelled concentrations rise instantaneously to the computed area-averaged concentration at sensor height for the computed time. The measured concentrations rise more slowly. The decrease of the concentration with time is well modelled. A good impression is obtained of the systematic mixing process and the natural concentration fluctuations around it. In general it can be said that the performance of the model in predicting local concentrations near the surface is satisfactory.

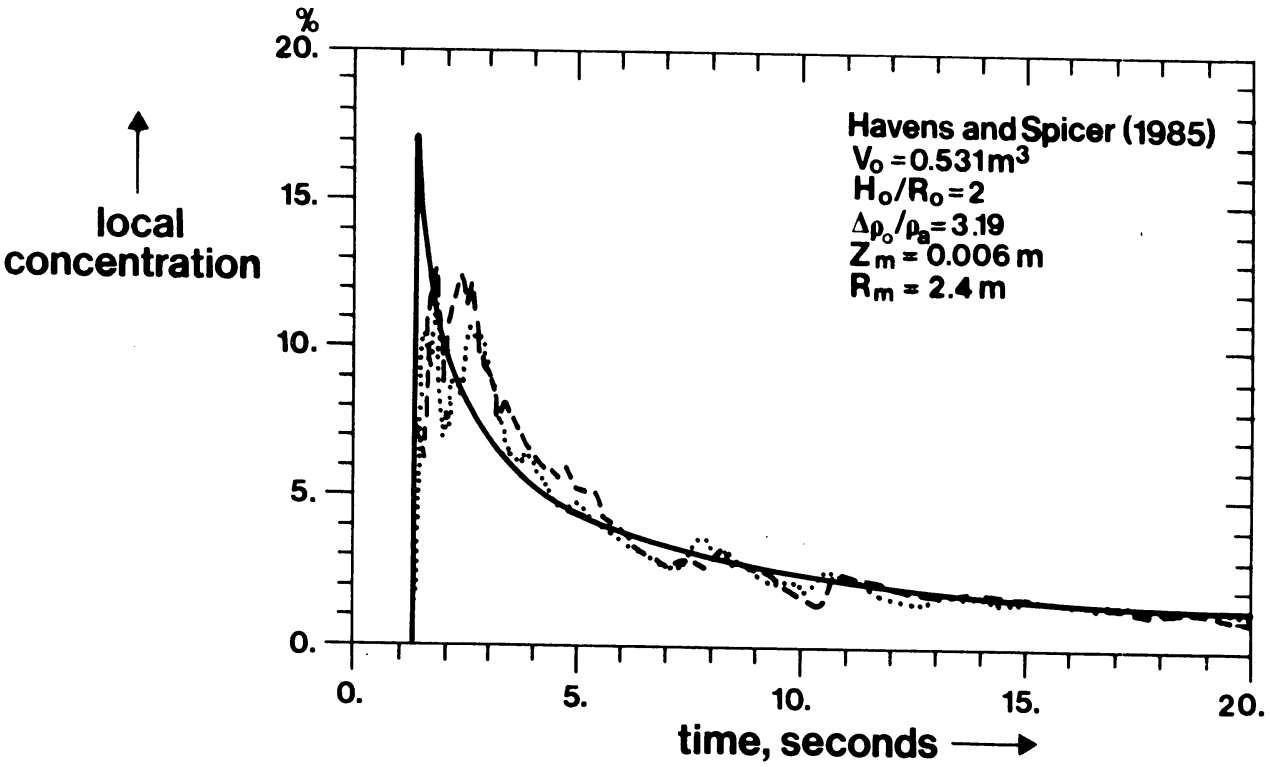

figure III.7: Local concentration versus time. Broken and dotted line: observed by Havens and Spicer (1985) at 2.4 m from the cloud center. Solid line: present model.

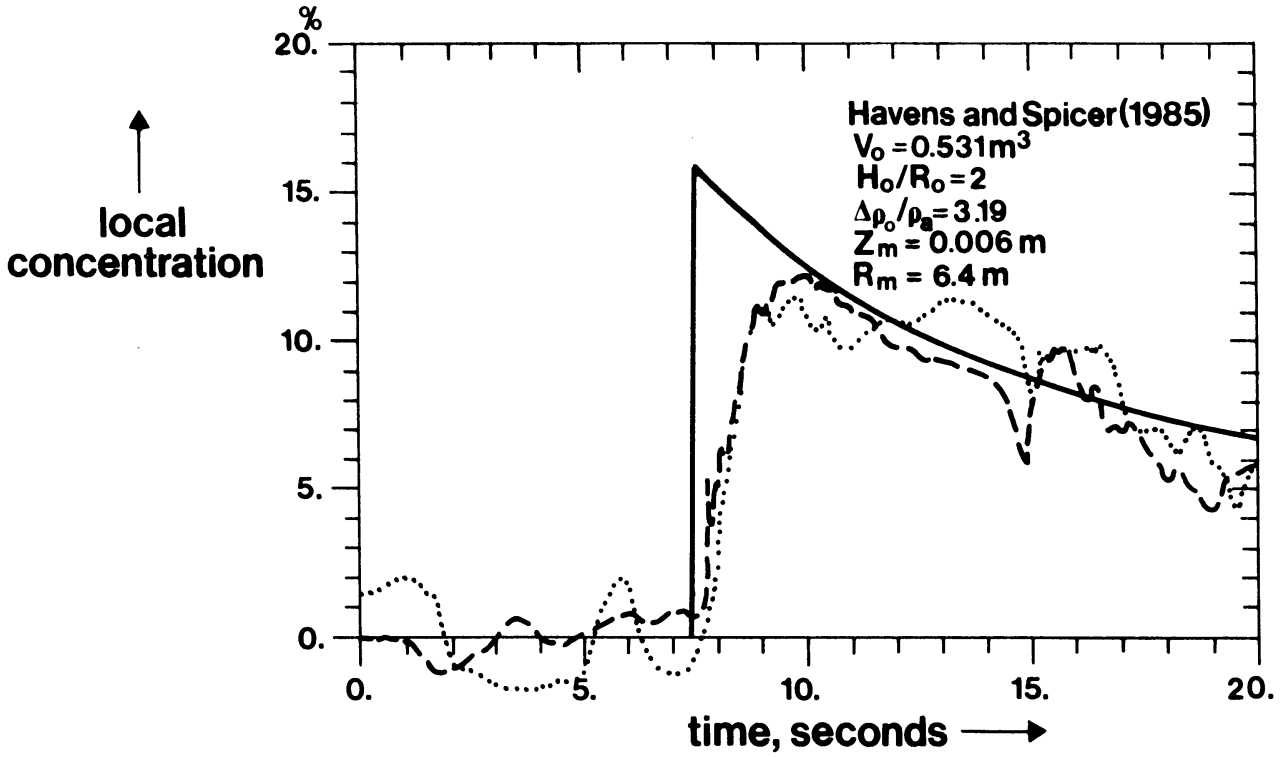

figure III.8: Local concentration versus time. Broken and dotted line: observed by Havens and Spicer (1985) at 6.4 m from the cloud center. Solid line: present model.

III.6 Model characteristics and sensitivity analysis

Now that we have seen that the present model has something to do with physical reality, it is worthwhile to give further illustrations on the general features of the spreading and mixing process of a dense puff. Also we will investigate the influence on model results of variations in empirical coefficients and in initial conditions.

III.6.1 Model properties for $\Delta\rho_o/\rho_a = 3.19$ and $H_o/R_o = 2$

The model properties can be illustrated with the behaviour of the scaled front velocity or Froude number

$$k \equiv U_f \; / \; (g \, \overline{\Delta\rho} \, H \; / \; \rho_a)^{\frac{1}{2}} \qquad \text{(III.6.1)}$$

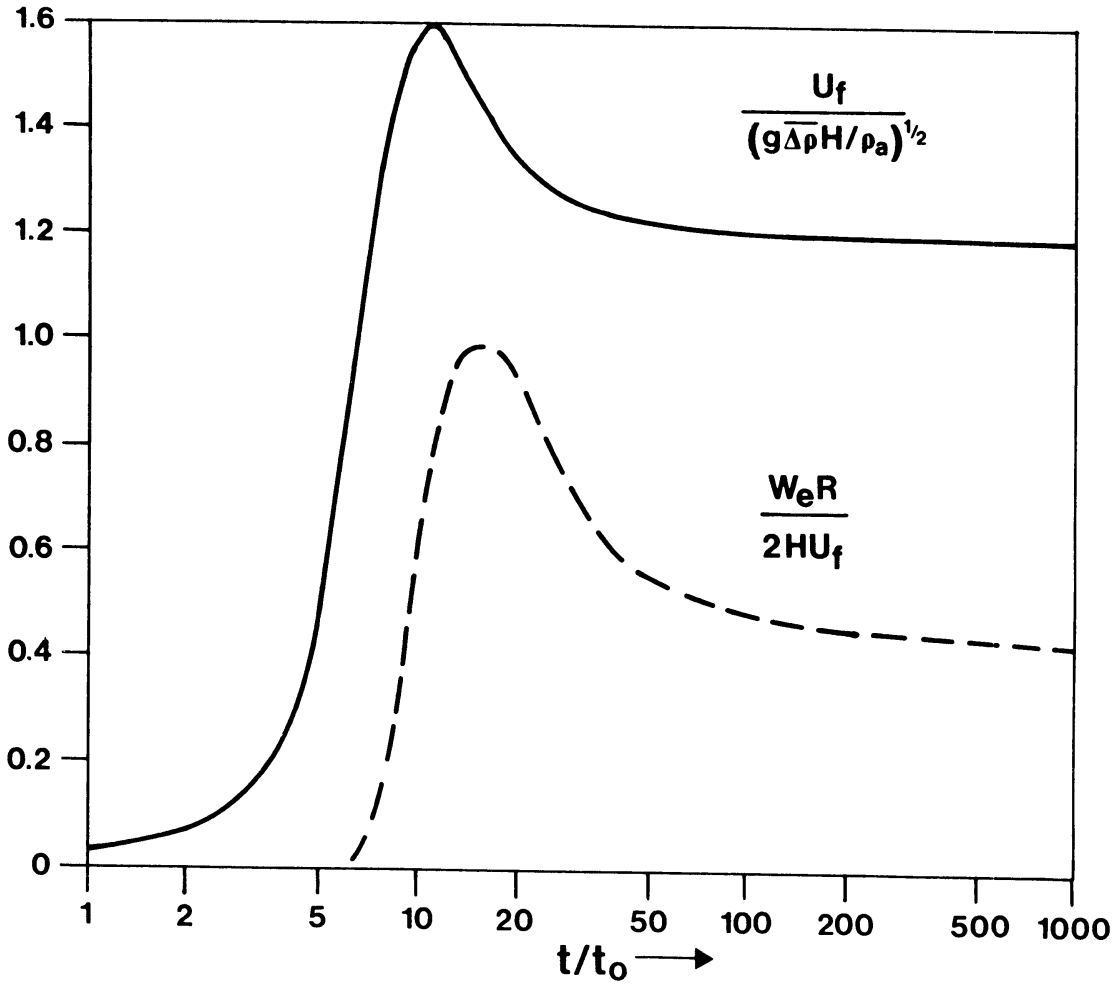

figure III.9: Modelled Froude number and Scaled Entrainment rate.
Solid line : Froude number $k \equiv U_f / \sqrt{g \overline{\Delta\rho} H / \rho_a}$.
Broken line: Scaled Entrainment rate $\alpha_e \equiv We^{R/2HU_f}$
$\Delta\rho_o/\rho_a = 3.19$; $H_o/R_o = 2$.

and of the scaled entrainment rate

$$\alpha_e = W_e R / 2 H U_f , \qquad \text{(III.6.2)}$$

where, mathematically speaking, α_e is identical with the traditional coefficient for edge-entrainment (Van Ulden, 1974). These dimensionless quantities are plotted against the dimensionless time t/t_o in figure III.9. We see that the Froude number is not constant. First we see the acceleration from rest until the Froude number reaches a maximum value of about 1.6 for $t/t_o \approx 11$. Then the Froude number decreases until it reaches an approximately constant value of $k = 1.20$ for $t/t_o > 100$. The entrainment coefficient shows a similar behaviour, be it with a time lag $\Delta t/t_o \approx 4$. This time lag is due to the fact

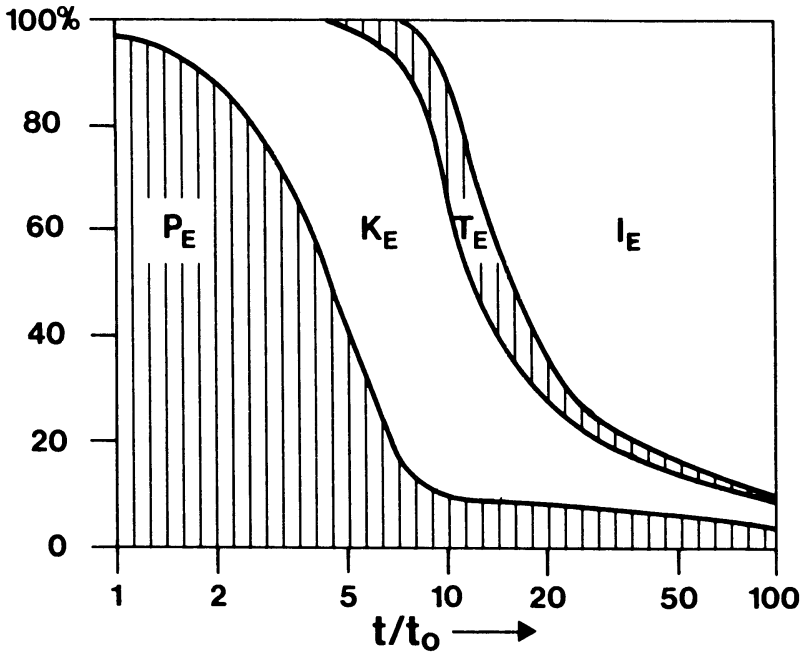

figure III.10: Modelled time variation of the four components of the energy budget.
Vertical axis: percentage of total energy.
$\Delta\rho_o/\rho_a = 3.19$; $H_o/R_o = 2$.

that it takes time to create turbulent energy needed for entrainment. The entrainment reaches a maximum of $\alpha_e = 1$ for $t/t_o \approx 15$. Around this time the cloud height hardly decreases, because the upward velocity of the cloud top due to entrainment is about equal to the slumping motion. For $t/t_o > 100$ the entrainment coefficient varies only slowly, but an asymptotic value is not yet reached for $t/t_o = 1000$.

The spreading and mixing process can be further illustrated by looking at the energy budget of the cloud. This is shown in figure III.10. Plotted are the potential energy, the kinetic energy, the turbulent energy and the internal heat. These four terms of the energy budget are scaled in such a way that their sum equals 100%. At the release of the cloud all energy is potential energy. In the slumping process potential energy is transformed into kinetic energy. This kinetic energy leads to the shear production of turbulent energy, which in turn is dissipated into heat and is used partly to increase the potential energy by entrainment. For $t/t_o \approx 8$ the kinetic energy reaches a maximum of about 75% of the total energy. Then the potential energy has been decreased by almost a factor 10. The turbulent energy reaches its maximum of about 22% for $t/t_o = 10$. For $t/t_o = 100$ already 90% of the original energy has been dissipated into

heat. In the figure we see clearly the increasing time lag for the production of kinetic energy, for the production of turbulent energy and for dissipation.

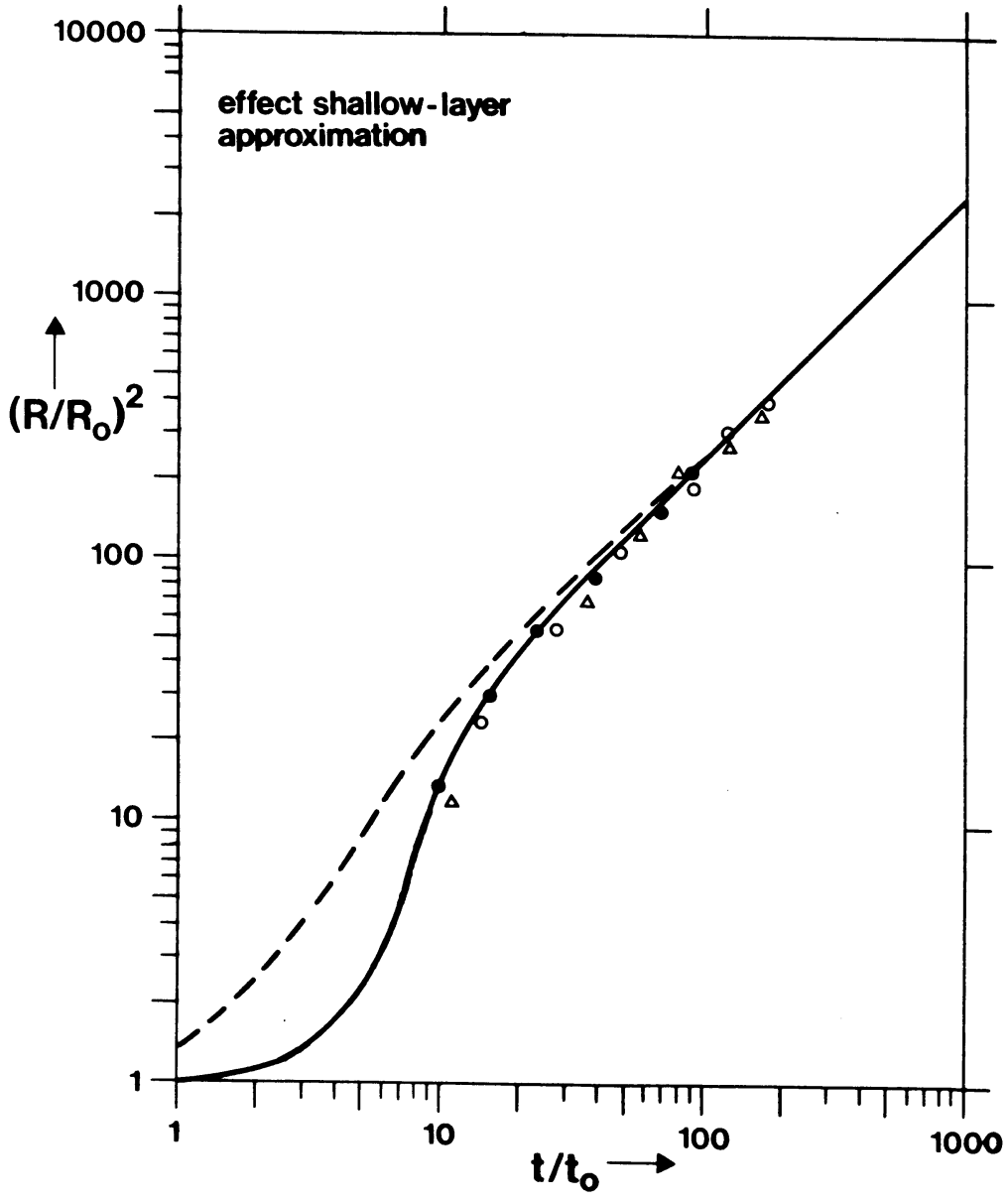

figure III.11: Dimensionless cloud area versus dimensionless time.
Solid line : standard model.
Broken line: model with shallow layer approximation.
Data by Havens and Spicer (1985). See table 1.
$\Delta\rho_o/\rho_a = 3.19$; $H_o/R_o = 2$.

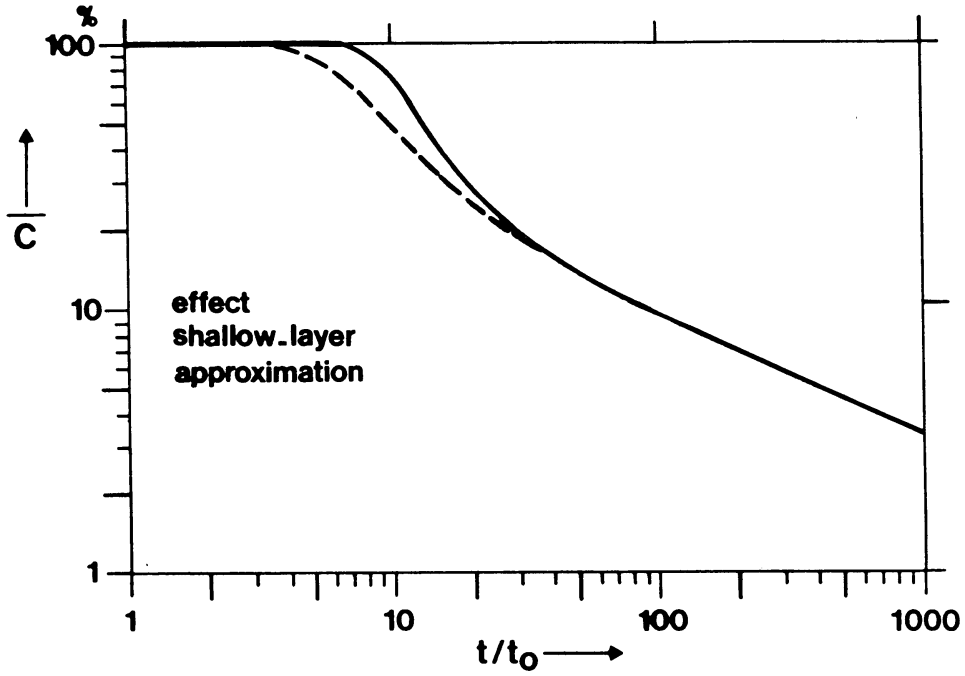

figure III.12: Cloud-averaged concentration versus dimensionless time.
Solid line : standard model.
Broken line: model with shallow layer approximation.
$\Delta\rho_o/\rho_a = 3.19$; $H_o/R_o = 2$.

In section III.3 we have mentioned the role of vertical accelerations and added mass in enhancing this time lag. In the momentum equations the terms containing H/R and $(H/R)^2$ account for these deviations from the shallow layer approximation. To investigate the effect of these terms we have run the model, neglecting these terms in the momentum equation and in the turbulent energy equation (III.4.27). The computed results for the cloud area and the cloud concentration are shown in the figures III.11 and III.12. In figure III.11 we see that the shallow layer approximation leads to a much faster acceleration from rest, which is not supported by the measured data. Apparently the non-hydrostatic correction terms should be included, as they are in the full model, at least for releases with a high initial aspect ratio H_o/R_o. In figure III.12 we see that the faster acceleration of the shallow layer model leads to an earlier start of the mixing process, as is to be expected.

III.6.2 Discussion on empirical coefficients

In this section we discuss the values of the major empirical coefficients used in our model.

We start with the drag coefficient c_d' which has been defined by (III.3.35). In section III.3 we have deduced that $c_d' = 0.64$. This estimate is based on direct measurements of the front conditions of steady and unsteady gravity currents see chapter II). This value of c_d' is consistent with the experimental data discussed in section III.5. The estimated accuracy of the value of c_d' is 10%. Changes of 10% in c_d' have a very small effect on our model results. E.g. the computed cloud area decreases no more than 2%, with a 10% increase in c_d'. Thus $c_d' = 0.64 \pm 0.06$ appears an adequate choice for the drag coefficient.

Next we consider the entrainment coefficient c_e as defined in (III.2.3). Here we have used $c_e = 0.2$ as proposed by Driedonks and Tennekes (1984). This choice is based on experimental data for entraining boundary layers in the atmosphere and in the laboratory. Since in the case of a spreading cloud we deal with a different flow problem, the value of c_e is not as well established as that of c_d'. To investigate the sensitivity of the model to variations in c_e we have investigated the effect of changes of a factor 2 in c_e. In figure III.13 we give the model results for the dimensionless cloud area. We see that the effect of changes in c_e is quite small. In figure III.14 we give the computed cloud-averaged concentration $\bar{c}$. As expected, we see a marked effect of the variation in c_e.

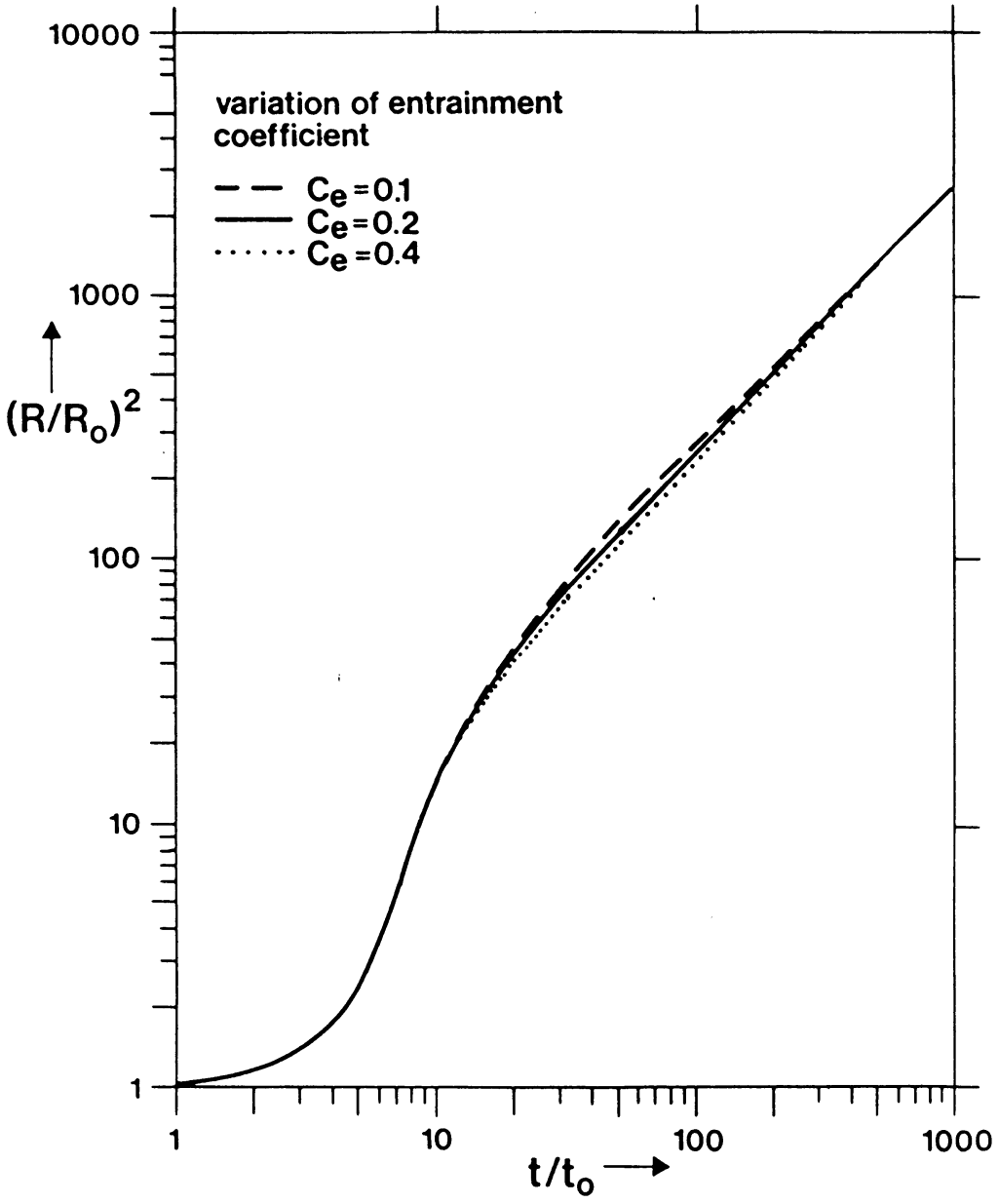

figure III.13: Dimensionless cloud area versus dimensionless time.
Effect of varying the entrainment coefficient c_e.
Solid line: standard model: $c_e = 0.2$.
$\Delta\rho_o/\rho_a = 3.19$; $H_o/R_o = 2$.

figure III.14: Cloud-averaged concentration versus dimensionless time.
(on next page) Effect of varying the entrainment coefficient c_e.
Solid line: standard model: $c_e = 0.2$.
$\Delta\rho_o/\rho_a = 3.19$; $H_o/R_o = 2$.

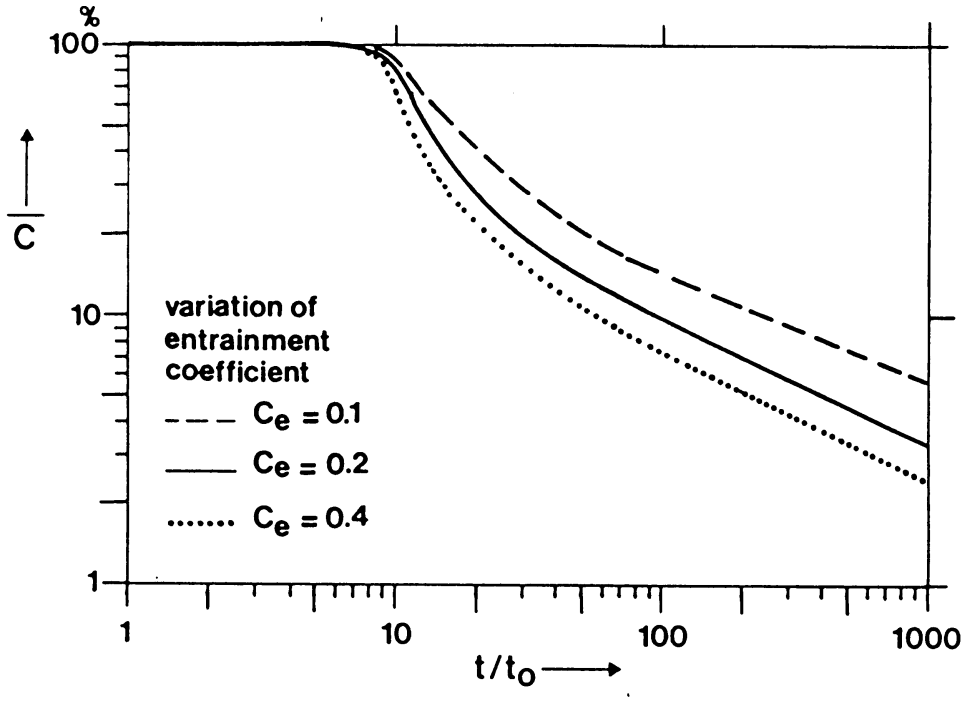

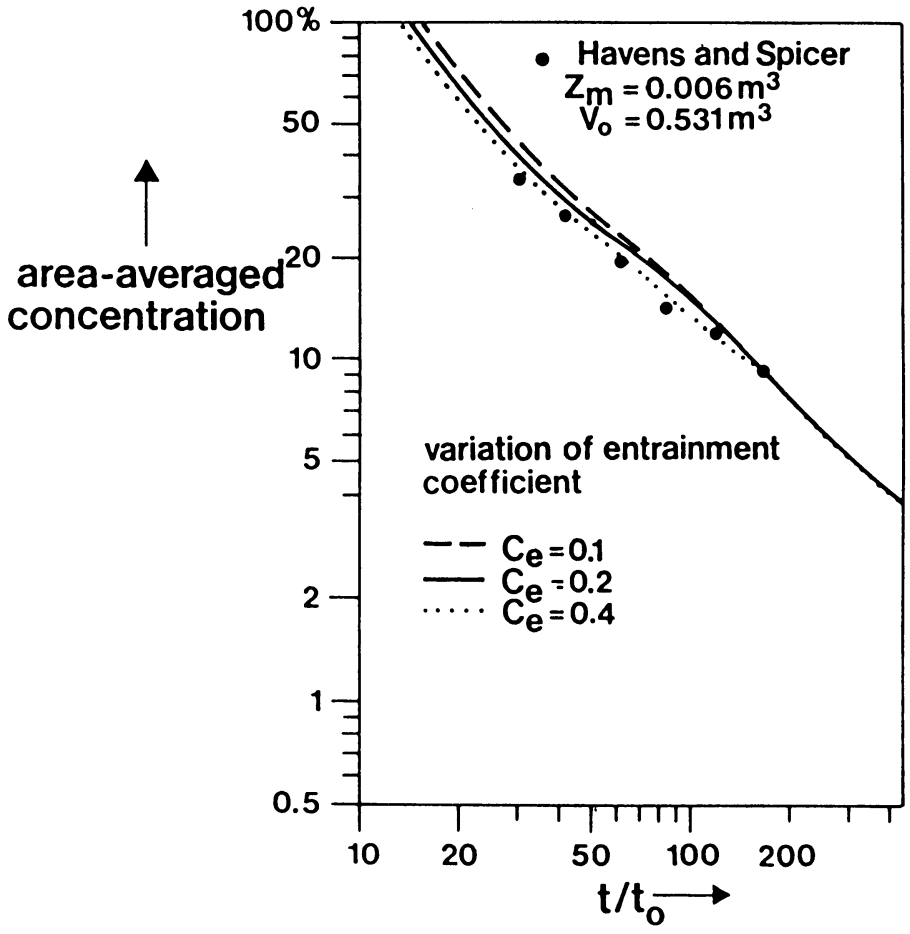

figure III.15: Area-averaged concentration versus dimensionless time. Effect of varying the entrainment coefficient c_e.

To relate this effect to measured data is not a straightforward task, because the volume cloud-averaged concentration is not a directly observed quantity. Furthermore the limited information on area-averaged concentration profiles, available for the experiments by Havens and Spicer (1985) and at Thorney Island, do not allow an accurate indirect estimate of the cloud-averaged concentration. Instead we will use the preliminary similarity profile (III.5.7) for estimating the area-averaged concentration at a given measuring height. In figure III.15 we give the results for the experiment by Havens and Spicer (1985) with $V_o = 0.531\ m^3$, $\Delta\rho_o/\rho_a = 3.19$ and $H_o/R_o = 2$ for the measuring height $z_m = 0.006$ m (see also figure III.6). As we see in figure III.15 the effect of changes in c_e on the computed area-averaged concentration at a given height is very small. The reason for this is that changes in $\bar{C}_c$ are accompanied by similar changes in H_c. This affects the scaled measuring height z_m/H_c and the profile correction (III.5.7) in such a way that a change in $\bar{C}_c$ is more or less compensated by the change in the profile correction (see also the discussion in section III.5). This is also true for the other available measuring heights. For "true" ground-concentrations ($z_m = 0$) this is not the case, but unfortunately such data are not available. The drawback of this is that with the available data the "correct" value of c_e cannot be pinned down accurately. With the present information we estimate that c_e is "known" within a factor of 2. Greater deviations from the standard value $c_e = 0.2$ lead to significantchanges in the computed cloud area which are inconsistent with the experimental data on the cloud area.

The last evaluation concerns our dissipation model and in particular the numerical coefficients c_n and c_b which have been defined in (III.4.13) and (III.4.16). We have run the model with c_n and c_b taken at half and twice their standard value. This corresponds with dividing or multiplying the standard dissipation rate by a factor of 2. In terms of the critical Richarson number Ri_c defined in (III.4.22) this corresponds with $Ri_c = 0.4$ and $Ri_c = 0.14$ respectively. In the figures III.16 and III.17 we give the model results. Changing the dissipation has a moderate effect on the cloud area. The effect on the cloud-averaged concentration is very pronounced. For $t/t_o > 300$ it is more than a factor 2. The effect is small for the area-averaged concentrations at the measuring heights of the experiments discussed previously, for reasons given before. The available data on the cloud area indicate an incertainty of about a factor of 2 in the dissipation rate. Similarly the incertainty in the "true" cloud-averaged concentrations and in the "true" cloud height is about a factor of 2.

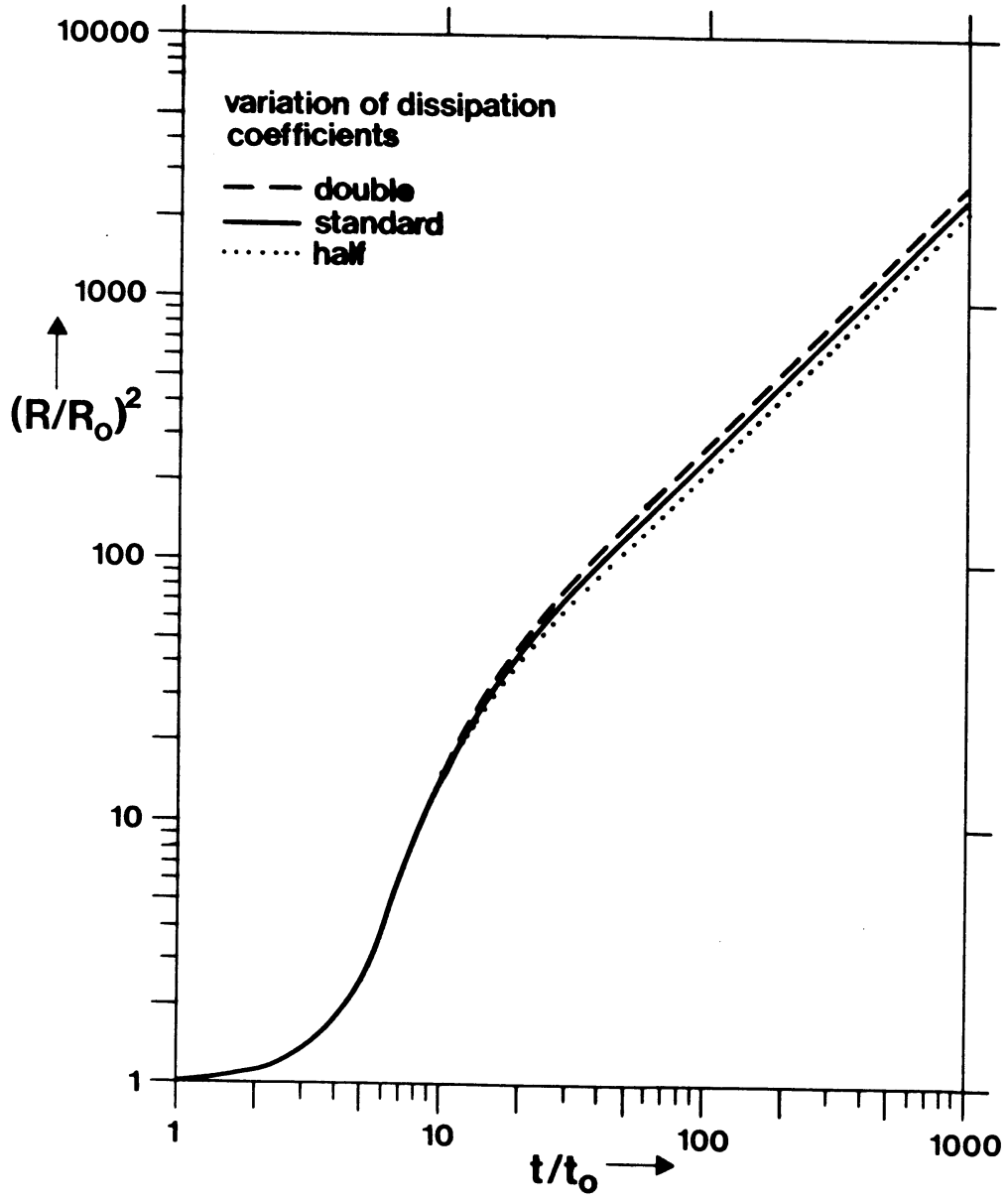

figure III.16: Dimensionless cloud area versus dimensionless time.
Effect of varying the dissipation rate.
Solid line: standard model.
$\Delta\rho_o/\rho_a = 3.19$; $H_o/R_o = 2$.

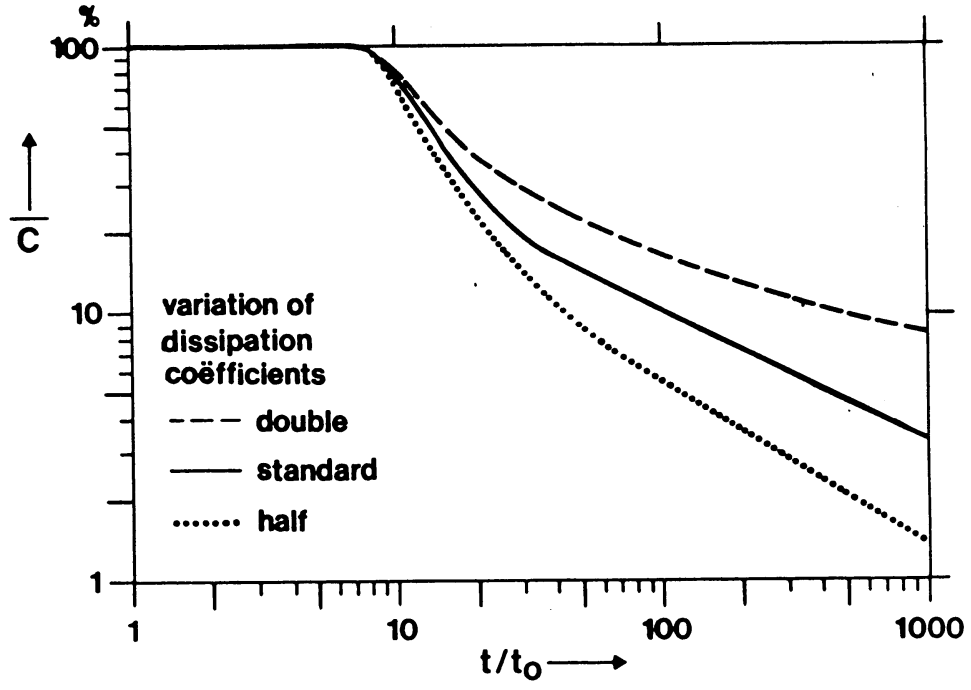

figure III.17: Cloud-averaged concentration versus dimensionless time.
Effect of varying the dissipation rate.
Solid line: standard model.
$\Delta\rho_o/\rho_a = 3.19$; $H_o/R_o = 2$.

III.6.3 Discussion on initial conditions

In this section we present model results for various initial conditions. In figure III.18 we show the computed cloud area for $H_o/R_o = 2$ and for varying initial density $\Delta\rho_o/\rho_a$. We see a marked effect on the initial acceleration, but for $t/t_o > 20$ the cloud area becomes independent of the initial density. In figure III.19 we give the cloud area for $\Delta\rho_o/\rho_a = 3.19$ and for varying initial aspect-ratio H_o/R_o. Here we see a pronounced effect on the initial acceleration, which lasts till about $t/t_o = 40$. The results shown in the latter two figures can be qualitatively understood by looking at the momentum equation (III.3.31) at the time $t/t_o = 0$ when $U_f = 0$. Then (III.3.31) can be written in the following dimensionless form:

$$\left[\frac{d(U_f/U_o)}{d(t/t_o)}\right]_{\frac{t}{t_o}=0} = \frac{1}{\frac{2}{3}\left(1+\frac{\Delta\rho_o}{\rho_a}\right) + 4\frac{H_o}{R_o} + \frac{4}{3}\left(1+\frac{\Delta\rho_o}{\rho_a}\right)\left(\frac{H_o}{R_o}\right)^2} \qquad \text{(III.6.3)}$$

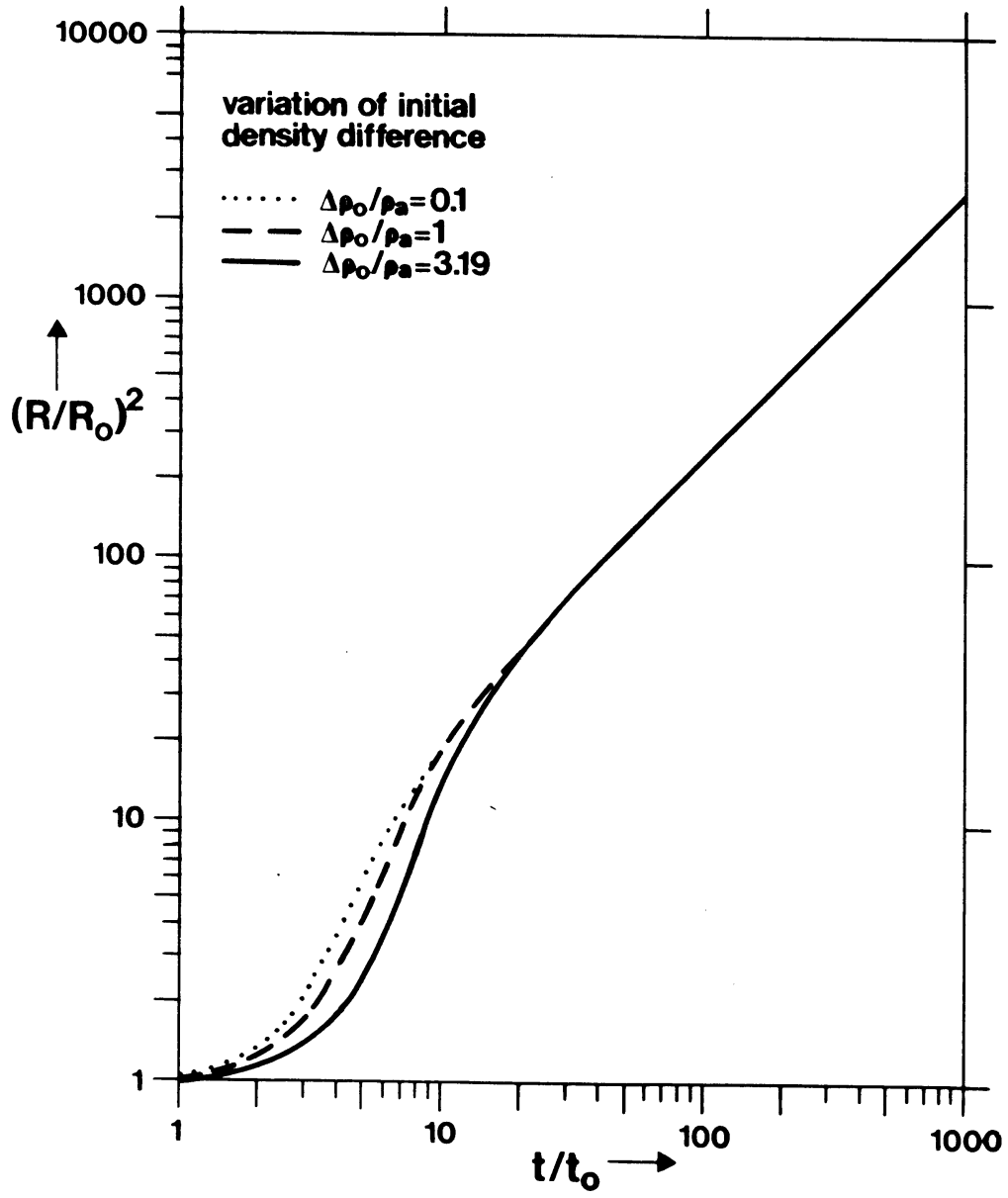

figure III.18: Dimensionless cloud area versus dimensionless time. Effect of varying the initial density difference $\Delta\rho_o/\rho_a$; $H_o/R_o = 2$.

In this equation we see directly that the initial dimensionless acceleration depends on $\Delta\rho_o/\rho_a$ and H_o/R_o. It is clear that the Boussinesq approximation and the shallow layer assumption are not valid. The initial acceleration reaches a maximum value of 3/2 when $\Delta\rho_o/\rho_a \ll 1$ and $H_o/R_o \ll 1$.

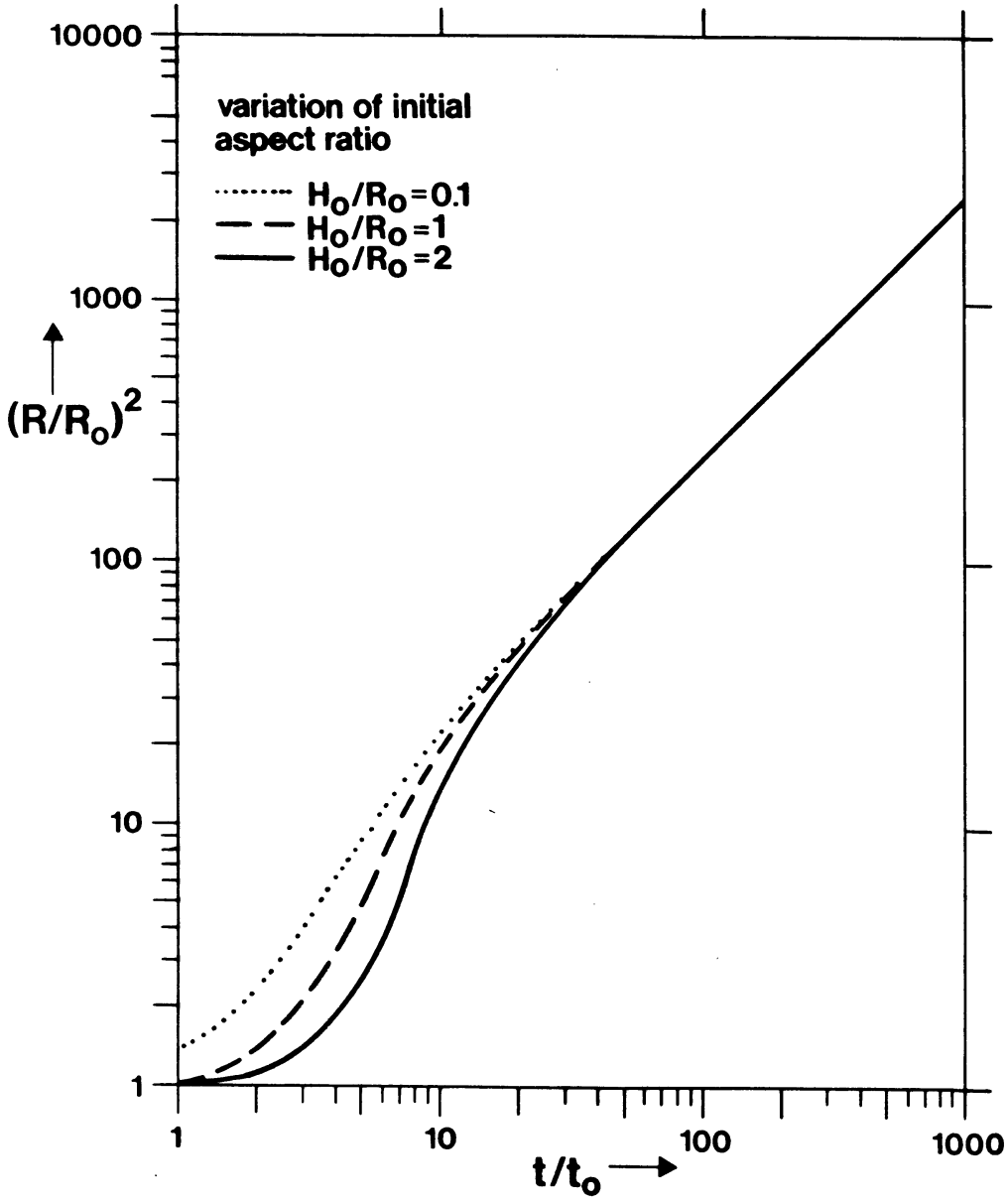

figure III.19: Dimensionless cloud area versus dimensionless time. Effect of varying the initial aspect ratio H_o/R_o. $\Delta\rho_o/\rho_a$ = 3.19.

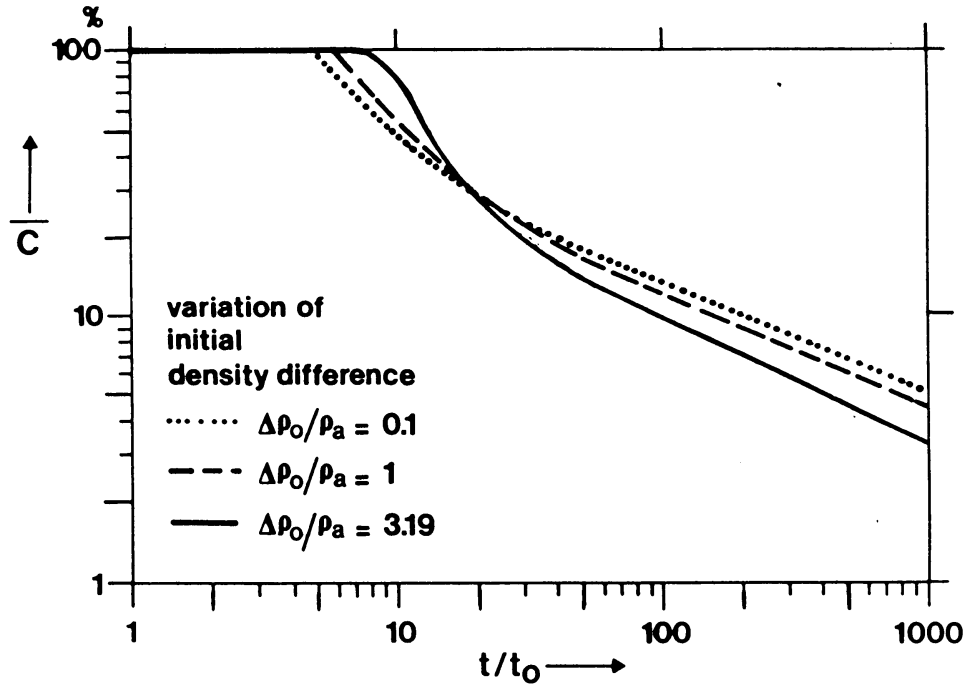

figure III.20: Cloud-averaged concentration versus dimensionless time. Effect of varying the initial density difference $\Delta\rho_o/\rho_a$. $H_o/R_o = 2$.

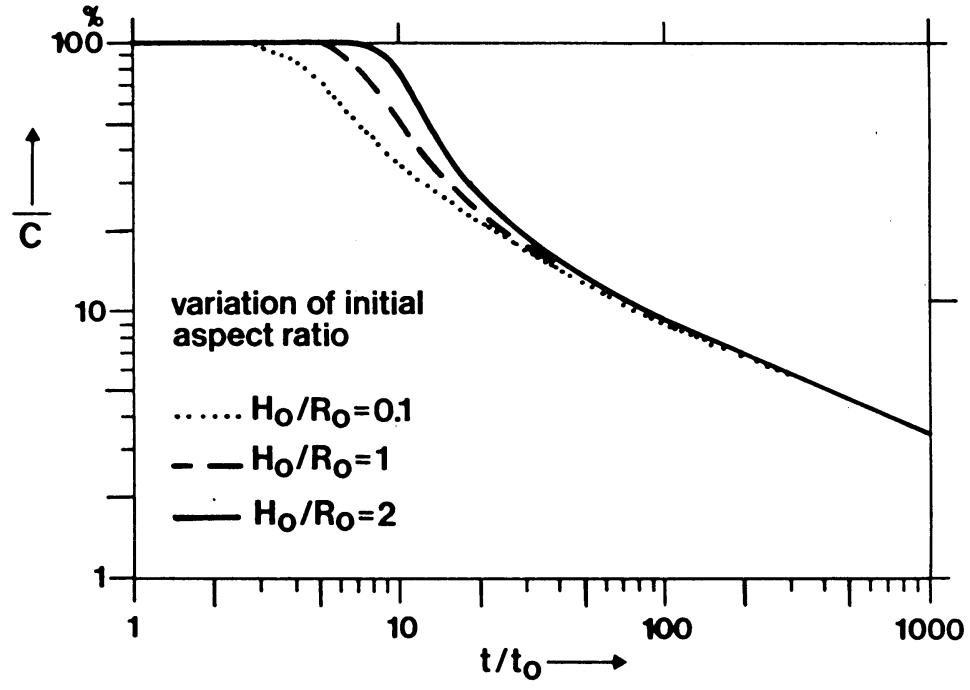

figure III.21: Cloud-averaged concentration versus dimensionless time. Effect of varying the initial aspect-ratio H_o/R_o. $\Delta\rho_o/\rho_a = 3.19$.

Next we consider the effect of the initial conditions on the cloud concentration. In figure III.20 we show the effect of cloud density. We see that the mixing process starts earlier for smaller initial density. This is due to the more rapid initial acceleration. For larger times we see higher concentrations for lower initial density. This can be explained by the higher dissipation that occurs for smaller densities when $t/t_o \approx 10$. In figure III.21 we show the results on cloud concentration for various initial aspect ratios. We see a moderate effect for $t/t_o < 100$.

Finally we consider the combined effect of lowering the initial value of both $\Delta\rho_o/\rho_a$ and H_o/R_o. In figure III.22 we show the model results for the cloud area. lowering both $\Delta\rho_o/\rho_a$ and H_o/R_o leads to a significantly more rapid acceleration (in terms of t/t_o). The interpretation is easy, when (III.6.3) is considered. It should be noted that the curve for $(R/R_o)^2$ approaches a similarity solution when both $\Delta\rho_o/\rho_a$ and H_o/R_o vanish. This solution is given by:

$$(R/R_o)^2 = 2k_\infty \, t/t_o \qquad \text{(III.6.4)}$$

with

$$k_\infty = 1.17. \qquad \text{(III.6.5)}$$

The solution is valid for $t/t_o > 1$.

Next we consider the cloud concentration in figure III.23. Here we see that the effect of the initial conditions is present both in the early acceleration phase and for $t/t_o > 100$. Again we see that when $\Delta\rho_o/\rho_a$ and H_o/R_o both vanish the curve for $\bar{c}$ approaches a similarity solution. This solution can be represented by

$$\bar{c} = (t/t_o)^{-0.41} \quad \text{for } t/t_o > 1 \; . \qquad \text{(III.6.6)}$$

A similar slope is found for other initial conditions for large times. This slope is significantly less negative than the slope - 0.70 found by Brighton (1985). The present study indicates that the high entrainment rate that corresponds with a slope - 0.7 leads to a reduction in the growth of the cloud area that is inconsistent with the available data for the cloud area.

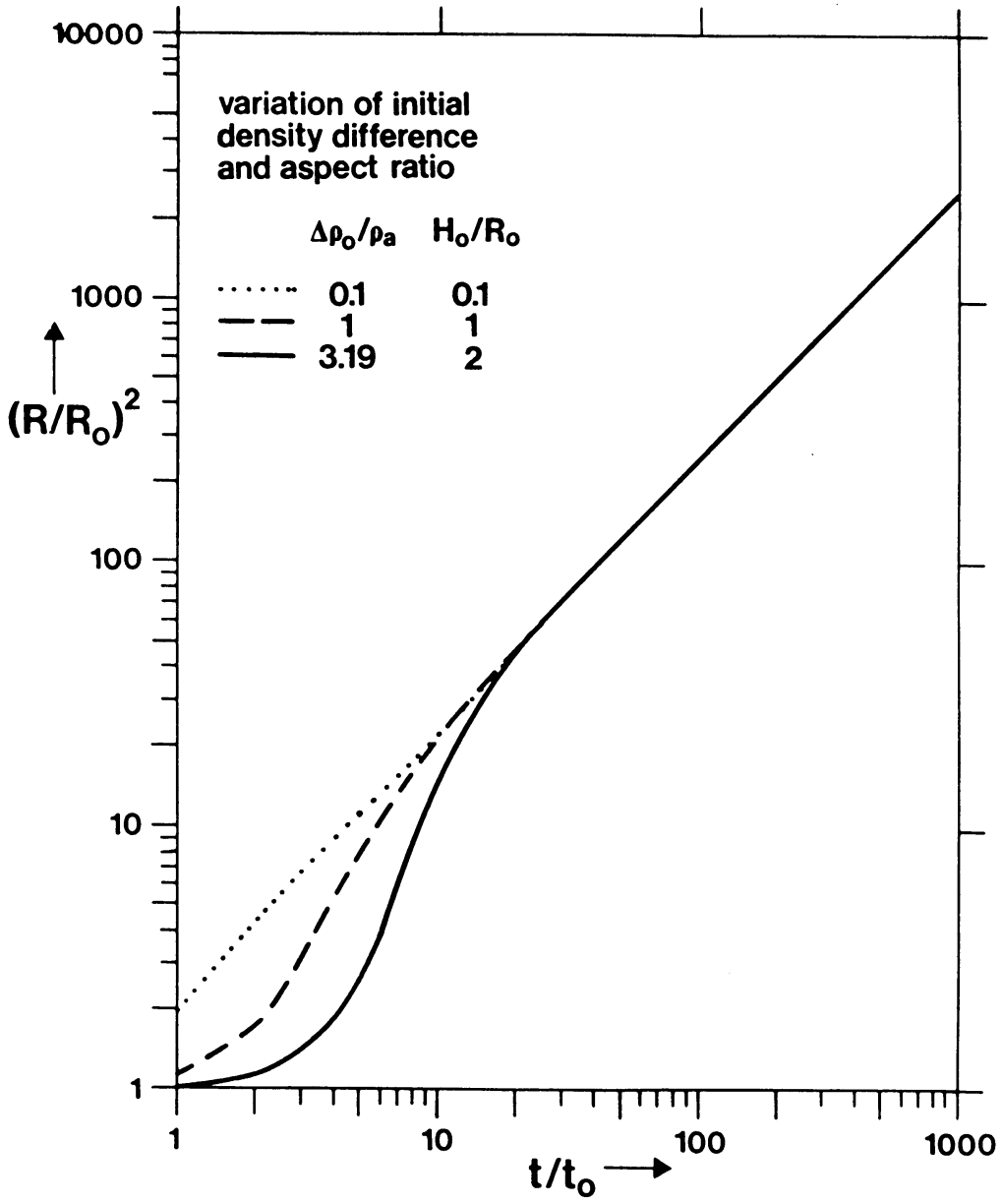

figure III.22: Dimensionless cloud area versus dimensionless time. Effect of varying both the initial density difference and the initial aspect ratio.

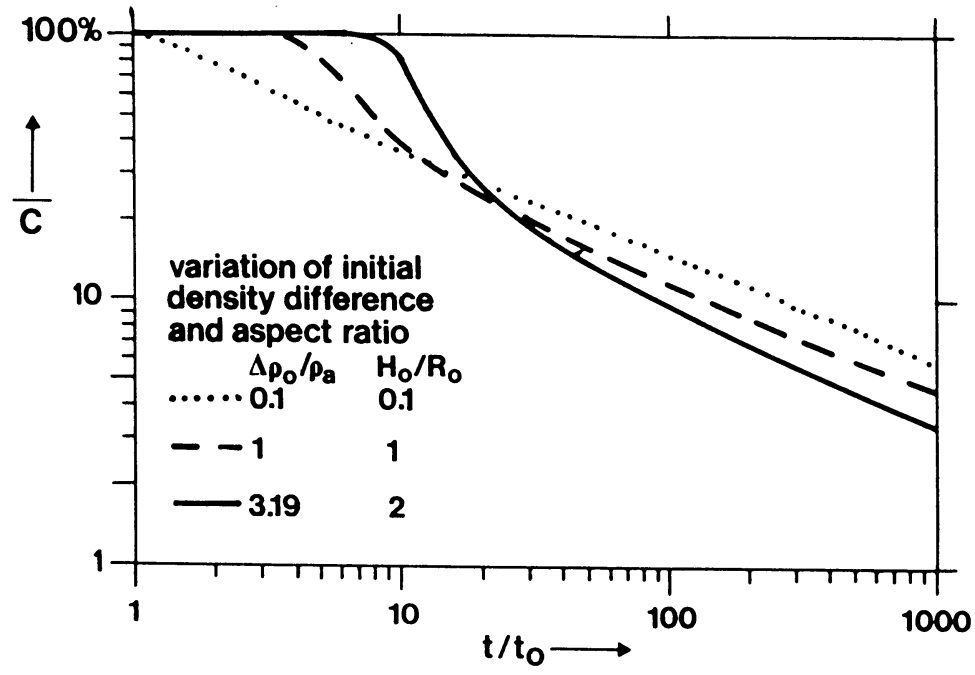

figure III.23: Cloud-averaged concentration versus dimensionless time. Effect of varying both the initial density difference and the initial aspect ratio.

III.7 Conclusions

We have presented a dynamical integral model for the spreading and mixing of a dense cloud in still air. The model is fully non-hydrostatic and non-Boussinesq. The numerical coefficients in the model have been estimated independently from the experiments that have been simulated in this chapter.

The model describes satisfactorily the radial gravity spreading observed in the laboratory and is consistent with available field data for low windspeed conditions.

The model gives predictions for the cloud height and the volume-averaged concentration. Also a preliminary similarity profile for the vertical concentration distribution has been deduced from the experiments analysed in this chapter. The model predictions in combination with this similarity profile give a satisfactory simulation of observed concentrations. This indicates that concentrations in dense clouds decrease rapidly with height near the surface and more slowly higher up in the cloud. The Gaussian profile does not seem to be a proper approximation to vertical concentration profiles.

The present analysis shows that most of the laboratory data by Havens and

Spicer (1985) are consistent with the field data obtained at Thorney Island during weather conditions with low atmospheric turbulence and low windspeeds. The laboratory runs with $V_o \geq 0.054$ m^3, $\Delta\rho_o/\rho_a = 3.19$ and $H_o/R_o = 2$ show no scale effects in the analysed time interval.

We have shown that it is essential to include non-hydrostatic and non-Boussinesq terms in the model equations in order to obtain acceptable results for small times ($t/t_o < 20$). For large times these terms have little or no effect on the model results. For small values of $\Delta\rho_o/\rho_a$ and H_o/R_o the model results approach a similarity solution for $t/t_o > 1$ with an asymptotic Froude number $k_\infty = 1.17$ and an equivalent edge-entrainment coefficient $\alpha_e = 0.41$. The latter value implies a much lower entrainment rate and therefore much higher concentrations than assumed in previous studies.

Chapter IV
REFLECTIONS ON THE CONSTRUCTION OF A COMPREHENSIVE MODEL FOR DENSE CLOUD DISPERSION

IV.1 Introduction

Since generally wind and turbulence are present in the atmosphere, a dense cloud will not stay in the quasi-uncoupled phase that has been described in chapter III. Sooner or later a transition will take place to the coupled phase, the mixed phase and the passive phase. So a comprehensive model has to deal with these latter phases also. To construct a comprehensive model, knowledge is required of both the density driven flow phenomena and the transport and diffusion processes due to the atmospheric flow. In their purest form the latter processes are present in the passive phase. In the passive phase the cloud particles just follow the atmospheric flow, without disturbing it. Thus a good approach is to describe passive dispersion first, and then try to combine the dense gas effects and the passive dispersion processes to model the intermediate phases.

IV.2 Basic processes in passive cloud dispersion

The basic processes that determine the dispersion of a passive cloud are the following. In the first place a passive cloud is advected by the mean wind. Because usually the windspeed increases with height, the advection velocity of the cloud will increase as the cloud depth increases. Furthermore this advection velocity will be higher for cloud particles, that happen to be in the top of the cloud, than the advection velocity for particles that are temporarily in the lower part of the cloud. Thus we expect that the concentration distribution of the cloud is skewed in the sense that the top of the cloud is further downwind than its bottom. When also the wind direction changes with height, which is normally the case in the bulk of the atmospheric boundary layer, an even more complicated stretching mechanism takes place.

In the second place the cloud as a whole is displaced by large horizontal eddies. Large means here: larger than the horizontal scales of the cloud. This leads to a meandering cloud motion relative to the advection by the mean wind and to an inherent uncertainty in the predictability of the position of an individual cloud. This is an absolute diffusion process that requires knowledge of the Lagrangian statistics of single particle motion.

In the third place the cloud is subject to diffusion by small scale

eddies, both horizontally and vertically. We may expect that this process leads to smooth average concentration distributions, with turbulent concentration fluctuations relative to these average distributions. Diffusion by small scale eddies is called relative diffusion and requires knowledge of the statistics of two-particle diffusion.

Of particular importance is the interaction between windshear and vertical diffusion. Windshear creates variance in the direction of the wind in the form of a skewed distribution. Vertical diffusion destroys this variance and tries to re-establish a homogeneous horizontal distribution. In this process the shear-produced skewness is transformed into diffusive variance in the wind direction. The actual skewness of the concentration distribution is determined by the magnitude of the windshear and by the magnitude of vertical diffusion. In general we may expect, that in stable atmospheric conditions the cloud is very skewed, because windshear is large and vertical diffusion small. In unstable conditions the opposite is true. Windshear is small and vertical diffusion is large, which will limit the skewness in these conditions.

As we see, the dispersion of a passive cloud is determined by complicated processes. It is therefore no wonder, that in the literature not a single model has been reported, that deals with all these processes in a satisfactory manner.

What do we call satisfactory? Let us try to formulate this and also discuss some relevant literature. A first requirement is that the dispersion model is based on an adequate characterization of the state of the atmosphere and in particular of the atmospheric boundary layer. This implies a proper description of the wind profile and of the characteristics of turbulence in terms of observable parameters. The problems involved with the characterization of the atmospheric boundary layer are discussed in some detail by Van Ulden and Holtslag (1985) and by Gryning et al. (1987). It appears that the scaling of the boundary layer in terms of similarity parameters forms an adequate basis for the description of dispersion in general. Therefore such a basis is strongly recommended as the starting point for a dispersion model for a passive puff.

Next we require that the dispersion model itself rests on a firm basis. A suitable basis is the continuity equation in a differential form (Csanady, 1973; p. 85). From this equation statistical information on dispersion can be obtained from ensemble averaging over a large number of hypothetical puff experiments. By applying ensemble averaging in fixed and cloud following coordinates a proper distinction can be made between absolute and relative diffusion (Csanady, 1973: p. 87). In this manner a diffusion equation can be derived

that describes the combined effects of windshear and relative diffusion. Many modelers do not make the distinction between absolute and relative diffusion. E.g. Chatwin (1968) and Wheatley (1987) use diffusion equations that presuppose a hypothetical atmosphere, in which no large horizontal eddies exist, but this is not cleary mentioned in these papers. Apart from this shortcoming these papers form a suitable basis for the analysis of the puff-dispersion problem.

Chatwin (1968) describes in detail the interaction between windshear and vertical diffusion for the neutral atmospheric surface layer. Using the method of integral moments by Aris (1956) and by Saffman (1962) he arrives at exact analytical results, which not only have theoretical, but also great practical value. The reason for this is that no experimental information seems to be available on this particular interaction process. Mikkelsen et al. (1982, 1984) extend these ideas to a diabatic surface layer, specified in terms of Monin-Obukhov similarity parameters. However, in these papers the treatment of the shear effect is not very convincing.

Wheatley (1987) includes the shear effect in a plausible, but approximate manner. Wheatley does not retrieve the exact results by Chatwin (1968) for the neutral case. Nevertheless Wheatley's model has great merits, because it makes the problem manageable for the general diabatic case. An advantage of this model is, that it is formulated in terms of rate equations for the vertical and horizontal scales of the cloud and for the skewness of the concentration distribution. These rate equations give the relation between the development of the concentration distribution and observable parameters like the friction velocity u_* and the Obukhov length. In principle this makes it possible to combine Wheatley's model with our dense gas model, which is also formulated in terms of rate equations for the scales of the cloud in terms of observable parameters.

A few problems still have to be solved. In the first place Wheatley's model should be modified as to match the exact results by Chatwin (1968) for the neutral case. In the second place Wheatley's rate equations contain integrals that have to be evaluated numerically. The model would be easier to handle, when these integrals were replaced by analytical approximations of the type proposed by van Ulden (1978) and by van Ulden and Nieuwstadt (1980). Finally absolute and relative horizontal diffusion deserve more attention. A recent discussion is given e.g. in Mikkelsen et al. (1987). In this paper many other references are given.

In all we can say that a satisfactory treatment of the dispersion of a passive puff is not yet available, but seems to be within reach.

IV.3 Modeling the intermediate phases

We now continue our discussion with some remarks on the problems of modeling the intermediate phases. It concerns the modeling of the following processes: advection by the mean wind, vertical mixing, gravity spreading, stretching by windshear, relative horizontal diffusion and meandering. We will discuss these processes in this order.

Advection

Initially the center of mass of a dense cloud does not move. When an ambient wind is present a transfer of momentum to the cloud takes place, which sets the cloud into motion in the direction of the mean wind. The cloud accelerates until - in the passive phase - the cloud travels at the same speed as a passive cloud with the same depth. The modeling of this process is in a very rudimentary state, not the least because of uncertainties in the actual rate of vertical mixing (see also chapter III). Crude attempts to estimate the rate of momentum transfer have been made by Wheatly and Prince (1987) and by Puttock (1987). These attempts are too much of an ad-hoc character to be satisfactory.

Vertical mixing

To describe vertical mixing, the combined effects of cloud-generated turbulence and buoyancy, and atmospheric turbulence and buoyancy have to be modeled. Our dense gas model is a good starting point, because it gives the required information on cloud generated turbulence and buoyancy. In principle our turbulent energy budget can be extended to include source and sink terms related to atmospheric turbulence. How to do this is not completely clear. Another possibility is to extend our entrainment model with atmospheric turbulence and stability terms. However, this procedure is not straightforward. Nevertheless these two possibilities are probably preferable over a very simple model in which cloud-generated entrainment and atmospheric entrainment are just added as such. Of course simple models can be adjusted, as to fit data in a limited range of conditions as shown e.g. by Wheatley et al. (1986). The applicability of such models to a wider range of circumstances is doubtful. Thus also here research remains to be done.

Gravity spreading

As shown in chapter III the rate of gravity spreading is affected by vertical mixing, which produces a radial shear that reduces the rate of spreading. When vertical mixing is enhanced by atmospheric turbulence, also the

reduction of gravity spreading will be enhanced. So far no box-model seems to include this feature. In our dynamic box-model this feature is automatically incorporated, when the effect of atmospheric turbulence is included in the entrainment model. Thus modeling this process does not seem to offer problems, provided a dynamic box-model is used.

The effect of windshear

Modeling the effect of windshear is already a problem in the relatively simple passive phase. In the coupled phase we expect even greater difficulties. The precise form of the velocity profile in the cloud is not known and neither is the local rate of vertical mixing. Nevertheless a crude model can be thought of, which includes among other features the effect of the variation of the translational cloud speed. Some discussion on this problem can be found in Chatwin (1984). Here clearly a lot of work is to be done.

Relative horizontal diffusion

The description of horizontal diffusion is necessarily restricted to a semi-empirical approximation of horizontal variances. In principle these variances can be added to the variances due to gravity spreading and windshear. This addition then gives the horizontal scales of the cloud. Possibilities for an addition procedure have been described by Wheatley and Webber (1984).

Meandering

As long as a dense cloud is not fully coupled to the atmospheric flow, it will not fully follow the meandering motion due to large eddies. In principle this can be modelled by considering the inertia of the cloud and by representing the action of large eddies by a meandering force on the cloud. On the other hand this is probably more an academic question then a process that really has to be included in a comprehensive model.

IV.4 Concluding remarks

We have discussed a number of problems involved with the construction of a satisfactory comprehensive model. Interested readers can find more information in the literature, e.g. in Colenbrander (1980), Hunt et al. (1984), Wheatly and Webber (1984), Havens and Spicer (1985), Chatwin (1985) and Puttock (1987). Such papers support our conclusion, that there are certainly perspectives for the construction of a satisfactory comprehensive model, but that much work remains to be done.

REFERENCES

Abbott, M.B., 1961: On the spreading of one fluid over another. La Houille Blanche, No 5-6.

Aris, R., 1956: On the dispersion of a solute in a fluid flowing through a tube, Proc. Roy. Soc., A235, 67, 1956.

Barr, D.J.H., 1967: Densimetric exchange flow in rectangular channels. La Houille Blanche 6/67, 619-631.

Batchelor, G.K., 1967: An Introduction to Fluid Dynamics, pp 455-458. Cambridge University Press.

Beljaars, A.C.M., P. Schotanus and F.T.M. Nieuwstadt, 1983: Surface layer similarity under nonuniform fetch conditions. J. of Climate and Appl. Meteorology, 22, no. 10, pp 1800-1810.

Benjamin, T.B., 1968: Gravity currents and related phenomena. J. Fluid Mech., 31, 209-248.

Brighton, P.W.M., 1985: Area-averaged concentrations, height-scales and mass balances, J. Hazardous Materials, 11, pp 189-208.

Brighton, P.W.M., A.J. Prince and D.M. Webber, 1985: Determination of cloud area and path from visual and concentration records. J. Hazardous Materials, 11, pp 155-178.

Brighton, P.W.M. and A.J. Prince, 1987: Overall properties of the heavy gas clouds in the Thorney Island Phase II Trials. J. Hazardous Materials, 16, pp 103-138.

Brost, R.A. and J.C. Wyngaard, 1978: A model study of the stably stratified planetary boundary layer. J. Atmos. Sci., 35, 1427-1440.

Byggstøyl, S. and L.R. Saetran, 1983: An integral model for gravity spreading of heavy gas clouds. Atm. Env., 17, no. 9, pp 1615-1620.

Chatwin, P.C., 1968: The dispersion of a puff of passive contaminant in the constant stress region. Q. J. Royal Met. Soc., 94, pp 350-360.

Chatwin, P.C., 1984: The incorporation of windshear effects into box models of heavy gas dispersion. In: "Atmospheric Dispersion of Heavy Gases and small particles". G. Ooms and H. Tennekes, eds., Springer Verlag.

Chatwin, P.C., 1985: Towards a box model of all stages of heavy gas cloud dispersion. In: Turbulence and Diffusion in Stable Environments. J.C.R. Hunt, ed. Oxford University Press, pp 260-291.

Colenbrander, G.W, 1980: A mathematical model for the transient behaviour of dense vapour clouds; 3rd Int. Symp. on Loss Prevention and Safety Promotion in the process Industries, Basel, September, 1980.

Colenbrander, G.W. and J.S. Puttock, 1984: Maplin Sands experiments 1980: Interpretation and modelling of liquefied gas spills into the sea. In: "Atmospheric Dispersion of Heavy Gases and Small Particles" Ooms and Tennekes, editors, Springer Verlag, 277-295.

Csanady, G.T., 1973: Turbulent Diffusion in the Environment. Geoph. and Astroph. Monographs. D. Reidel Publishing Company.

Driedonks, A.G.M. and H. Tennekes, 1984: Entrainment effects in the well-mixed atmospheric boundary layer. Boundary-Layer Meteorology, 30, pp 75-105.

Duym, N.J., A.P. van Ulden, W.H.H. van Heugten and P.J.H. Builtjes, 1986: Physical and mathematical modeling of heavy gas dispersion - accuracy and reliability. In: Proceedings 15th I.T.M. on Air Poll. and its Appl., C. de Wispelaere ed., Plenum Press. St. Louis, April 16-19, 1985.

Emblem, K., P.A. Krogstad and T.K. Fanneløp, 1984: Experimental and theoretical studies in heavy gas dispersion. Part 1. Experiments. In: Atm. Dispersion of Heavy Gases and Small Particles, pp 307-321, G. Ooms and H. Tennekes. eds., Springer Verlag.

"Experiments with chlorine", 1975: Report published by Directorate General of Labour of the Ministry of Social Affairs, Voorburg, The Netherlands.

Fanneløp, T.K. and G.D. Waldman, 1971: The dynamics of oil slicks - or "creeping crude". 9th Aerospace Sciences Meeting A.I.A.A., New York, January 1971.

Fanneløp, T.K. and G.D. Waldman, 1972: The dynamics of oil slicks. A.I.A.A. Journal, 10, 506-510.

Fanneløp, T.K., P.A. Krogstadt and Ø. Jacobsen, 1980: The dynamics of heavy gas clouds. Norwegian Institute of Technology. Report J.F.A.G. B-124.

Fay, J.A., 1969: In "Oil on the Sea", ed. D.P. Hoult, 53-63, New York, Plenum.

Fay, J.A., 1980: Gravity spread and dilution of heavy vapor clouds. Proceedings of 2nd Int. Symp. on Stratified Flows, Trondheim, June 1980, 471-494.

Graziani, G., P. Moretti and G. Volta, 1987: Dispersione atmosferica di gas pesanti: Sviluppo del Modello MARA e suo confronto con dati sperimentali. Report EUR 11132 IT from the Central Research Establishment of the Commission of the European Community at Ispra (Italy).

Gryning, S.E., A.A.M. Holtslag, J.S. Irwin and B. Sivertsen, 1987: Applied dispersion modeling based on meteorological scaling parameters. Atmos. Env., 21, no. 1, p. 79.

Hall, D.J., Hollis, E.J., Ishaq, H., 1982: A wind tunnel model of the Porton dense gas spill. Warren Spring Laboratory, Report LR 394 (AP), May 1982.

Havens, J.A. and T.O. Spicer, 1984: Gravity spreading and air entrainment by heavy gases instantaneously released in a calm atmosphere. In: Atm. Dispersion of Heavy Gases and Small Particles, pp 177-189, G. Ooms and H. Tennekes eds., Springer Verlag.

Havens, J.A. and T.O. Spicer, 1985: Development of an atmospheric dispersion model for heavier-than-air gas mixtures. Report no. CG-D-23-85. U.S. Dept. of Transport. U.S. Coast Guard.

Hoult, D.P., 1972: Oil spreading on the sea. Ann. Rev. Fluid Mech., 4, 341-368.

Hunt, J.C.R. and A.H. Weber, 1979: A Lagrangian statistical analysis of diffusion from a ground-level source in a turbulent boundary layer. Q.J. Royal Met. Soc., 105, pp 423-443.

Hunt, J.C.R. and J.W. Rottman, 1984: Some physical processes involved in the dispersion of dense gases. In: "Atmospheric Dispersion of Heavy Gases and Small Particles", G. Ooms and H. Tennekes, eds., Springer Verlag, pp 361-398.

Huppert, H.E. and Simpson, J.E., 1980: The slumping of gravity currents. J. Fluid Mech., 99, 785-799.

McQuaid, J., 1984: Observations on the current status of field experimentation on heavy gas dispersion. In: Atmospheric Dispersion of Heavy Gases and Small Particles. Ooms and Tennekes, editors, Springer Verlag, 241-267.

McQuaid, J., 1985: Objectives and Design of the phase I heavy gas dispersion trials. J. Hazardous Materials, 11, pp 1-34.

Mikkelsen, T., 1982: A parametric description of a skewed puff in the diabatic surface layer. Risø Report 476, Roskilde, Denmark.

Mikkelsen, T., S.E. Larsen and S. Thykier-Nielsen, 1984: Description of the Risø Puff Diffusion Model, Nuclear Techn., 67, p. 56, 1.

Mikkelsen, T., S.E. Larsen and H.L. Pecseli, 1987: Diffusion of Gaussian puffs. Quart. J. Royal Met. Soc., 113, p. 81.

Monin, A.S. and Yaglom, A.M., 1971: Statistical Fluid Mechnics Vol. I. M.I.T. Press, Cambridge, Mass.

Nieuwstadt, F.T.M. and A.P. van Ulden, 1978: A numerical study on the vertical dispersion of passive contaminants from a continuous source in the atmospheric surface layer. Atm. Env., 12, pp 2119-2124.

Ooms, G. and H. Tennekes, 1984: Editors, Proceedings from IUTAM symposium on "Atmospheric Dispersion of Heavy Gases and Small Particles". Delft, Aug. 29 - Sept. 2, 1983; Springer Verlag.

Picknett, R.G., 1978: Fluid experiments on the behaviour of dense clouds. Part I, Main Report. Ptn 1 L 1154/78/1, Chemical Defense Establishment, Porton Down, U.K.

Picknett, R.G., 1981: Dispersion of dense gas puffs released in the atmosphere at ground level. Atm. Env., 15, 509-525.

Puttock, J.S., 1987: Analysis of meteorological data for the Thorney Island phase I trials. J. Hazardous Materials, 16, pp 43-74.

Puttock, J.S., 1987: Comparison of Thorney Island Data with predictions of the HEGABOX/HEGADAS. J. Hazardous Materials, 16, pp 439-456.

Saffman, P.G., 1962: The effect of wind shear on horizontal spread from an instantaneous ground source, Quart. J. Royal Met. Soc., 88, p. 382.

Schmidt, W., 1911: Zur Mechanik der Böen. Meteorologisches Zeitschrift, August 1911, pp 355-362.

Simpson, J.E., 1972: Effects of the lower boundary on the head of a gravity current. J. Fluid Mech. 53, 759-768.

Simpson, J.E. and Britter, R.E., 1979: The dynamics of the head of a gravity current advancing over a horizontal surface. J. Fluid Mech., 94, 477-495.

Simpson, J.E., 1982: Gravity currents in the laboratory, atmosphere and ocean. Ann. Rev. Fluid Mech., 14, 213-234.

Tennekes, H. and J.L. Lumley, 1973: A first course in turbulence. M.I.T. Press, Cambridge, Mass.

Tennekes, H. and Driedonks, A.G.M., 1981: Basic entrainment equations for the atmospheric boundary layer. Boundary Layer Meteorology, 20, 515-531.

Van Ulden, A.P., 1974: On the spreading of heavy gas released near the ground. Proceedings Int. Loss Prevention Symp., pp 221-226, C.H. Buschman ed., Elsevier, Amsterdam.

Van Ulden, A.P., 1978: Simple estimates of vertical diffusion from sources near the ground. Atm. Env., 12, pp 2121-2129.

Van Ulden, A.P., 1979: The unsteady gravity spread of a dense cloud in a calm environment. In: Proceedings of 10th. I.T.M. on Air Poll. Mod. and its Appl., NATO-CCMS, Rome.

Van Ulden, A.P. and F.T.M. Nieuwstadt, 1980: Discussions on vertical diffusion. Atmos. Env., 14, pp. 267-270.

Van Ulden, A.P., 1984: A new bulk model for dense gas dispersion: two-dimensional spread in still air. In: Atm. Dispersion of Heavy Gases and Small Particles, pp 419-440, G. Ooms and H. Tennekes eds., Springer Verlag.

Van Ulden, A.P. and A.A.M. Holtslag, 1985: Estimation of atmospheric boundary layer parameters for diffusion applications. J. Climate and Appl Met., 24, p. 1196-1207.

Van Ulden, A.P., 1987 [A]: The spreading and mixing of a dense cloud in still air. Proceedings of I.M.A. conference on "Stably Stratified Flow and Dense Gas Dispersion", Chester, April, 1986, J.S. Puttock, editor, Oxford University Press.

Van Ulden, A.P., 1987 [B]: The heavy gas mixing process in still air at Thorney Island and in the laboratory. J. of Hazardous Materials, 16, pp 411-426.

Webber, D.M. and C.J. Wheatley, 1987: The effect of initial potential energy on the dilution of a heavy gas cloud. J. Hazardous Materials, 16, pp 357-380.

Wheatley, C.J. and Webber, D.M., 1984: Aspects of the dispersion of denser-than-air vapours relevant to gas cloud explosions. Report VII/829/84-E, Safety and Reliability Directorate, Warrington WA 3 4NE, England.

Wheatley, C.J., P.W.M., Brighton and A.J. Prince, 1986: Comparison between data from the heavy gas dispersion experiments and predictions of simple models. In: Air Pollution Modelling and its Application V, C. de Wispelaere, ed., Plenum, New York, pp. 717-721.

Wheatley, C.J. and Prince, A.J., 1987: Translational cloud speeds in the Thorney Island trials: mathematical modeling and data analysis. J. Hazardous Materials, 16, pp 185-200.

Wheatley, C.J., 1987: Dispersion in a stratified flow adjacent to a wall. Preprints of 3rd Int. Symp. on Stratified Flows, Cal. Inst. of Techn., California.